N- and O- Donor Ligands for Fluorometric and Colorimetric Detection of Metal Ions

A Dissertation Submitted to the
Indian Institute of Technology Guwahati
as Partial Fulfillment for the Degree
of
Doctor of Philosophy
in
Chemistry

by

Araghni Bhattacharya

Roll No. 176122036

Department of Chemistry

Indian Institute of Technology Guwahati

Guwahati – 781039

November 2023

Dedicated

to

My late Grandparents,

My Parents

and

Well wishers

DEPARTMENT OF CHEMISTRY
INDIAN INSTITUTE OF TECHNOLOGY GUWAHATI
GUWAHATI–781039

DECLARATION

I do hereby declare that the research work embodied in this thesis entitled "**N- and O- Donor Ligands for Fluorometric and Colorimetric Detection of Metal Ions**" is the outcome of research work carried out by me under the supervision of Prof. V. Manivannan, at the Department of Chemistry, Indian Institute of Technology Guwahati, Assam, India.

In keeping with the general practice of reporting scientific observations, due acknowledgements have been made wherever the work described is based on the findings of other investigators.

Araghni Bhattacharya

IIT Guwahati
November 2023

Araghni Bhattacharya
(Roll No. – 176122036)

Dr. V. Manivannan
Professor
Department of Chemistry
Indian Institute of Technology
Guwahati-781039
Assam, INDIA

Ph: +91 361 258 2306 (O)
E-mail: mani@iitg.ac.in

CERTIFICATE

This is to certify that the research work presented in this thesis entitled "**N- and O- Donor Ligands for Fluorometric and Colorimetric Detection of Metal Ions**" is an authentic record of the results obtained from the research work carried out by **Araghni Bhattacharya** under my supervision in the Department of Chemistry, Indian Institute of Technology Guwahati, India. This work is original and has not been submitted elsewhere for a degree.

V. Manivannan

IIT Guwahati
November 2023

Prof. Vadivelu Manivannan
(Thesis Supervisor)

Acknowledgements

The career of a Doctoral student begins with the hope of becoming a part of the research activities that are shaping the world through inventions and technological advancements. I set sail on the voyage of pursuing my Doctoral research with the same hope. And finally, with my utmost delight, I can see that journey coming to a fruitful end. During my tenure as a PhD scholar, I went through a lot of challenges both academic and non-academic. Now, it is time to acknowledge the people and the establishments that have been constantly helping me to overcome difficulties and guide me to success.

At first, I deeply acknowledge my thesis supervisor Prof. Vadivelu Manivannan for his continuous guidance, support and motivation over the past six years. Even during the difficult times of the COVID-19 pandemic, he motivated me to stay on the right track and keep exploring new ideas that were beneficial for my research thesis.

I extend my sincerest gratitude to my Doctoral Committee members Prof. Anil Kumar Saikia (Chairperson), Prof. Lal Mohan Kundu and Prof. Seenipandian Ravi for their invaluable suggestions that significantly improve my thesis. Our collaborators Mr. Ashutosh Bandyopadhyay and Prof. Biman B. Mandal are respectfully acknowledged for their contribution to my second Chapter.

I also feel grateful to my late grandparents who always dreamt of seeing me as a successful Doctorate student and finally, I am able to fulfil their dream. I am also thankful to my parents for their continuous support and well wishes that helped me in difficult times and made me committed to my work.

My stay at IIT Guwahati would not have been enjoyable if I had not met knowledgeable friends and juniors like Dr. Bitan Sardar and Dr. Anik Ghosh with whom I had spent hours discussing on academic and non-academic topics. I had been associated with the Bengali cultural society of IIT Guwahati, "Tero Parbon," and spent quality times while organising different cultural activities as a member and as in leadership role. I am thankful to the society and its fellow members. I would also like to thank some of my friends and juniors of IIT Guwahati, Dr. Mrityunjoy Barman, Mr. Buddhadeb Ghosh, Dr. Biswanath Mahato, Dr. Sagnik Dey, Mr. Anjishnu Biswas, Mr. Bipradip Dey, Ms. Chandrika Ghosh, Mr. Aritra Mitra, Mr. Aniket Banerjee, Mr. Gourav Bhattacharjee, Ms Swagata Patra, Dr. Bhanupriya Das, Dr. Supriya Das, Ms. Manideepa Paul, Ms. Monikha Chetia, Mrs. Shilpa Bhuyan, Dr. Mihir Manna, Dr. Megha Basak, Dr. Debojit Paul, Dr. Senjuti Halder, Dr. Sourav Bhowmik, Mr. Arindam Bikash Neog, Dr. Abu Sufian and Mr. Tipu Alam for the academic help and the golden memories that we have made together. I am also grateful to Ms. Ishana Bhattacharya for being supportive to me during the last phase of my doctoral research. I am grateful to my dear schoolmates and fellow research scholar friends of other institutions. Respectable seniors

of IIT Guwahati Dr. Debojit Bhattacharjee and Dr. Tousif Hossen have always inspired me with positive motivational words and their experience in the research field, and I offer my heartiest thankfulness to them.

Besides, I take this opportunity to acknowledge senior lab members, Dr. Nibedita Behera and Dr. Jugal Bori for their sincere efforts to help me learn different experimental techniques and research methodology. I am grateful to my junior Mr. Sandeep Kumar for helping me in solving the crystal structure by SC-XRD. I duly acknowledge Mr. Amlan Ranjan Rayasingh for helping me with the HRMS data. I am also thankful to other lab mates and project students who have worked with me.

I am thankful to the Department of Chemistry, Central Instrumental Facility and PARAM-ISHAN supercomputing facility of IIT Guwahati for providing me with the instrumental and computational facility for carrying out my research works. I am also thankful to the Ministry of Human Research Development for the fellowship. I am obliged to the staffs of Department of Chemistry and the operators of Central Instrumental Facility for the official help and the recording of the data from various instruments respectively.

Araghni Bhattacharya

Preface

This Thesis contains five chapters. Chapter 1 is the introduction which describes the contribution of metals in our daily lives and their adverse effects on human beings when exposed to excess amounts along with a brief elaboration of different detection techniques. Some recent developments in devising fluorescent and colorimetric probes are also discussed. In Chapter 2 the 2,4,5-tris(2-pyridyl)imidazole (**L1H**) molecule has been evaluated as a probe for dual sensing of Hg^{2+} and Cu^{2+} ions in EtOH/HEPES buffer medium (5 mM, pH = 7.34, 1:1, *v*/*v*). Probe **L1H** shows a good sensitive and selective *turn off* response in the presence of both Hg^{2+} and Cu^{2+} ions, which is comprehensible under long UV light. Its sensitivity was evaluated in different pH medium and in presence of other metal ions. Paper strip experiments and in-vitro cell imaging was done to know the sensitivity of the probe towards the metal ions in different environment. Chapter 3 describes the probe 2,6-di(2-pyridyl)-1,5-dihydroimidazo[4,5-*f*]benzimidazole (**L2H$_2$**) and its sensing application towards metal ions. This probe could detect Zn^{2+} and Cd^{2+} ions in three different aqueous systems viz., water, DMSO/HEPES buffer (1:1, *p*H = 7.34, rt), and DMSO/water (1:1, rt). In water a "*turn-on*" response was observed for both metal ions, whereas in the latter two solvent systems, a ratiometric change in fluorescence maximum was observed. The detection limit of this probe was as low as 0.3 μM and 0.62 μM (in water) for Zn^{2+} and Cd^{2+} ions, respectively. In Chapter 4 synthesis and evaluation of a novel probe *N*'-(pyren-1-ylmethylene)benzo[*d*]imidazo[2,1-*b*]thiazole-2-carbohydrazide (**L3H**) as metal ion sensor was explored. It was found to be able to nanomolar detection of Pd^{2+} and Ni^{2+} ions by colorimetric change. This probe was also able to detect the presence of Pd^{2+} ions in drug samples and APIs without any major interference. LOD values were calculated to be 46.1 to 93.9 nM (4.9 to 6.0 ppb) for $PdCl_2$ and 10.6 to 19.6 nM (1.1 to 2.1 ppb) for $Pd(PPh_3)_2Cl_2$ and 9.301 nM for $NiCl_2$ solutions. It also showed extremely good recovery of Pd^{2+} in presence of all the drug molecules. In Chapter 5 another novel ligand **L4H** based on 2,7-dichlorofluorescein was synthesized and evaluated for sensing applications. It was found to be able to detect Co^{2+} and Cu^{2+} ions differentially by different colouration of the solution in presence of these two metal ions. *In situ* Cu-complex of the ligand was utilised for quantification of amino acids like BSA and HSA proteins. Its differential selectivity paved the for molecular logic gate application.

Abbreviations:

API: Active Pharmaceuticals Ingredients

HOMO: Highest Occupied Molecular Orbitals

LUMO: Lowest Un-occupied Molecular Orbitals

TDDFT: Time Dependent Density Functional Theory

ARB: Angiotensin Receptor Blockers

PDE: Permitted Daily Exposure

HEPES: 4-(2-Hydroxyethyl)-1-piperazine ethanesulfonic acid

EDTA: Ethylenediaminetetraacetate

DMSO: Dimethyl sulfoxide

ACN: Acetonitrile

HSA: Human Serum Albumine

BSA: Bovine Serum Albumine

NMR: Nuclear Magnetic Resonance

FT-IR: Fourier Transformed-Infra Red

HRMS: High Resolution Mass Spectra

ESI: Electro Spray Ionisation

LOD: Limit of Detection

LOQ: Limit of Quantification

WHO: World Health Organisation

US EPA: United States Environmental Protection Agency

EMA: European Medicines Agency

Table of Contents

Chapter 5

Selective colorimetric detection of Co^{2+} and Cu^{2+} ions by a 2,7-dichlorofluorescein based ligand: use of its in situ Cu-complex for estimation of BSA and HSA proteins

Chapter 1

Introduction, Materials and Methods

Abstract:

In this chapter, an in-depth study about the adverse effects of over accumulation of metals in the environment that may lead to several diseases in human beings, animals and plants is contemplated. Importance of detection of such contaminants and the existing procedures for such detection have been discussed. Possibilities of colorimetric and fluorometric sensors being better alternative of these existing costly procedures were also studied. Recent works regarding application of sensors in the field of medicinal chemistry along with other biological applications is also thoughtfully examined. Thorough research objective have also been proposed based on the previous discussions. The materials used in this study, their commercial sources, methods regarding spectrophotometric data collection, specification, make and models of the instrument used in the experiments, crystallographic data collection and theoretical calculations using Gaussian 16 package are also briefed at the end.

Introduction:

1.1 Metals and pollution

Discovery of metals and their potential uses in day-to-day life is one of the most significant discoveries in human history. It shapes our civilization as the metals find their uses for their tensile strength and rigidity, which is utilized for making structures, houses, utensils, engineering parts, automobiles, instruments, weapons and many more. In the medicinal fields, metals like sodium, aluminum, and zinc often serve as countercations to drug molecule[1]. Palladium and ruthenium catalysts are vital in synthesizing many complex organic drug molecules[2]. As trace elements, several metals are present in living beings, which help in enzymatic metabolism, oxygen transport, structure formation (bones and cell walls), hormonal secretion and antiviral activity[3]. Dietary intake of metal ion is necessary and happens through the consumption of natural food sources like fruits, grains, and meat. However, rapid industrialization, growth in the use of automobiles, rampant use of heavy metals in fertilizers, pesticides and insecticides, mining of metals etc., caused a substantial increase in the concentration of heavy metals on the earth's crust, water bodies and other natural resources[4]. Electronic wastes such as circuit boards in discarded household electronic appliances, printers, mobile phone, computers; CD drives and CDs, and soldering equipment contains a high concentration of toxic heavy metals such as Cd, Pb, As, Hg and Cu which are released into soil, water and air as a result of unorganized recycling process[5,6]. Natural sources of heavy metal pollution include weathering rock, soil erosion and volcanic activities[7,8]. As a result, diseases and physiological complications related to metal toxicity have become a significant concern, especially in the developing world. Due to the adverse impacts on human health, all the international and national agencies set up a maximum allowable exposure limit for each metal through food, drinking water and air[9,10]. Although essential metals are required as significant trace elemental components for different biological functions, overexposure or accumulation may lead to metal toxicity-induced physiological conditions beyond a limit. Some metal-specific toxicity is described along with the diseases that the metals induced.

Among all the metals that pollute the environment, when present in the environment in excess Cr, Ni, Co, Cu, Zn, Cd, Hg, Pb and As (metalloid) are the most responsible elements for metal-induced toxicity[11,12].

Chromium is the 21st most abundant material on earth's crust. Due to its stainless nature, it makes strong alloys like stainless steel. Chromated copper oxide is used for wood processing and leather tanning[13]. Cr inhalation increases the chance of lung cancer as an occupational hazard among the workers who work in industries related to chromate production, plating, pigments and ferrochrome production industries[14]. Apart from lung cancer Cr can cause other types of cancer as its most stable form, Cr(VI) i.e. CrO_4^{2-} is water soluble and can easily get into cells through carboxylate, sulfate and phosphate transporter [15]. Inside the cell, chromate gets reduced to Cr(III) in a step-wise mechanism generating reactive oxygen species(ROS) and both the ROS and Cr(III) can cause damage to the DNA which induces carcinogenicity inside the cell by making DNA-Cr(III) adduct, the oxidized form of DNA and DNA-protein cross linkage[16]. Among the metals listed above Hg, Pb and Cd are considered primarily toxic for their numerous adverse effects on human health. Hg can exist in three different forms: elemental, inorganic (Hg(II) and Hg(I)) and organometallic (CH_3HgCl and CH_3CH_2HgCl). All these three forms are toxic. Human exposure to elemental mercury happens from inhalation of mercury vapor from dental amalgam, thermometer, barometer and fossil fuel emission from industrial and automobile sources[17]. It can pass through blood-brain barriers to accumulate in the nerve cells, causing neurological problems[18] like lack of coordination and concentrations in the victims of mercury exposure. Three forms of mercury follow the toxicity order: organometallic Hg > inorganic > elemental mercury[19], where organometallic Hg is the most toxic form. Inorganic mercury i.e., Hg(II) and Hg(I), can bind with -SH, -carboxyl, phosphate and amino groups to form stable complexes with enzymes and proteins, making them irreversibly ineffective[20]. Chronic exposure of any form of Hg can cause cardiovascular problems, which may lead to hypertension and cardiomyopathy. The most lethal form of mercury is $(CH_3)_2Hg$, a few µL of which on the skin can cause death to an individual[17]. The most infamous case of mass Hg poisoning happened on the coast of Minamata in Japan, where people got sick after consuming seaborn fishes from the contaminated coastal water. The contamination happened due to industrial discharge to the seawater from the acetaldehyde factory[21,22]. Regarding metal-induced damage to the central nervous system (CNS), lead (Pb) plays a significant role among all other metals. Unlike Hg, elemental Pb does not pose significant harm to human health because of its non-bioavailability. However, higher oxidation states (Pb(II) and Pb(IV)) can dissolve in water, which paves the way to pass into the cell and interfere with the cellular mechanism. Lead poisoning causes damage to the liver, kidney and CNS. It contributes to delayed mental growth in children and slowing down motor nerve

conduction and headaches in adults [23,24]. Cadmium is another polluting heavy metal that is a threat to living beings due to its toxicity. Industrial wastes are the primary source of Cd released into the environment and can easily get into a living organism through water and food. Besides that, Cd is found in PVC products, color pigments, batteries, fossil fuel combustion exhaust gas, phosphate fertilizers *etc*. [25]. It is a non-essential metal known to disrupt many cellular mechanisms and lead to cancer development. Cadmium also creates oxidative stress by ROS generation, like hydroxide and superoxide radicals, as well as hydrogen peroxide molecules, which can react with biological macromolecules, thereby increasing the chance of developing cancer[26–28]. Cadmium also induces neurological diseases due to its neurotoxic properties[29–33]. People living in Cd-contaminated zones are often diagnosed with bone diseases; itai-itai diseases in the Jinzu river basin are well-known for extreme Cd toxicity[34].

Metal	Toxic Effects	Ref
Chromium	Kidney dysfunction, Lung Cancer, GI disorder	[35]
Mercury	CNS injuries, Renal dysfunctions, Hepatotoxicity	
Lead	Cardiovascular dysfunctions, Liver damage, Reduced pulmonary functions	
Cadmium	Degenerative bone disease, Kidney dysfunction, Liver damage, GI disorders, Lungs injuries	

Apart from the toxic heavy metals that pollute the earth, arsenic (As) is a metalloid that harms human health. Arsenic pollution happens through the contamination of groundwater where there is a natural source of arsenic. It mainly exists in two oxidation states As(III) and As(V); among them As(III) is the most toxic due to its reaction with critical thiols in proteins and inhibition of their activity[36]. ROS generation by arsenic metabolism inside cells increases human cancer risk[37].

1.2 Methods for detection and quantification of heavy metals:

As discussed in the previous section, hazardous metals pollute different biosphere components. So, detecting and quantifying heavy metals in the given samples is reasonably necessary. Several detection methods are being used for that purpose and they can be broadly classified into three categories: (a) spectroscopic detection, (b) electrochemical detection and (c) optical

detection[38,39]. Examples of spectroscopic techniques include Atomic Absorption Spectroscopy (AAS)[40,41], Inductively Coupled Plasma Mass Spectrometry (ICP-MS)[42,43], X-ray Fluorescence Spectroscopy (XFS)[44] and Inductively Coupled Plasma Optical Emission Spectroscopy (ICP-OES)[45] They are versatile but expensive detection techniques which require trained personnel. Flame atomic absorption spectroscopy is a relatively cheaper technique to detect metal from water samples[46–48]. Electrochemical detection is also very popular technique in the field of biosensors and it is broadly classified into three different types which are (i) conductometric, (ii) potentiometric and (iii) amperometric[49,50]. Among all the sensing techniques optical sensors are the cheapest and it is mainly classified in (i) colorimetric and (ii) fluorometric sensors.

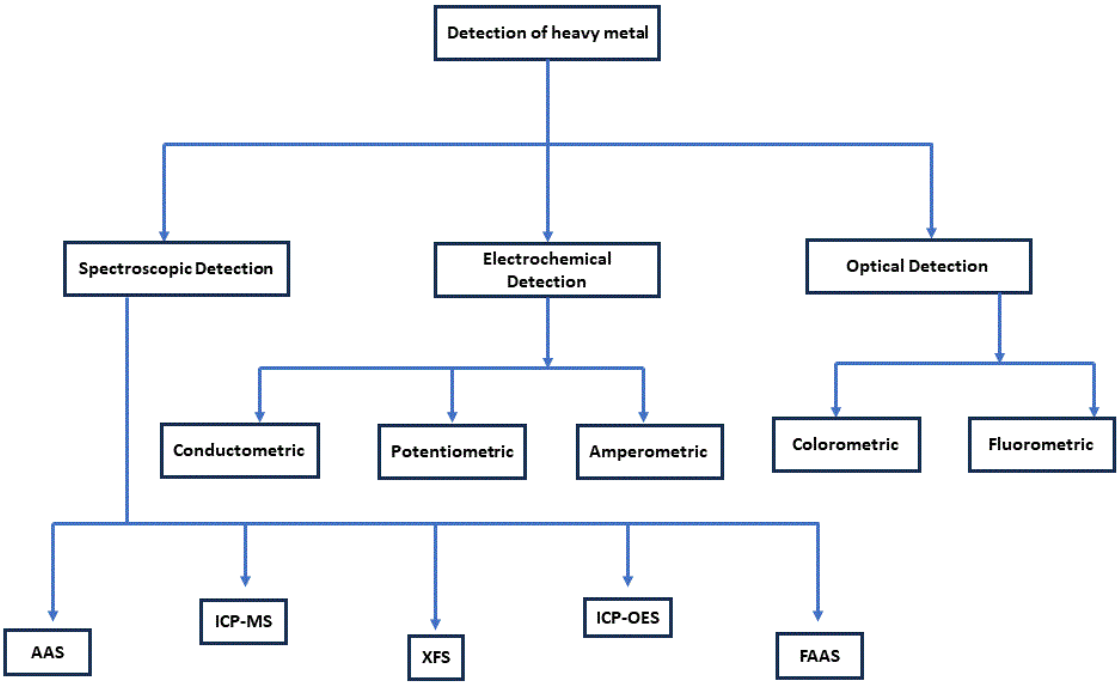

Figure 1 Classification of the detection techniques.

1.3 Fluorometric and colorimetric sensors

Numerous research groups are working on devising new and highly potent fluorometric and colorimetric sensors for detecting various metal ions, anions, biomolecules and macromolecules. Recent advancements in this field have been discussed as this thesis's research topics are syntheses and the application of small molecules for colorimetric and fluorometric detection of hazardous and polluting metal ions.

Colorimetric and fluorometric sensors require chromophores and fluorophores in the probe, responsible for specific absorption and emission bands, respectively. Many researchers have synthesized and utilized the derivatives of these chromophoric and fluorophoric subunits. Those subunits are 1,8-naphthalimide, fluorescein, rhodamine B and 6G, coumarin, pyrene, 8-hydroxyquinoline and many more. Derivatives of these subunits are synthesized with electron donor groups containing primarily N-, O- and S- donor sites that can capture specific metal cations from the solution, resulting in comprehensible shifts in spectral bands. There are different sensing mechanisms, which are Photo-induced Electron Transfer (PET), Fluorescence Resonance Energy Transfer (FRET), Excited State Intramolecular Proton Transfer (ESIPT), Intramolecular Charge Transfer (ICT), Twisted Intramolecular Charge Transfer (TICT).

1.3.1 1,8-Naphthalimide

1,8-Naphthalimide has been a favourite fluorophoric unit for its photophysical properties, including emission in red and infrared regions, significant stoke shift, and high quantum yield with two-photon absorption[51]. Several chemosensors containing 1,8-naphthalimide detect different metal ions depending on their structure and coordination

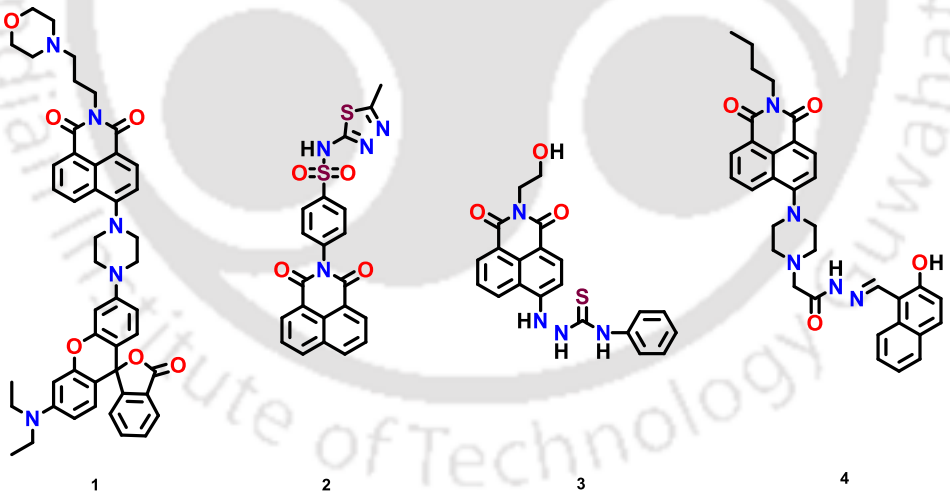

Figure 2. Chemosensors containing 1,8-naphthalimide.

. Liu *et al*. reported a highly selective naphthalimide -rhodamine-based sensor (**1**), which can target lysosomal Cu^{2+} in a ratiometric fluorescence response[52]. Bahta *et al*. and Lv *et al*. reported that Hg^{2+} sensors **2** and **3** contain 1,8-naphthalimide and do fluorescence detection of Hg^{2+} ratiometrically[53,54]. Kang and co-workers reported **4** being a ratiometric and fluorescent sensor of Al^{3+} ions[55].

1.3.2 Fluorescein

Fluorescein has been a popular chromophoric part of many dyes, quantum dots and chemosensors[56,57] for its absorption and emission in the visible range, the property that enhances the comprehensibility of an interaction between an analyte and the probe. Recent advances in devising new chemosensors for sensitive detection involve the incorporation of fluorescein moiety into chemosensors. Erdemir and co-workers synthesized a fluorescein-based chemosensor **5** that showed green fluorescence in the presence of Hg^{2+} ions[58]. Zhang *et al*. proposed a multi-functional dual-mode colorimetric sensor **6** for Pb^{2+} and Cd^{2+} ions with a molecular logic gate application[59]. A bi-fluorescein-based sensor **7** was developed by Rathod *et al*. for the selective detection of Cu^{2+} ions by emitting blue fluorescence[60]. Li Zhang and co-workers also developed a sensor **8** based on the same chromophore that detects Cu^{2+} colorimetrically[61].

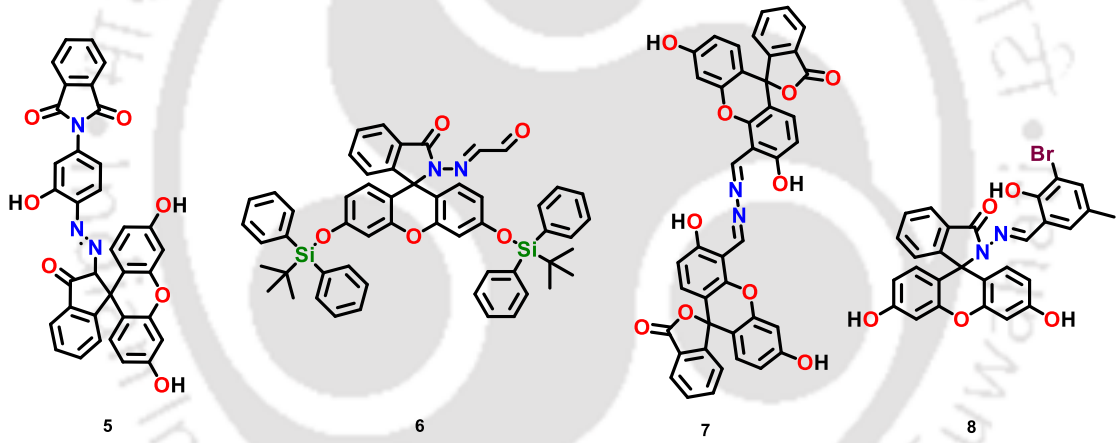

Figure 3: Chemosensors containing fluorescein.

1.3.3 Rhodamine B and 6G

Rhodamine B and 6G have the xanthene ring system which is analogous to fluorescein and share the similar photophysical characteristics. Because of this, a lot of rhodamine-based chemosensors have been reported.

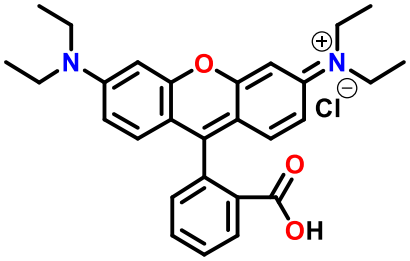

Rhodamine B

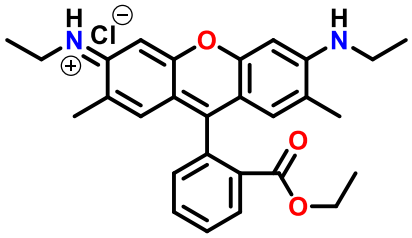

Rhodamine 6G

Rhodamine B can exist in cyclic and acyclic forms depending on the pH of the system. The central lactone ring has been found to stay in the open form in acidic pH but tends to go into the cyclic form (Scheme 1) when the pH has been increased[62].

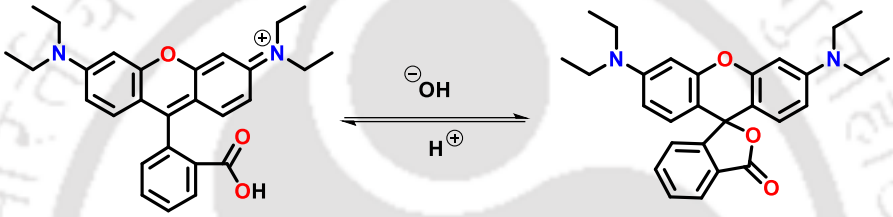

Scheme 1 Switching between cyclic and acyclic forms through regulation of pH.

A lot of reports have been published where the rhodamine scaffold is utilized as a fluorophoric part of the probe[63,64]. Some representative examples are given below.

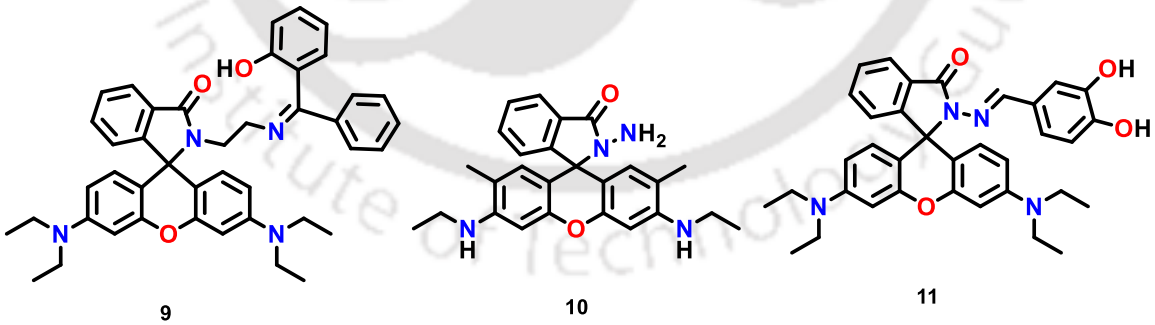

9 10 11

Figure 4 Chemosensors containing Rhodamine.

A rhodamine appended benzophenone probe **9** has been synthesized by Adak and co-workers. Their probe can detect Pd^{2+} ions in living cells by emitting pink fluorescence upon coordination with the metal ions with remarkable selectivity[65]. Xie *et al*. synthesized another rhodamine 6G hydrazide **10** can function as a sensor for detecting lead contaminants in soil, tap water and seafood in fluorescence and visualization mode[66]. The application of molecular logic gate

operation was reported by Chan *et al*., where a rhodamine B derived chemosensor **11** can detect Al^{3+} and Cu^{2+} ions both colorimetrically and fluorometrically[67]. The addition of EDTA to the *in situ* metal complex can free up the binding sites of the ligand, restoring its original photophysical property and that phenomenon was utilized to apply the probe as an INHIBIT logic gate.

1.3.4 Coumarin

Coumarin is another interesting fluorophore because of its diversity in functionalization at different positions of the coumarin ring system. Therefore, coumarin has been widely used for making fluorescent dyes, markers and sensors of different compounds. Mostly 3,4,7 and 8 positions (Figure 4) of coumarin ring are functionalized in order to make fluorescent probes[68].

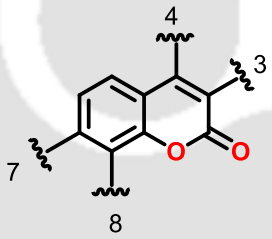

Figure 5. Coumarin ring and its positions of functionalizations.

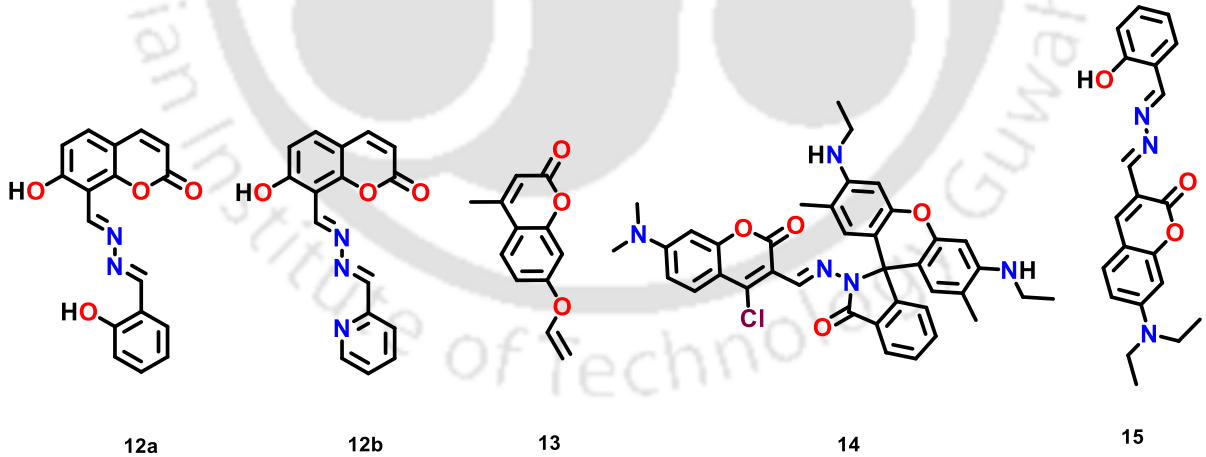

Figure 6. Chemosensors containing coumarin.

Chemosensor **12a** and **b**, examples of coumarin ring substituted at 8 position were synthesized by Jiaxin Fu *et al*. These probes can detect Zn^{2+} ions both colorimetrically and fluorometrically. **12a** emits yellow fluorescence and **12b** emits green fluorescence in the presence of Zn^{2+} ions[69]. Probe **13** is an example of a chemo dosimeter that reacted with Hg^{2+} to release 7-

hydroxy-4-methylcoumarin, which caused fluorescence enhancement[70]. Wu and co-workers reported this chemosensor. Many chemosensors were synthesized by joining two fluorophores through a spacer or connector. Gosi *et al*. reported a chemosensor **14** in which the coumarin and rhodamine 6G were connected through imine linkage. This chemosensor was reported as a dual sensor detecting Hg^{2+} and Cu^{2+} colorimetrically[71]. Chemosensor **15** was an example of 3-substituted coumarin as reported by Yeh *et al*. This probe can detect Cu^{2+} colorimetrically through the change of solution colour from light yellow to red. Whereas, the probe's fluorescence was quenched in the presence of the metal ions, making the probe a "*turn off*" fluorescence sensor[72].

1.3.5 Pyrene

Pyrene is a π-electron rich aromatic ring system that has been used as fluorophore in many probes used as chemosensor. It has interesting photophysical properties with relatively long lifetime, which contributes to the fluorescence sensing of analytes.

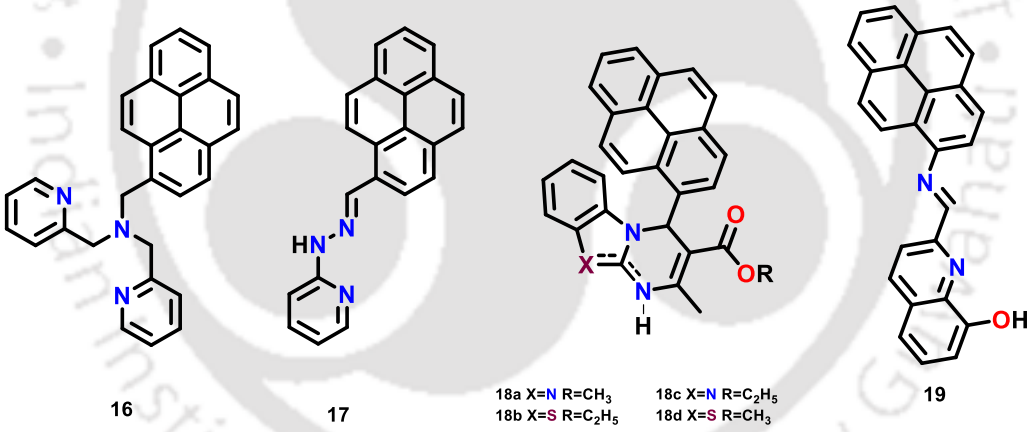

Figure 7 Chemosensors containing pyrene.

Phapale *et al*. had reported a chemosensor **16** that can colorimetrically detect Cu^{2+} and Fe^{3+} ions differentially. In presence of Cu^{2+} ion, the solution color turned green whereas Fe^{3+} changed the colour of the solution from colourless to light brown[73]. The chemosensor **17** showed remarkable selectivity towards Cu^{2+} ions as there was "*turn on*" response in presence of the metal ions. This probe, reported by Venkatesan *et al*., was unique in its photophysical property as Cu^{2+} is generally known as a quencher of fluorescence for its paramagnetic nature. But in this case the coordination of the probe with Cu^{2+} switched off the photoinduced electron transfer (PET) process and that caused enhancement of the fluorescence intensity[74]. Tilak Raj

et al. had synthesized compound **18a -18d** among those **18a** and **18c** could differentially detect Zn^{2+} in organic medium and Fe^{3+} in aqueous medium. In organic solvent, **18a** and **18c** got bound with Zn^{2+} disrupting the excimer of the probes, which caused quenching of the excimer peak and increment of the monomer peak. Whereas organic nanoparticles of **18a** and **18c** formed in aqueous medium showed enhancement of the fluorescence intensity due to aggregation induced enhanced emission (AIEE) and it was quenched in the presence of Fe^{3+} ions[75]. Mukherjee *et al*. synthesized chemosensor **19** which can selectively detect Fe^{3+} ions. The fluorescence of the probe rapidly increased in the presence of the metal ions due to CHEF (Chelation Enhanced Fluorescence) effect[76].

There are numerous fluorescent probes reported by researchers all over the globe that can detect a specific metal cation and show comprehensible change. Some significant probes are summarised above to show case the utility and function of the fluorophores in devising sensing strategy.

1.4 Application of chemosensors for other analytes

Chemosensors were not only been used in detection of the metal ions but it has found wide utilization in the detection of anions, biologically important macromolecules like biothiols, amino acids, neurotransmitters, carbohydrates, nucleotides, nucleoside phosphate, oligonucleotides, lipids, steroids and drugs[77,78]. Chemosensors were also used in the detection of nitro aromatics that were used in making explosives[79]. Several biosensors were used to diagnose viral infection from the detection of surface protein, viral protein and genetic material of mammalian viruses like dengue, human immunodeficiency virus (HIV), zika virus, hepatitis virus and influenza virus. A brief discussion on the detection of the above-mentioned analytes is as follows.

1.4.1 Amino acids

Ninhydrin (**20**) has been a famous and usual choice for the detection of primary amino acids. In presence of primary amino acids, it gives a deep purple colour known as Ruhemann's purple (Scheme 2). It is, to date, the most used probe for the detection of primary amino acids. Among the significant recent examples of the probe for the detection of the amino acids are the meso-ester BODIPY motifs (**21** & **22**) proposed by Bouffard and co-workers. It got bound strongly with amino acid -NH_2 group and a nearly 3000-fold increase in the emission intensity along with change in emission wavelength was also observed[80].

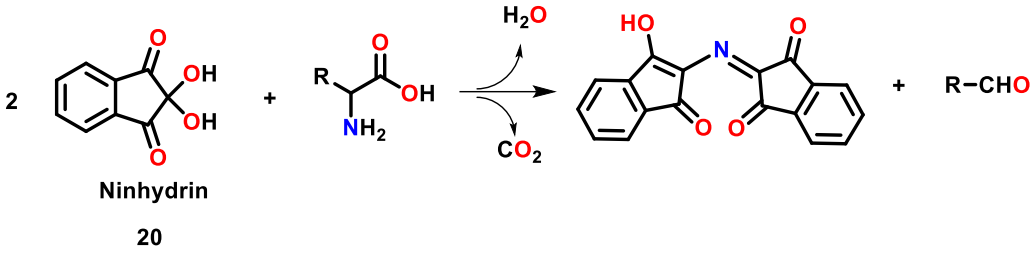

Scheme 2

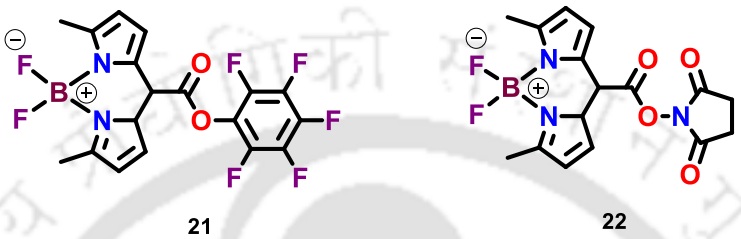

Figure 8 Chemosensors for amino acid detection.

1.4.2 Anions

Like many heavy metals, some inorganic anions are harmful to living beings. Cyanide, sulfide and fluoride are prime examples of such anions that are potential pollutants of nature and the environment.

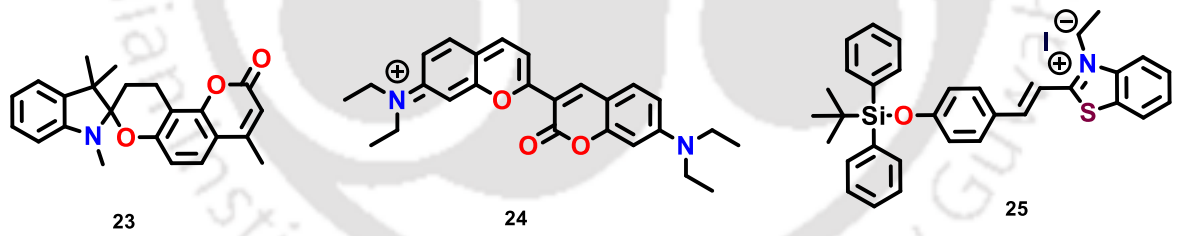

Shiraishi and co-workers had synthesized[81] compound **23** which can detect CN^- exclusively by enhancing the fluorescence intensity after opening of the spiropyran ring after nucleophilic attack by the CN^-. Compound **24** was proposed by Guo *et al*. as a thiol sensor which consisted of two coumarin rings. The emission changed from NIR to visible upon the addition of the H_2S to the system[82]. Zhu *et al*. projected **25** as a fluoride sensor that can detect the presence of F^- both colorimetrically and fluorometrically[83].

1.5 Objective of the thesis

Inspired by the literature survey, an attempt has been made to explore the photophysical properties of 2,4,5-tris(2-pyridyl)imidazole in the presence of various metal ions in Chapter 2

of the thesis. In Chapter 3, further exploration of a benzobisimidazole based ligand towards selectivity of specific metal ions was done. In Chapters 4 and 5 two novel ligands were synthesized and scrutinized for their colorimetric response towards specific metal ions. In Chapter 4, the ligand was also employed in the detection of metal ion in the presence of the drug samples. In Chaper 5, the 2,7-dichlorofluorescein based ligand was further used for the quantification of protein and molecular logic gate operation.

1.6 Materials and Methods

1.6.1 General Information and Materials

All the chemicals and solvents (EtOH, MeOH, MeCN and DMSO) were purchased from Merck India and used without further purification. Deionized water which is obtained from Mili-Q Reference Water Purification System, was used to prepare HEPES buffer. An Agilent Cary 100 and a Perkin Elmer Lambda 365 spectrophotometer were used to record the absorption spectra in the 200-600 nm range in quartz a cuvette of path length 1 cm. A Horiba Fluoromax-4 spectrofluorometer was used to record emission spectra with a 1 cm pathlength quartz fluorescence cuvette. We used Pico Second Time Resolved Fluorimeter Lifespec II by Edinburgh Instruments for the time-resolved photoluminescence study. NMR spectra were recorded using Bruker Ascend 600 MHz NMR spectroscopic system calibrated with reference of 0.03 % (v/v) TMS mixed with deuterated solvent. Mass spectrometry was done by Agilent QTOF6520 and Agilent 6546A series High Resolution Mass Spectrometers.

1.6.2 Absorbance and Emission Spectroscopic Studies:

Spectroscopic studies were done in solvent/HEPES buffer (5mM, pH = 7.34, *v*/*v*) (solvent = EtOH, DMSO and CH_3CN) unless otherwise specified. All the metal chloride except $PdCl_2$ salts are dissolved in deionized water to make stock solutions (1.0×10^{-3} M). Stock solutions of the probes were prepared in EtOH or DMSO (1.0×10^{-3} M) and used for UV-Vis and fluorescence studies. A 3 mL of solvent/HEPES buffer solution was placed a quartz cuvette of 1 cm path length and the appropriate amount of stock solution of the probe was added to make a dilute (1.315×10^{-5} M) solution for both the absorption and emission studies. The UV-vis and fluorescence titration experiment was carried out by adding stock solution of metal chloride solution to the diluted solution of the probe and each data was taken within 1 min of addition. Absorption spectra were recorded within a range of 200-600 nm. For fluorescence studies, the

excitation beam of 308 nm (Chapter 2) and 354 nm (Chapter 3) were used with a slit length of 2 nm. The emission was recorded in the range of 328-598 nm (Chapter 2) and 365-620 nm (Chapter 3). Na_2EDTA solution (1.0×10^{-3} M) was prepared in deionized water to test the probe's reversibility. The Na_2EDTA solution was added after each addition of detectable cation solution to the buffered solution of the probes.

1.6.3 Fluorescence quantum yield calculation:

1.6.3.1 Absolute method

We carried out fluorescence quantum yield calculation by Petite Integrating Sphere Method with the help of Horiba Jobin Yvon Fluoromax-4 Spectrofluorometer. The experiment was done in EtOH/HEPES buffer medium for **L1H**, **L1H**-Cu complex and **L1H**-Hg Complex at the excitation wavelength of 308 nm. The following equation was used to calculate the absolute quantum yield (φ).

$$\varphi = \frac{E_C - E_A}{L_A - L_C} \quad (1)$$

E_C = Emission of the Sample, E_A = Emission of the Blank, L_C = Light scattering of the Sample and L_A = Light scattering of the Blank.

1.6.3.2 Relative method

A reference solution of quinine sulphate was prepared by dissolving the minuscule amount of it was dissolved in 1 mL of 0.1 M H_2SO_4 such that O.D. value under 0.1in 3 mL 0.1 M H_2SO_4 in the absorption spectrum and emission spectrum of the same sample was also recorded. Same procedure was repeated for getting the absorption and emission data of **L2H₂**, Zn- **L2H₂** and Cd- **L2H₂** in water, DMSO/Water (1:1) and DMSO/HEPES buffer (5 mM, pH = 7.34, 1:1, *v*/*v*) solutions.

The following equation was employed for determination of Quantum Yield (Φ).

Φ of **L2H₂** (or its complexes) = Φ_{ref} × (Area under the emission spectrum of **L2H₂** / Area under the emission spectrum of **Ref**) × (Absorbance of **Ref** / Absorbance of **L2H₂**) × (Refractive index of **L2H₂** / Refractive index of **Ref** solution) (2)

1.6.4 Stern Volmer Plot:

Following the standard procedure I_0/I was plotted against the concentration of the metal ion where I_0 is the fluorescence intensity of the **L1H** and I is the fluorescence intensity after addition of the metal ion solution to the buffered solution of **L1H**.

$$I/I_0 = K_{SV}[\mathbf{M}] + 1 \quad (3)$$

[**M**] = Concentration (mol L^{-1}) of metal ion

1.6.5 Time resolved photo luminescence study:

For the lifetime measurement of the ligand **L1H** and its complexes (**L1H**-Cu and **L1H**-Hg) 308 nm of LED diode was used as source. For **L2H₂** and its complexes 375 nm laser source was used.

1.6.6 Determination of Limit of Detection:

Limit of detection was determined following the standard procedure. Standard deviation of the replicate data of fluorescence intensity of the emission maxima which was taken 20 times in 2 min interval, was calculated. Slope of the fitted curve was calculated after plotting the fluorescence intensity of the probe after each addition vs the concentration of the respective metal chloride solution. Following equation was employed for the calculation of the limit of detection of the probe for the respective metal ions.

$$LOD = \frac{3\sigma}{k} \quad (4)$$

1.6.7 Determination of the binding stoichiometry:

The binding stoichiometry of the ligand probes with metal ions were determined by (i) Job's Plot and (ii) Mass spectrometry. The binding constant was calculated from the Benesi-Hildebrand plot. The method of continuous variation of mole fraction was used to plot the Job's plot and the ratio was determined accordingly.

The equation that follows was employed to determine the binding constants.

$$\frac{1}{I - I_0} = \frac{1}{K_b(I_0 - I_{min})} \frac{1}{[Cu^{2+}]\ or\ [Hg^{2+}]} + \frac{1}{I_0 - I_{min}} \quad (5)$$

$$y = mx + c \quad (6)$$

Where I = Fluorescence intensity with respect to a definite concentration of metal ion
I_0 = Fluorescence intensity of the probe in the absence of any metal ion
K_b = Binding constant or the rate constant of complexation
I_{min} = Fluorescence intensity of the probe in the fully quenched state

1.6.8 NMR titration experiment:

A solution of probes was prepared by dissolving 20 mg of it in 600 µL of DMSO-d_6 and the metal chloride solutions of same concentration were also prepared in same solvent. The ligand solution was titrated against the metal solutions under gradual addition of the same.

1.6.9 Computational studies:

All the theoretical calculations were done by Gaussian 16 program [84] and visualized by Gaussview 06 software [85]

The optimized structure of the **L1H** and its complexes were obtained by gaussian calculation performed by Gaussian16 software program. The ligand **L1H**'s structure was optimized in 6-31G basis set on B3LYP level. The complexes of **L1H** were optimized in LanL2DZ basis set on B3LYP level.

The ligand **L2H$_2$**'s structure was optimized in 6-31G basis set on B3LYP level. The complexes of **L2H$_2$** were optimized in LanL2DZ basis set on B3LYP level. TD-DFT calculation was also done in in the same basis sets.

Optimization of molecular structures and the TD-DFT energy calculation of **L3H**, [Pd(**L3**)(CH_3CN)Cl] and [Ni(**L3H**)(H_2O)(CH_3CN)Cl_2] were done. Both the calculations were performed at B3LYP level using 6-31+G(d,p) basis set for **L3H** and in LANL2DZ for complexes. All the calculations were done by incorporating acetonitrile as the solvent in the CPCM continuum solvation model. The theoretical electronic spectra were obtained by using the result of TD-DFT energy calculations.

Optimization and TD-DFT calculations of **L4H** were done in B3LYP level using 6-31+G(d,p) basis set. For theoretical calculation [Cu(**L4**)(H_2O)]$^+$ and [Co(**L4**)$_2$]$^+$ complexes were taken based on the experimental results. For optimization and TD-DFT calculaions of [Cu(**L4**)(H_2O)]$^+$ LanL2DZ basis set was used at B3LYP level. Whereas, in the case of [Co(**L4**)$_2$]$^+$ complex the optimization was done by modelling the Co metal centre by LanL2DZ and other atoms by 6-31G(d,p) in GEN basis set at B3LYP level. TD-DFT calculation of the same was done in LanL2DZ basis set at B3LYP level.

1.6.10 Appendices

The Chapter appendix containing relevant supporting materials has been added at the end of the references of each of the Chapters.

References:

[1] D. Gupta, D. Bhatia, V. Dave, V. Sutariya, S. V. Gupta, *Molecules* **2018**, *23*, 1719

[2] R. Emadi, A. Bahrami Nekoo, F. Molaverdi, Z. Khorsandi, R. Sheibani, H. Sadeghi-Aliabadi, *RSC Adv.* **2023**, *13*, 18715–18733.

[3] National Research Council (US) Committee on Diet and Health., in *Diet and Health: Implications for Reducing Chronic Disease Risk.*, National Academies Press (US), Washington (DC), **1989**.

[4] J. Briffa, E. Sinagra, R. Blundell, *Heliyon* **2020**, *6*, e04691.

[5] S. Arya, R. Rautela, D. Chavan, S. Kumar, *Process Saf. Environ. Prot.* **2021**, *152*, 641–653.

[6] S. C. Chakraborty, M. Qamruzzaman, M. W. U. Zaman, M. M. Alam, M. D. Hossain, B. K. Pramanik, L. N. Nguyen, L. D. Nghiem, M. F. Ahmed, J. L. Zhou, M. I. H. Mondal, M. A. Hossain, M. A. H. Johir, M. B. Ahmed, J. A. Sithi, M. Zargar, M. A. Moni, *Process Saf. Environ. Prot.* **2022**, *162*, 230–252.

[7] P. B. Tchounwou, C. G. Yedjou, A. K. Patlolla, D. J. Sutton, in *Molecular, Clinical and Environmental Toxicology: Volume 3: Environmental Toxicology* (Ed.: A. Luch), Springer Basel, Basel, **2012**, pp. 133–164..

[8] J. O. Duruibe, M. O. C. Ogwuegbu, Egwurugwu, *Int. J. Phys. Sci.* **2007**, *2*, 112–118.

[9] *Guidelines for Drinking-Water Quality: Fourth Edition Incorporating the First Addendum. Licence: CC BY-NC-SA 3.0 IGO.*, Geneva, **2017**.

[10] C. Griffiths, H. Klemick, M. Massey, C. Moore, S. Newbold, D. Simpson, P. Walsh, W. Wheeler, *Rev. Environ. Econ. Policy* **2012**, *6*, 130–146.

[11] H. N. M. Ekramul Mahmud, A. K. Obidul Huq, R. B. Yahya, *RSC Adv.* **2016**, *6*, 14778–14791.

[12] M. Balali-Mood, K. Naseri, Z. Tahergorabi, M. R. Khazdair, M. Sadeghi, *Front. Pharmacol.* **2021**, *12*, 643972.

[13] J. Barnhart, *Regul. Toxicol. Pharmacol.* **1997**, *26*, S3–S7.

[14] D. M. Proctor, M. Suh, S. L. Campleman, C. M. Thompson, *Toxicology* **2014**, *325*, 160–179.

[15] H. Hossini, B. Shafie, A. D. Niri, M. Nazari, A. J. Esfahlan, M. Ahmadpour, Z. Nazmara, M. Ahmadimanesh, P. Makhdoumi, N. Mirzaei, E. Hoseinzadeh, *Environ. Sci. Pollut. Res.* **2022**, *29*, 70686–70705.

[16] T. L. DesMarias, M. Costa, *Curr. Opin. Toxicol.* **2019**, *14*, 1–7.

[17] K. M. Rice, E. M. Walker Jr, M. Wu, C. Gillette, E. R. Blough, *J. Prev. Med. Public Health* **2014**, *47*, 74–83.

[18] B. Fernandes Azevedo, L. Barros Furieri, F. M. I. Peçanha, G. A. Wiggers, P. Frizera Vassallo, M. Ronacher Simões, J. Fiorim, P. Rossi De Batista, M. Fioresi, L. Rossoni, I. Stefanon, M. J. Alonso, M. Salaices, D. Valentim Vassallo, *J. Biomed. Biotechnol.* **2012**, *2012*, 1-11.

[19] A. Kungolos, I. Aoyama, S. Muramoto, *Ecotoxicol. Environ. Saf.* **1999**, *43*, 149–155.

[20] T. W. Clarkson, *Environ. Health Perspect.* **1987**, *75*, 59–64.

[21] P. Li, X. B. Feng, G. L. Qiu, L. H. Shang, Z. G. Li, *J. Hazard Mater.* **2009**, *168*, 591–601.

[22] L. D. Hylander, M. E. Goodsite, *Sci.Total Environ.* **2006**, *368*, 352–370.

[23] A. L. Wani, A. Ara, J. A. Usmani, *Interdiscip. Toxicol.* **2016**, *8*, 55–64.

[24] M. S. Collin, S. K. Venkatraman, N. Vijayakumar, V. Kanimozhi, S. M. Arbaaz, R. G. S. Stacey, J. Anusha, R. Choudhary, V. Lvov, G. I. Tovar, F. Senatov, S. Koppala, S. Swamiappan, *J. Hazard Mater.* **2022**, *7*, 100094.

[25] G. Genchi, M. S. Sinicropi, G. Lauria, A. Carocci, A. Catalano, *Int. J. Environ. Res. Public Health* **2020**, *17*, 3782.

[26] J. Liu, W. Qu, M. B. Kadiiska, *Toxicol. Appl. Pharmacol.* **2009**, *238*, 209–214.

[27] A. Rani, A. Kumar, A. Lal, M. Pant, *Int. J. Environ. Health Res.* **2014**, *24*, 378–399.

[28] J. M. Moulis, F. Thévenod, *BioMetals* **2010**, *23*, 763–768.

[29] B. Wang, Y. Du, *Oxid. Med. Cell Longev.* **2013**, *2013*, 898034.

[30] G. Notarachille, F. Arnesano, V. Calò, D. Meleleo, *BioMetals* **2014**, *27*, 371–388.

[31] B. Wang, Y. Du, *Oxid. Med. Cell Longev.* **2013**, *2013*, 1-12.

[32] A. Minami, A. Takeda, D. Nishibaba, S. Takefuta, N. Oku, *Brain Res.* **2001**, *894*, 336–339.

[33] M. K. Viaene, R. Masschelein, J. Leenders, L. J. V. C. Swerts, M. de Groof, H. A. Roels, *Occup. Environ. Med.* **2000**, *57*, 19–27.

[34] L. Järup, *Nephrol. Dial. Transplant.* **2002**, *17*, 35–39.

[35] M. Balali-Mood, K. Naseri, Z. Tahergorabi, M. R. Khazdair, M. Sadeghi, *Front. Pharmacol.* **2021**, *12*, 1-19.

[36] M. F. Hughes, *Toxicol. Lett.* **2002**, *133*, 1–16.

[37] H. Shi, X. Shi, K. J. Liu, *Mol. Cell Biochem.* **2004**, *255*, 67–78.

[38] L. A. Malik, A. Bashir, A. Qureashi, A. H. Pandith, *Environ. Chem. Lett.* **2019**, *17*, 1495–1521.

[39] S. J. Hill, *Chem. Soc. Rev.* **1997**, *26*, 291.

[40] M. Arienzo, R. Capasso, *J. Agric. Food Chem.* **2000**, *48*, 1405–1410.

[41] M. E. Conti, F. Botrè, *Food Control* **1997**, *8*, 131–136.

[42] A. A. Ammann, *Anal. Bioanal. Chem.* **2002**, *372*, 448–452.

[43] N. Lewen, S. Mathew, M. Schenkenberger, T. Raglione, *J. Pharm. Biomed. Anal.* **2004**, *35*, 739–752.

[44] J. Q. McComb, C. Rogers, F. X. Han, P. B. Tchounwou, *Water Air Soil Pollut.* **2014**, *225*, 2169.

[45] K. Uysal, Y. Emre, E. Köse, *Microchem. J.* **2008**, *90*, 67–70.

[46] A. R. Ipeaiyeda, A. R. Ayoade, *Appl. Water Sci.* **2017**, *7*, 4449–4459.

[47] Y. Bakırcıoğlu, S. Akman, N. Bıçak, F. Şenkal, *J. Trace Microprobe Tech.* **2003**, *21*, 239–248.

[48] Ş. Tokalioğlu, Ş. Kartal, L. Elçi, *Anal. Chim. Acta.* **2000**, *413*, 33–40.

[49] D. Grieshaber, R. MacKenzie, J. Vörös, E. Reimhult, *Sensors* **2008**, *8*, 1400–1458.

[50] J. Baranwal, B. Barse, G. Gatto, G. Broncova, A. Kumar, *Chemosensors* **2022**, *10*, 363.

[51] N. Jain, N. Kaur, *Coord. Chem. Rev.* **2022**, *459*, 214454.

[52] C. Liu, X. Jiao, S. He, L. Zhao, X. Zeng, *Org. Biomol. Chem.* **2017**, *15*, 3947–3954.

[53] B. Muzey, A. Naseem, *J. Photochem. Photobiol. A Chem.* **2020**, *391*, 112354.

[54] F. Lv, Y. Chen, T. Tang, Y. Chen, D. Xu, *J. Fluoresc.* **2017**, *27*, 1285–1292.

[55] L. Kang, Y. T. Liu, N. N. Li, Q. X. Dang, Z. Y. Xing, J. L. Li, Y. Zhang, *J. Lumin.* **2017**, *186*, 48–52.

[56] K. S, B. Sam, L. George, S. Y. N, A. Varghese, *J. Fluoresc.* **2021**, *31*, 1251–1276.

[57] Aruna, V. P. Verma, A. P. Singh, R. Shrivastava, *J. Mol. Struct.* **2024**, *1295*, 136549.

[58] S. Erdemir, D. Aydin, O. Kocyigit, *Mater. Chem. Phys.* **2023**, *310*, 128376.

[59] Y. Zhang, L. Chen, J. Yang, Y. Zhang, M.-S. Yuan, *Spectrochim. Acta A Mol. Biomol. Spectrosc.* **2020**, *232*, 118163.

[60] R. V. Rathod, S. Bera, M. Singh, D. Mondal, *RSC Adv.* **2016**, *6*, 34608–34615.

[61] L. Zhang, X. Zhang, *Spectrochim. Acta A Mol. Biomol. Spectrosc.* **2014**, *133*, 54–59.

[62] O. M. Obukhova, N. O. Mchedlov-Petrossyan, N. A. Vodolazkaya, L. D. Patsenker, A. O. Doroshenko, *Colorants* **2022**, *1*, 58–90.

[63] Y. Wang, X. Wang, W. Ma, R. Lu, W. Zhou, H. Gao, *Chemosensors* **2022**, *10*, 399.

[64] P. Ghosh, P. Roy, *Chem. Commun.*. **2023**, *59*, 5174–5200.

[65] A. K. Adak, B. Dutta, S. K. Manna, C. Sinha, *ACS Omega* **2019**, *4*, 18987–18995.

[66] X. Xie, M. Pan, L. Hong, K. Liu, J. Yang, S. Wang, S. Wang, *J. Agric. Food Chem.* **2021**, *69*, 7209–7217.

[67] W. C. Chan, H. M. Saad, K. S. Sim, V. S. Lee, K. W. Tan, *J. Mol. Struct.* **2022**, *1254*, 132337.

[68] X. Sun, T. Liu, J. Sun, X. Wang, *RSC Adv.* **2020**, *10*, 10826–10847.

[69] J. Fu, K. Yao, B. Li, H. Mei, Y. Chang, K. Xu, *Spectrochim. Acta A Mol. Biomol. Spectrosc.* **2020**, *228*, 117790.

[70] C. Wu, J. Wang, J. Shen, C. Bi, H. Zhou, *Sens. Actuators B Chem.* **2017**, *243*, 678–683.

[71] M. Gosi, A. C. Kumar, Y. Sunandamma, *J. Fluoresc.* **2022**, *32*, 2379–2393.

[72] J.-T. Yeh, W.-C. Chen, S.-R. Liu, S.-P. Wu, *New J. Chem.* **2014**, *38*, 4434–4439.

[73] D. Phapale, A. Gaikwad, D. Das, *Spectrochim. Acta A Mol. Biomol. Spectrosc.* **2017**, *178*, 160–165.

[74] P. Venkatesan, S.-P. Wu, *RSC Adv.* **2015**, *5*, 42591–42596.

[75] T. Raj, P. Saluja, N. Singh, *Sens. Actuators B Chem.* **2015**, *206*, 98–106.

[76] S. Mukherjee, S. Talukder, *J. Fluoresc.* **2016**, *26*, 1021–1028.

[77] J. Krämer, R. Kang, L. M. Grimm, L. De Cola, P. Picchetti, F. Biedermann, *Chem. Rev.* **2022**, *122*, 3459–3636.

[78] M. H. Lee, Z. Yang, C. W. Lim, Y. H. Lee, S. Dongbang, C. Kang, J. S. Kim, *Chem. Rev.* **2013**, *113*, 5071–5109.

[79] Y. Salinas, R. Martínez-Máñez, M. D. Marcos, F. Sancenón, A. M. Costero, M. Parra, S. Gil, *Chem. Soc. Rev.* **2012**, *41*, 1261–1296.

[80] S. Jeon, T.-I. Kim, H. Jin, U. Lee, J. Bae, J. Bouffard, Y. Kim, *J. Am. Chem. Soc.* **2020**, *142*, 9231–9239.

[81] Y. Shiraishi, M. Nakamura, N. Hayashi, T. Hirai, *Anal. Chem.* **2016**, *88*, 6805–6811.

[82] J. Liu, Y. Sun, J. Zhang, T. Yang, J. Cao, L. Zhang, W. Guo, *Chem. Eur. J.* **2013**, *19*, 4717–4722.

[83] B. Zhu, F. Yuan, R. Li, Y. Li, Q. Wei, Z. Ma, B. Du, X. Zhang, *Chem. Commun.* **2011**, *47*, 7098.

[84] Gaussian 16, Revision C.01, M. J. Frisch, G. W. Trucks, H. B. Schlegel, G. E. Scuseria, M. A. Robb, J. R. Cheeseman, G. Scalmani, V. Barone, G. A. Petersson, H. Nakatsuji, X. Li, M. Caricato, A. V. Marenich, J. Bloino, B. G. Janesko, R. Gomperts, B. Mennucci, H. P. Hratchian, J. V. Ortiz, A. F. Izmaylov, J. L. Sonnenberg, D. Williams-Young, F. Ding, F. Lipparini, F. Egidi, J. Goings, B. Peng, A. Petrone, T. Henderson, D. Ranasinghe, V. G. Zakrzewski, J. Gao, N. Rega, G. Zheng, W. Liang, M. Hada, M. Ehara, K. Toyota, R. Fukuda, J. Hasegawa, M. Ishida, T. Nakajima, Y. Honda, O. Kitao, H. Nakai, T. Vreven, K. Throssell, J. A. Montgomery, Jr., J. E. Peralta, F. Ogliaro, M. J. Bearpark, J. J. Heyd, E. N. Brothers, K. N. Kudin, V. N. Staroverov, T. A. Keith, R. Kobayashi, J. Normand, K. Raghavachari, A. P. Rendell, J. C. Burant, S. S. Iyengar, J. Tomasi, M. Cossi, J. M. Millam, M. Klene, C. Adamo, R. Cammi, J. W. Ochterski, R. L. Martin, K. Morokuma, O. Farkas, J. B. Foresman, and D. J. Fox, Gaussian, Inc., Wallingford CT, **2016**.

[85] GaussView, Version 6.1, Roy Dennington, Todd A. Keith, John M. Millam, Semichem Inc., Shawnee Mission, KS, **2016**.

Chapter 2

Application of 2,4,5-tris(2-pyridyl)imidazole as '*turn off*' fluorescence sensor for Cu(II) and Hg(II) ions and *in vitro* cell imaging*

Abstract:

The 2,4,5-tris(2-pyridyl)imidazole (**L1H**) molecule has been evaluated as a probe for dual sensing of Hg^{2+} and Cu^{2+} ions in EtOH/HEPES buffer medium (5 mM, pH = 7.34, 1:1, *v*/*v*). Probe **L1H** shows a good sensitive and selective *turn off* response in the presence of both Hg^{2+} and Cu^{2+} ions, which is comprehensible under long UV light. The probe can detect Cu^{2+} ion in the pH range 3–11 and Hg^{2+} ion in pH 6–8. The limit of detection for Cu^{2+} (0.77 μM) is well under the allowable limit prescribed by the United States Environmental Protection Agency. Two metal (Cu^{2+}/Hg^{2+}) ions are needed per **L1H** for complete fluorescence quenching. The probe shows marked reversibility on treatment with Na_2EDTA, making the protocol more economical for practical purposes. Paper strip coated with the **L1H** solution of EtOH can detect the presence of Cu^{2+} and Hg^{2+} ions in the sample using visible quenching of the fluorescence intensity. Density functional theory–time-dependent density functional theory (DFT–TDDFT) calculations support experimental observations, and *d*-orbitals of Cu^{2+}/Hg^{2+} provide a nonradiative decay pathway. Cell imaging study using HDF and MDA-MB-231 cells also supported the viability of **L1H** in detecting Cu^{2+} and Hg^{2+} ions in living cells.

* This work has been published in:

A. Bhattacharya, S. Mahata, A. Bandyopadhyay, B. B. Mandal and V. Manivannan, *Luminescence*, **2022**, 37, 883–891.

2.1 Introduction:

The development and utilization of heterocyclic molecules to detect metal ions are of interest for many researchers. Harmful levels of metal ions are studied for both qualitative and quantitative evaluations. Among all other methods for sensing, colorimetric and fluorometric methods are well adopted by researchers due to their cost–effectiveness. Excessive accumulation of copper and mercury ions causes severe health-related issues in living beings. Copper is crucial for functioning many biological systems, including cytochrome c oxidase, superoxide dismutase, and tyrosinase.[1] Menkes' syndrome is the result of copper deficiency, while Wilson's disease is due to copper overload.[2] Wilson's disease is an autosomal disorder that leads to inefficient copper excretion, resulting in copper deposition in the liver and kidney.[3,4] Other health hazards related to copper overloading in infants and children under six years of age are Indian childhood cirrhosis, endemic Tyrolean infantile cirrhosis, and idiopathic copper toxicosis.[3,5–7] Mercury poisoning is mainly the result of industrial discharge to natural water bodies. Metallic mercury itself is toxic and is converted into another harmful methyl-mercury species by microbial organisms residing in the water bodies.[8] Also, mercury in salt form may cause thyroid dysfunction with inhibition of secretion of T3 and T4 hormones. [9–11]

For the colorimetric and fluorometric detection of Hg^{2+} ion, a ratiometric fluorescent probe with phenanthro[9,10-*d*]imidazole and benzo[*d*]thiazole moieties was reported.[12] A probe containing anthracene and thiourea groups was found to be capable of colorimetric detection of F^- and Cu^{2+} ions, as well as Hg^{2+} ion and picric acid, fluorometrically.[13] A thiourea-based sensor bearing a pyrene ring as a chromophore has been reported to detect both Cu^{2+} and Hg^{2+} ions fluorometrically as well as by the naked eye.[14] The probe with rhodamine as chromophore has been developed as a dual sensor for Cu^{2+} and Hg^{2+} ions.[15] Another rhodamine-based chemosensor has been utilized for detecting only Hg^{2+} ion in water and both Cu^{2+} and Hg^{2+} ions in acetonitrile.[16] A three-in-one sensing strategy was developed using a 3,4-ethylenedioxythiophene- and tetrahydrophenazine-based donor–acceptor–donor type conjugated molecule as the probe for the detection of Hg^{2+} ion selectively using fluorometric, colorimetric, and paper strip.[17] Four xanthene– fluorene-based probes have been reported for the detection of Hg^{2+} ion.[18] A '*turn on*' fluorescent sensor has been reported for selective detection of Hg^{2+} ion in an aqueous medium, using a fluorescein based probe.[19] An imidazo[1,2-*a*]pyridine nucleus bearing a coumarin moiety was developed as the selective ratiometric sensor for the detection of Cu^{2+} ion.[20] Another imidazo[1,2-*a*] pyridine-based

chemosensor was developed that acts as a remarkable sensor for Zn^{2+} ion.[21] A hydrazide bearing imidazo[2,1-*b*]thiazole nucleus has been utilized for developing an Al^{3+} ion chemosensor.[22] Two structural isomers of disubstituted imidazo[1,5-*a*]pyridinium ion fluorophore bearing *p*-methoxyphenyl and *p*-diethylaminophenyl groups were found to exhibit distinct fluorescence *turn on* or ratiometric response to pH change.[23] Imidazo[1,5-*a*]pyridine and imidazo[1,5-*a*]isoquinoline moieties were also been utilized for fluorescence cell imaging studies and anion detection.[24,25] Substituted imidazole molecules have found application in medicinal chemistry as enzyme inhibitors and some 2,4,5-substituted imidazoles were found to have such properties.[26–29] Metal complexes of some trisubstituted imidazoles have also been found to show antimicrobial activity.[30] Synthesis of three positional isomers of 2,4-bis(2-pyridyl)-5-(pyridyl)imidazoles using 2-cyanopyridine and 2-,3- and 4-picolylamines have been reported.[31] Molecular structures of copper(I), chromium (III) and cadmium (II) complexes of 2,4,5-tris(2-pyridyl)imidazole (**L1H**) have also been reported.[32,33] One such isomer 2,4-bis(2-pyridyl)-5-(4-pyridyl)imidazole has been found to be a sensor for the selective detection of Zn^{2+} ion.[34] In this Chapter, utility of **L1H** as a metal ion sensor was evaluated and the results are reported.

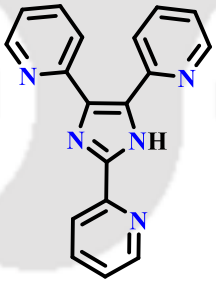

L1H

2.2 Experimental Section

2.2.1 Cell culture

Cytotoxicity evaluation and fluorescence attributes of **L1H** were carried out with human breast carcinoma cells, MDA-MB-231, procured from NCCS (India) being cultured at passage 49 and human dermal fibroblasts (hDF) procured from HiMedia Laboratories (India) being cultured at passage 22. Both the cell types were maintained and sub-cultured in high glucose Dulbecco's modified Eagle's medium (hgDMEM) procured from Gibco, USA further supplemented with 10 % (*v*/*v*) Fetal Bovine Serum (FBS) and 1% (*v*/*v*) antibiotic–antimycotic solution.

2.2.2 MTT based cytotoxicity study

Standard MTT based *in vitro* cytotoxicity investigation against the developed **L1H** was carried out on both MDA-MB-231 cells as well as hDF cells according to previously established protocol [35,36]. Briefly, both cell types were suspended in 100 µL of hgDMEM medium, post trypsin treatment, serum-based neutralization and centrifugation, and subsequently plated at a seeding density of 5×10^3 cells/well in a 96 well plate and incubated in a humidified (37 °C, 5% CO_2) incubator for 24 h. After attachment within wells, both cell types were subjected to treatment of an increasing concentration gradient of **L1H** i.e., 0, 1.25, 2.5, 5, 7.5, and 10 µM in hgDMEM for 24 h within the standard incubation conditions. Post **L1H** treatment, cellular viability was evaluated using thiazolyl blue tetrazolium bromide (MTT) reagent (Sigma Aldrich, USA). Briefly, the culture media was drawn out from the wells, and a 1:10 diluted 5 mg/mL MTT solution was prepared using phosphate buffered saline. The cells were incubated with the diluted MTT solution for 4 h. Thereafter, the purple formazan crystals formed by the incubated cells were dissolved in 100 µL DMSO and absorbance of the dissolved formazan was read at 570 nm wavelength using a Multiskan Sky Spectrophotometer (Thermo Scientific, USA). Percentage of viable cells post-exposure to **L1H** were calculated w.r.t. the positive control with no treatment of **L1H**.

2.2.3 Fluorescence imaging

The 2.5 µM non-cytotoxic concentration of **L1H** was chosen for assessing the fluorescence properties of **L1H** alone and **L1H** followed by $HgCl_2$ (Hg^{2+}) and $CuCl_2$ (Cu^{2+}) against both MDA-MB-231 and HDF cells. Both cell types were seeded at 2×10^4 cells/well in a 24-well plate and incubated in a humidified (37 °C, 5% CO_2) incubator for 24h. Post attachment, both cell types were incubated in cell culture media supplemented with 2.5 µM **L1H** dissolved in high glucose DMEM for 120 min for fluorescence appearance. Thereafter, quenching action of 5 µM $HgCl_2$ and 5 µM $CuCl_2$ were correspondingly done on the cells pre-treated with 2.5 µM **L1H** for 60 min each. The cells were washed twice with incomplete medium and replenished with complete medium before brightfield and fluorescence imaging at 20x magnification of EVOS fluorescence microscope (Life Technologies).

2.2.4 Statistical analysis

All experimental data were obtained using n = 3 samples, analyzed and represented in the form of mean ± standard deviation (SD). Statistical analyses were preformed over the experimental

groups using One-way ANOVA on OriginPro 2018 (Originlab Corporation, USA) and statistical significance was considered to be significant for *p ≤ 0.05, **p ≤ 0.01 and #p ≤ 0.001. Image processing of fluorescence micrographs was done using Fiji (ImageJ, NIH, USA).

2.3 Results and Discussion

The ligand 2,4,5-tris(2-pyridyl)imidazole (**L1H**) was reported [31] along with two other positional isomers and 2,4-bis(2-pyridyl)-5-(4-pyridyl)imidazole has been found to be selective towards Zn(II) ion [34]. Our initial evaluation of **L1H** revealed that it has an excellent fluorescent character. By virtue of having five nitrogen atoms, this ligand can coordinate with metal ions and may show selective characteristics towards a specific metal ion(s); thus, this study has been carried out.

2.3.1 UV-Vis Spectra

The UV-Visible spectrum of the free **L1H** recorded in EtOH/HEPES buffer (1:1, *v/v*) shows characteristic bands having the maxima at 268, 308, 320, 354 and 373 nm (Figure A1). Ligand **L1H** has three 2-pyridyl rings substituted at the central imidazole moiety. The ligand is rich with π electron density along with non-bonding pairs of electrons centred at N atoms. So, the possible electronic transitions are n-π^*, π-π^* and n-σ^*. Among them n-π^* transition being the lowest energy can be assigned to the pair of bands appearing at 354 and 373 nm, while the pair at 308 and 320 nm could be due to π-π^* transition.

UV-titration technique was adopted to understand the behaviour of **L1H** in the presence of various cations, wherein spectra were recorded after each gradual addition of specific cations to the solution of **L1H**. The cations used here are Li^+, Na^+, K^+, Mg^{2+}, Al^{3+}, Ca^{2+}, Cr^{3+}, Mn^{2+}, Fe^{3+}, Co^{2+}, Cu^{2+}, Zn^{2+}, Cd^{2+}, Pb^{2+} and Hg^{2+} ions. In most cases, spectral features remained unaffected but Cu^{2+} and Hg^{2+} ions showed a significant change (Figure 1). But in case of Ni^{2+} ion, the peak got flattened slightly and λ_{max} value got shifted from 308 to 311 nm, which is negligible, with respect to the shifts observed in presence of Cu^{2+} and Hg^{2+} ions. Upon adding $CuCl_2 \cdot H_2O$ to **L1H** following changes were observed: (i) a gradual decrease in peak intensity at 308 nm, (ii) 308 nm peak getting shifted to 332 nm (a red shift) accompanied by its broadening and (iii) coalescence of peaks at 354 and 373 with the new peak appearing at 332 nm. This coalescence of peaks corresponding to n-π^* transitions indicates that lone pair of electrons located on all nitrogen atoms are involved in coordination to the Cu^{2+} ion. Two clear

isosbestic points that appeared at 328 nm and 343 nm indicate that only two species are involved during the titration process (Figure 2)

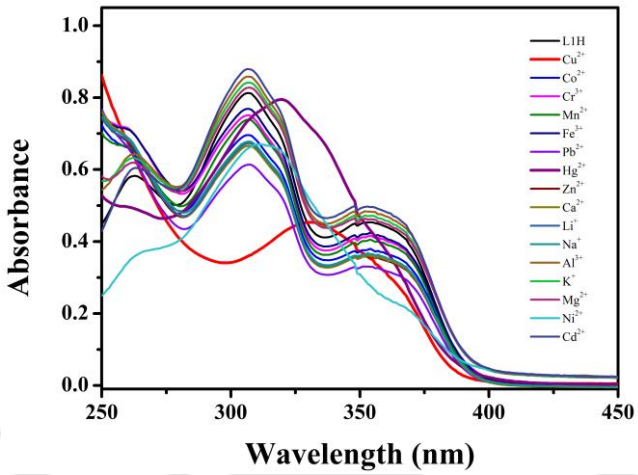

Figure 1. Absorption spectra of **L1H** (1.315×10^{-5} M) in presence of different metal ions (2.5 equivalents) in EtOH/HEPES buffer (5 mM, pH = 7.34, 1:1, *v*/*v*).

Upon adding $HgCl_2$ to **L1H**, (i) a small decrease in peak intensity at 308 nm occurred, (ii) the 308 nm peak shifted to 331 nm (a red shift) along with broadening and (iii) coalescence of peaks at 354 and 373 nm with the new peak at 331 nm. Thus, disappearance of peaks due to n-π^* transition also indicates that lone pair of electrons located on all nitrogen atoms got engaged in coordination to the Hg^{2+} ion. Two isosbestic points that appeared at 322 nm and 345 nm indicate the involvement of two species in solution (Figure A2).

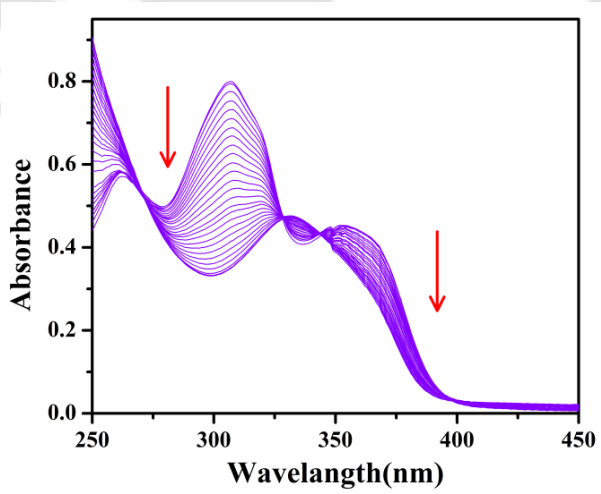

Figure 2. Changes in the absorption spectrum of **L1H** (1.315×10^{-5} M) upon gradual addition of $CuCl_2$ (upto 2.5 equivalents) in EtOH/HEPES buffer (5 mM, pH = 7.34, 1:1, *v*/*v*).

2.3.2 Emission Spectra

The molecule **L1H** is fluorescent in ethanol and its fluorescence intensity was measured using ethanol / HEPES buffer (1:1, *v/v,* pH = 7.34, rt) as a solvent in this work. Upon exciting **L1H** with a light of 308 nm wavelength, a single emission band having the maximum at 485 nm was obtained. The titration experiment was carried out by gradual addition of the metal ions (up to 2.5 equivalents) to the ligand **L1H**. Among all metal ions studied, the fluorescence intensity was completely quenched only upon addition of Hg^{2+} and Cu^{2+} ions, while metal ions like Li^{+}, Na^{+}, K^{+}, Mg^{2+}, Al^{3+}, Ca^{2+}, Cr^{3+}, Mn^{2+}, Fe^{3+}, Co^{2+}, Zn^{2+}, Cd^{2+} and Pb^{2+} ions did not exhibit any perceptible change in the emission spectra, but Ni^{2+} ion exhibited a reduction in the emission intensity. Reduction in fluorescence intensity rendered by Ni^{2+} ion (Figure 3, 4 and 5), has not much effect on the selectivity since the extent of reduction (which cannot be ascertained with naked eye) for Ni^{2+} (43%) is less than those of the Cu^{2+}(99%) and Hg^{2+}(90%) ions. From the bar diagrams (Figure A3 and A4), it can be ascertained that the selectivity towards these two ions remains intact in the presence of Ni^{2+}. To the buffered probe solution, the addition of an equimolar mixture of Cu^{2+} and Hg^{2+} ions exhibited about 50% quenching (with one equivalent of the mixture) of the fluorescence intensity and complete quenching happened with two equivalents of the mixture (Figure A3).

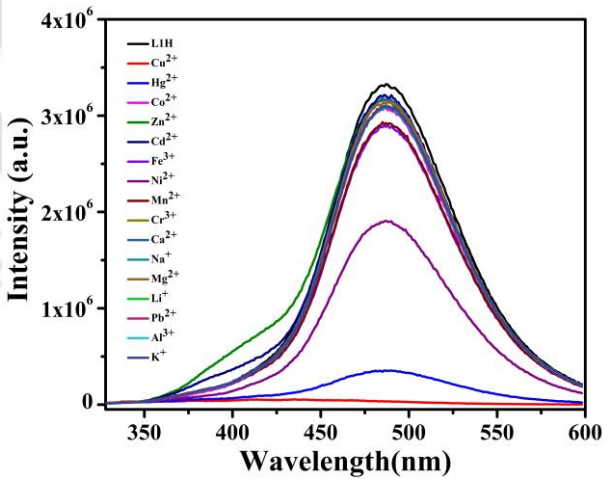

Figure 3. Emission spectra of **L1H** (1.315×10^{-5} M) in presence of different metal ions (2.5 equivalents) in EtOH/HEPES buffer (5 mM, pH = 7.34, 1:1, *v/v*)

Although it is apparent that the ligand **L1H** is very selective towards Cu^{2+} and Hg^{2+}, sometimes there can be competition between the metal ions to occupy the binding sites of the ligand. In order to affirm this, solutions of Cu^{2+} ion and Hg^{2+}ion were added to the solution containing

the probe and another metal ion, and their emission spectra were recorded. The bar diagram (Figure A4) clearly reveals that the quenching of fluorescence was an inherent property of Cu^{2+} and Hg^{2+} ions even in the presence of other metal ions. So, there can be no interference from other metal ions if they are present in the solution.

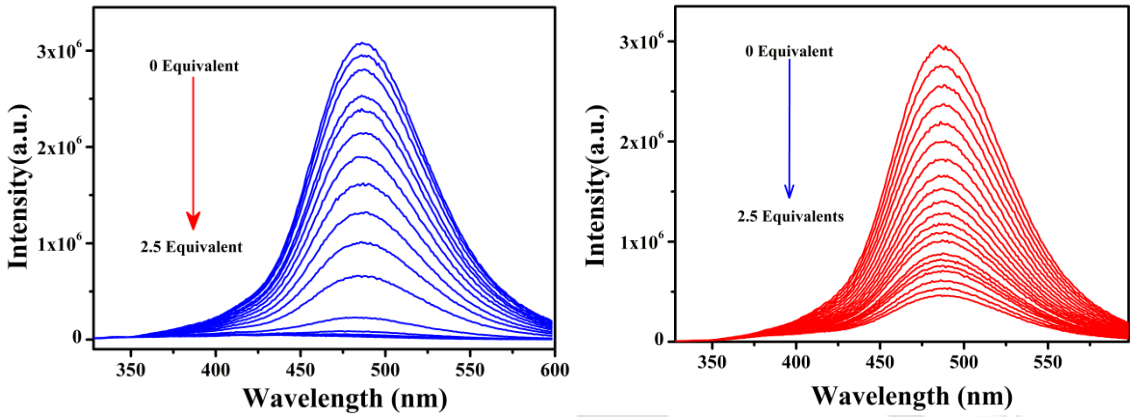

Figure 4. Fluorescence titration of **L1H** with $CuCl_2$ (left) and $HgCl_2$ (right).

The sensing of metal ions through the fluorescence quenching mechanism can be affected by pH of the solution. For ligands having N- and O- donors at binding sites tend to accept proton(s) from the solution, which makes the lone pair of electrons unavailable for complexation with metal ions, especially at lower pH values. Although the binding of proton to the donor sites depends on the pK_a value of donor sites at a given pH, there can be competition between the proton and the metal ions to bind to the probe. On the other hand, at higher pH, metal ions form hydroxide, which will decrease the number of quenchers, i.e., metal ions in the solution, which can hamper the sensing phenomenon. So, it is indispensable to establish a pH window for every sensor molecule to use for practical purposes.

In this study, it was found that these two metal ions showed a different pattern of quenching. For Cu^{2+} ion, probe **L1H** shows an admissible extent of quenching in terms of comprehensibility through a wide pH range of 3-11. But for the Hg^{2+} ion, the pH window is narrowed down to 6-8, in that range the probe can easily detect the presence of the Hg^{2+} ion. So, the presence of copper ions can be easily detected outside the pH range of 6-8 as well; wherein Hg^{2+} ions are causing fluorescence quenching (Figure A5 and A6)

Another aspect for a probe for working as a practically usable sensor is its reversibility so that the same system can be used in several cycles. This test can be achieved using a powerful sequestering agent $EDTA^{4-}$. Typically, to a mixture of the probe and 2.0 equivalents of Cu^{2+}

ion, the same equivalent of Na_2EDTA solution was added and emission spectrum was recorded. In this study, this cycle was repeated three times and it is understandable from the result (Figure A7 and A8), that the probe **L1H** retained its fluorescence when released in free form after Cu^{2+} and Hg^{2+} ions were sequestered by $EDTA^{4-}$. Presence of anions like SO_4^{2-}, SCN^-, $S_2O_3^{2-}$, NO_3^-, $C_2O_4^{2-}$, F^-, NO_2^-, AcO^- and $HCOO^-$, no change in fluorescence spectra was observed, confirming that these anions have no interference with the sensitivity of ligand (Figure A9).

2.3.3 Binding ratio

The binding ratio between the metal ion and the ligand **L1H** was determined by the method of Job's Plot. In this continuous variation method, it is observed that both two metal ions bind with one molecule of **L1H**. Thus 2:1 ratio suggests that two Cu^{2+} or two Hg^{2+} ions bind to $\mathbf{L1}^-$, the conjugate base of **L1H** (with the dissociable proton of the imidazole ring being removed) through all five N atoms (Figure A10 and A11). The values of binding constants calculated from the Benesi-Hildebrand Plot are $1.53 \times 10^4\ M^{-1}$ (Cu^{2+}) and $1.18 \times 10^4\ M^{-1}$ (Hg^{2+}) (Figure A12 and A13). High values of the binding constants indicate the formation of a stable complex between **L1H** and Cu^{2+} and Hg^{2+} ions.

The ESI(+) mass spectrum of copper complex showed a peak at *m*/*z* value of 597.89 (Figure A14) corresponding to the formula $[Cu_2(\mathbf{L1})Cl_3(C_2H_5OH)Na]^+$ (*m*/*z* value calculated for $[Cu_2(C_{18}H_{12}N_5)Cl_3(C_2H_5OH)Na]$ is 597.91). The peak at *m*/*z* = 802.24 observed in the ESI(+) mass spectrum of the mercury complex can be fitted to the composition $[Hg_2(\mathbf{L1})Cl_2(CH_3OH)]^+$ (*m*/*z* value calculated for $[Hg_2(C_{18}H_{12}N_5)Cl_2(CH_3OH)]^+$ is 802.01) (Figure A15). Thus, one ligand capturing two metal bivalent metal ions can be arrived at from these mass spectral data and in other words, a binding stoichiometry of 2:1 between metal and **L1H** is pertinent for both copper and mercury complexes. The same ratio has also been found in the case of zinc [34] with 2,4-bis(2-pyridyl)-5-(2-pyridyl)imidazole, the positional isomer of **L1H**.

The absolute fluorescence quantum yield was calculated from Petite Integrating Sphere Method and for **L1H,** it has been determined to be 0.42. After adding Cu^{2+} and Hg^{2+} ions to the solution of **L1H,** the quantum yield has dropped to 0.034 and 0.053, respectively. The limit of detection was calculated for both the metal ions and it was found to be 0.77 µM (for Cu^{2+}) and 1.58 µM (for Hg^{2+}) (Figure A16 and A17). The allowable limit of copper in drinking water is 20 µM [37], so **L1H** can be a valuable probe for the detection of Cu^{2+} ion. According to the US EPA

guidelines [38] and FSSAI (Food Safety and Standards Authority of India), the allowable limit of mercury in drinking water should be less than 0.00997 μM and 0.00498 μM, respectively. So, **L1H** is a poor choice for the detection of Hg^{2+} ion in drinking water but in fish and other food items, the allowable limit is in the range of 2.49-4.98 μM; this probe can be of use.

In terms of LOD, probe **L1H** works better than the previously reported probes (Table A6) **4** and **5** and comparable with **2**. Other imidazole-based probes **8**, **9** and **11** were reported to be sensing Zn^{2+}, Al^{3+} and sulphite ions, respectively, while **10** acted as a very good pH sensor. Probes **1**–**7** were reported to detect Cu^{2+} and/or Hg^{2+} by single or dual mode of sensing.

2.3.4 Detection in real water samples

To check probe **L1H**'s practical applicability**,** we did similar titration experiments on tap water and river water (taken from the Brahmaputra River near the IIT Guwahati campus). At first, the water samples were filtered through a 0.22 μm membrane filter. After that, a 1:1 mixture of EtOH and the water samples were used to prepare test solutions of probe and metal ions. After recording the background spectrum, analytes were added for recording emission titration profiles with Cu^{2+} and Hg^{2+} ions. Quenching of fluorescence activity of **L1H** by Cu^{2+} and Hg^{2+} ions were identical with the pure water samples (Figure A18 and A19)

2.3.5 Life-time measurement

Stern-Volmer plot has been the well-known procedure wherein the ratio of initial fluorescence intensity and the fluorescence intensity (I_0/I) after addition of the quencher is plotted against the concentration of the quencher (Figure A20) [39,40]. For both Cu^{2+} and Hg^{2+} ions, hyperbolic plots were obtained, consistent with the quenching nature of their action. From TRPL lifetime measurement (Figure 6), the average fluorescence lifetime was calculated to be 2.115 (for **L1H**), 2.101 (for **L1H** + $CuCl_2$) and 2.157 ns (for **L1H** + $HgCl_2$). Very similar average lifetime values indicate the static nature of quenching and the presence of efficient non-radiative decay for the excited state.

2.3.6 ^{1}H NMR Spectra

During ^{1}H NMR titration of **L1H** in DMSO-d_6 with $CuCl_2$ solution, the peak (Figure 7) at δ = 12.63 ppm corresponding to imidazole N–H proton broadened gradually, which finally disappeared after addition of two equivalents of Cu^{2+} ion. This indicates the binding of **L1H** as $\mathbf{L1}^-$ to Cu^{2+} ions. In addition, peaks in the aromatic region broadened accompanied by merging

of adjacent peaks during the course of the titration which is due to paramagnetic nature of Cu^{2+} ions. But during ^{1}H NMR titration of **L1H** with $HgCl_2$ (Figure A21) and broadening of only the N–H proton was observed which disappeared eventually and peaks in the aromatic region remained sharp.

2.3.7 Paper-based sensing

The practical applicability of a sensor should be attributed to the ease of its use and for this purpose, rectangular pieces of filter paper were dipped in ethanolic solution of **L1H** and dried in air. This dried paper containing sensor was dipped in solutions of Cu^{2+} and Hg^{2+} ions (2×10^{-6} M, deionised water) separately and were observed under long UV light in UV chamber. The paper part that has come into contact with Cu^{2+} and Hg^{2+} ions exhibited a vastly diminished fluorescence (Figure A23). Figure 8 shows the comparison of fluorescence property of the sensor paper strips before and after dipping in metal ion solutions. This experiment clearly established the practical applicability of the fluorescent sensor **L1H** in the real sample by a cheap method that requires only paper strips and a long UV lamp.

Figure 5. Photograph of the solutions of **L1H** in presence of various metal ions under long UV (365 nm) and blank **L1H** solution in the cuvette.

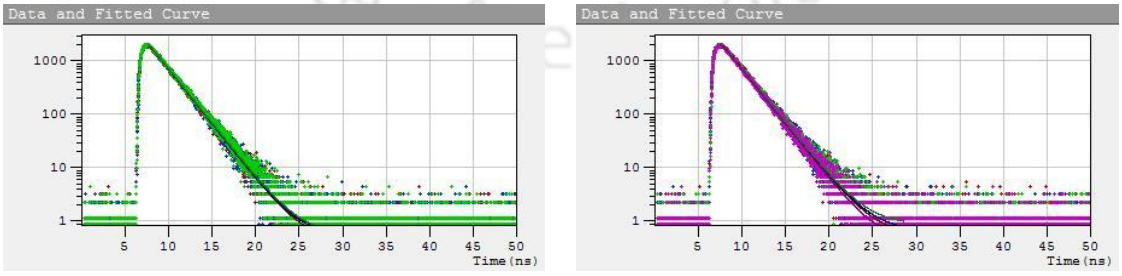

Figure 6. Fluorescence decay profile of **L1H** in presnce of Cu^{2+} (left) and Hg^{2+} (right) ions.

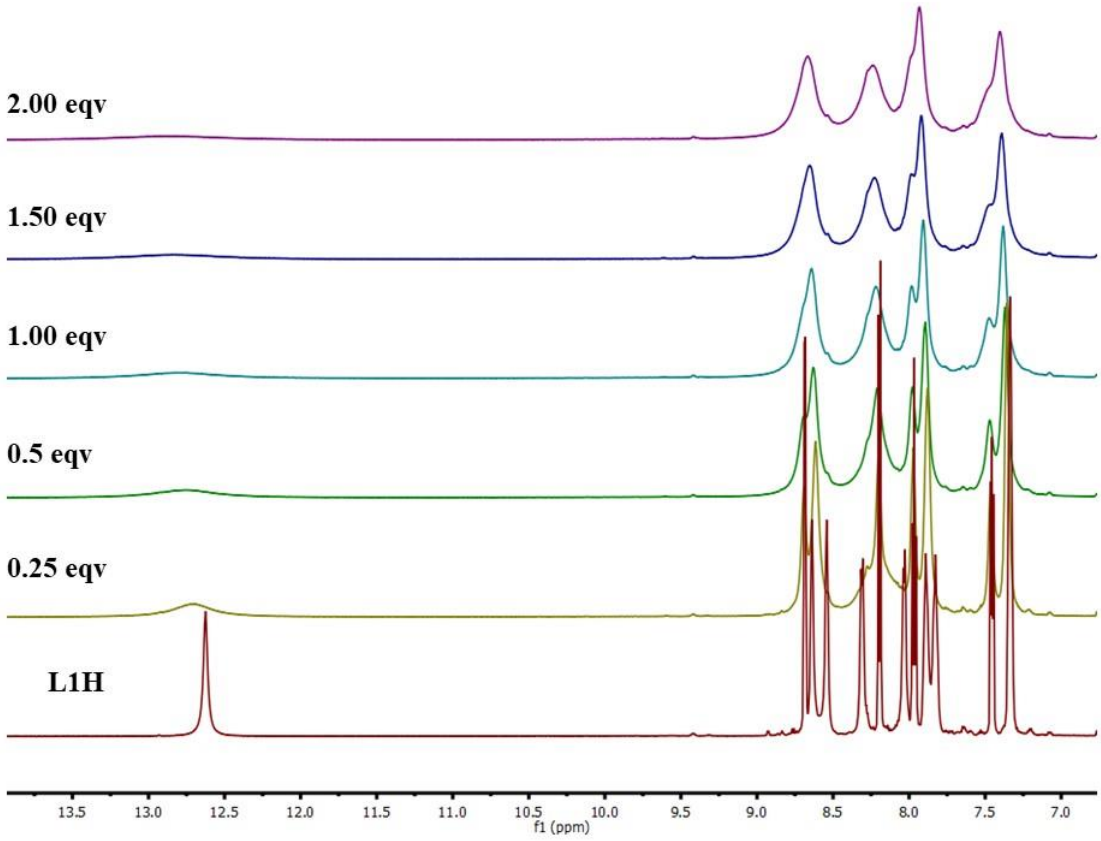

Figure 7. ^{1}H NMR titration of **L1H** with $CuCl_2$.

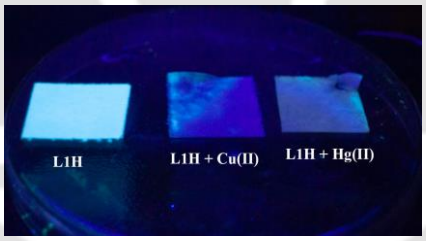

Figure 8. Paper strip images under long UV.

2.3.8 Proposed sensing mechanism

The probe **L1H** has three pyridine rings attached to a central imidazole ring and the whole molecule is non-planar due to the non-zero dihedral angle between 2-pyridyl rings with respect to the central imidazole ring. It has also been found that **L1H** binds in its deprotonated form (**L1**$^{-}$). Each of the five nitrogen atoms has one lone pair of electrons, binding two metal ions simultaneously. As a result, on one side **L1**$^{-}$ can be acting as a tridentate ligand and on the other side as a bidentate ligand. Thus, all the lone-pair of the electrons are engaged in coordination to the metal center (Figure 9). The TRPL experiment shows that the static nature of quenching

is happening, so it is classic example of Chelation induced Quenching (CHEQ) mechanism operating in the presence of Cu^{2+} and Hg^{2+} ions.

2.3.9 Theoretical calculations

The DFT / TDDFT calculation (6-31G/LanL2DZ) were performed on the molecular formula $[Cu_2(\mathbf{L1})Cl_3(EtOH)]$ (**1**) and $[Hg_2(\mathbf{L1})Cl_3]$ (**2**) along with **L1H**. Details of such calculations on **L1H** has been reported elsewhere by another group [40] but we have included its calculation results here for uniformity in comparison with complexes. In complex **1**, the ligand π and π* orbitals are found to be HOMO–4 and LUMO+1, respectively (Figure 10). In between these ligand-based MOs, *d*-orbitals of copper are located as LUMO, HOMO, HOMO-1, HOMO-2 and HOMO-3. These orbitals probably provide efficient non-radiative decay through metal-ligand vibrations and from the differences of energy of different MO levels the transition from the HOMO–4 to LUMO+1 level seems to be best suited with the experimental observations in the electronic spectrum of **1**.

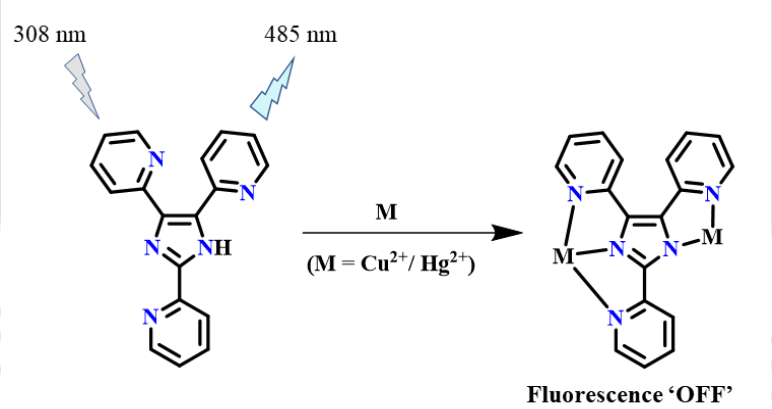

Figure 9. Proposed mechanism of sensing.

Also, in complex **2**, the ligand π and π* orbitals are found to be HOMO–2 and LUMO, respectively. In between these ligand-based MOs, *d*-orbitals of mercury are present as HOMO and HOMO-1 (along with lone pair of electrons from Cl) are located, providing non-radiative decay through metal-ligand vibrational states. In complex **2,** experimentally observed absorption bands are probably due to the HOMO–2 to LUMO transition. In both complexes, the LUMO and LUMO+1 levels of the ligand were stabilized on coordination. The HOMO–4 of **1** and HOMO–2 of **2** were also stabilized when compared to the HOMO of **L1H** but the

HOMO-LUMO energy difference in of **1** and **2** was higher than that in **L1H**, consistent with the red shift observed in the complexes.

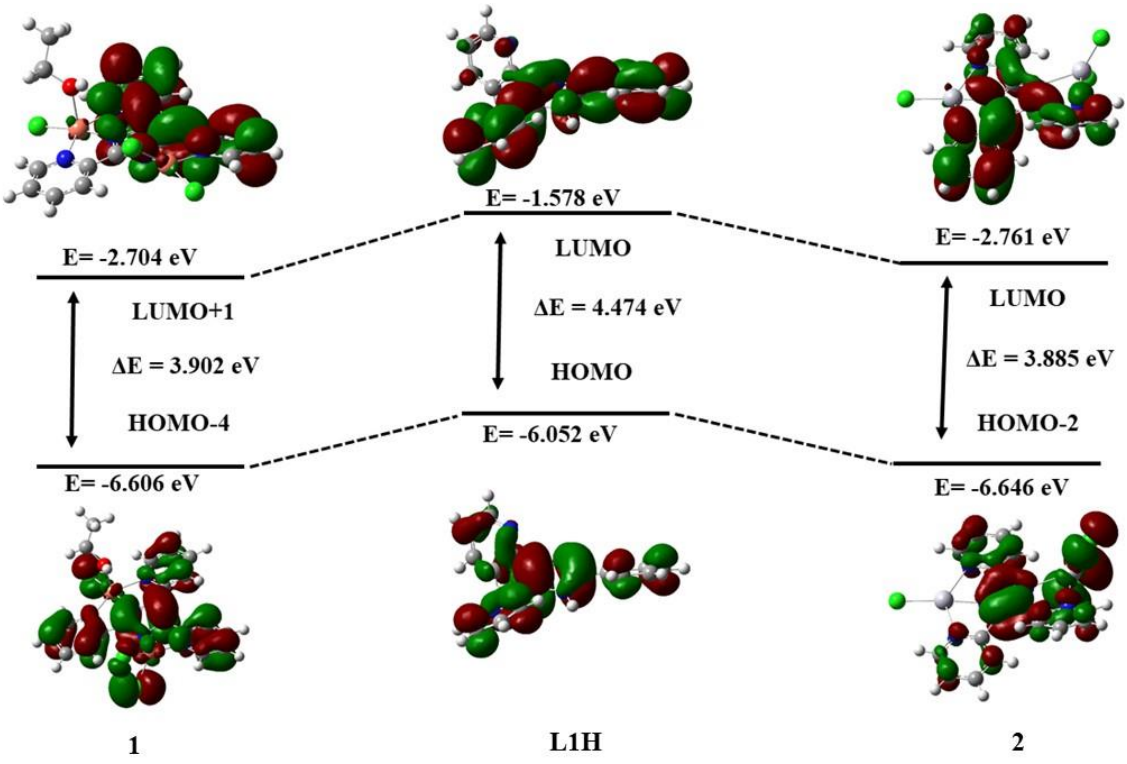

Figure 10. Relevant ligand based frontier orbitals present in **1**, **L1H** and **2**.

2.3.10 Cytotoxicity study

MTT based cytotoxicity assay revealed that as the **L1H** concentration was raised in the culture medium, the viability of the incubated HDF and MDA-MB-231 cells decreased (Figure 11). The viability of both HDF and MDA-MB-231 was found to decrease significantly at **L1H** concentration of 5 μM and above when compared to the untreated cells. The viability of HDF cells were found to reduce significantly ($p<0.001$) to 68.69±6.89%, 67.77±3.8% and 53.53±3.49% at 5 μM, 7.5 μM and 10 μM of **L1H** concentration respectively when compared with the positive control. Similarly, the viable population of MDA-MB-231 cells decreased significantly to 85.29±3.11%, 65.59±5.55% and 57.95±6.52% at 5 μM ($p<0.05$), 7.5 μM ($p<0.001$) and 10 μM ($p<0.001$) of **L1H** concentration respectively when compared with the positive control. Though the viability of MDA-MB-231 was higher than that of HDF cells at 5 μM **L1H** concentration, the decrease of viability was significant as compared to the control

and hence the 2.5 μM concentration of **L1H** was chosen for fluorescence and bright field imaging.

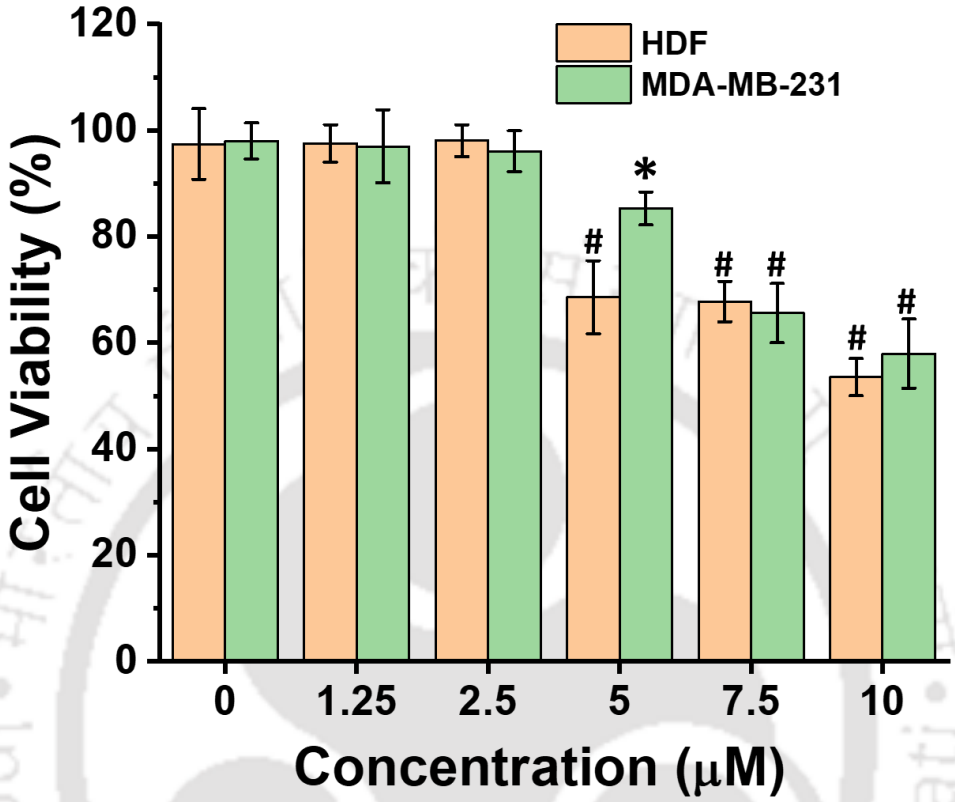

Figure 11. MTT based evaluation of cellular viability of HDF and MDA-MB-231 cells treated using varying concentrations of **L1H** in media. *p≤0.05 and #p≤0.001

2.3.11 Fluorescence imaging

Fluorescence of the **L1H** internalized by the cells and its quenching when co-incubated with bivalent metal ions (Hg^{2+} from $HgCl_2$ and Cu^{2+} from $CuCl_2$) was evaluated after incubation for specified time intervals in both MDA-MD-231 (Figure 12) and HDF cells (Figure 13). Both HDF and MDA-MB-231 and HDF cells exhibited no fluorescence intensity when incubated with bare media and started showing fluorescence after incubation with 2.5 μM of **L1H**. Thereafter, to comprehend the quenching property of bivalent metal ions, cells were treated with 5 μM of $HgCl_2$ and $CuCl_2$ individually after the incubation with **L1H**. Bright blue fluorescence was observed when the cells were incubated only with **L1H** as can be seen in the blue filter and the merged brightfield images. Fluorescence quenching can be seen in the blue filter and merged brightfield images post-metal ion treatment in both the cell types. This could serve as a detection modality for such divalent heavy metal ions within the cells.

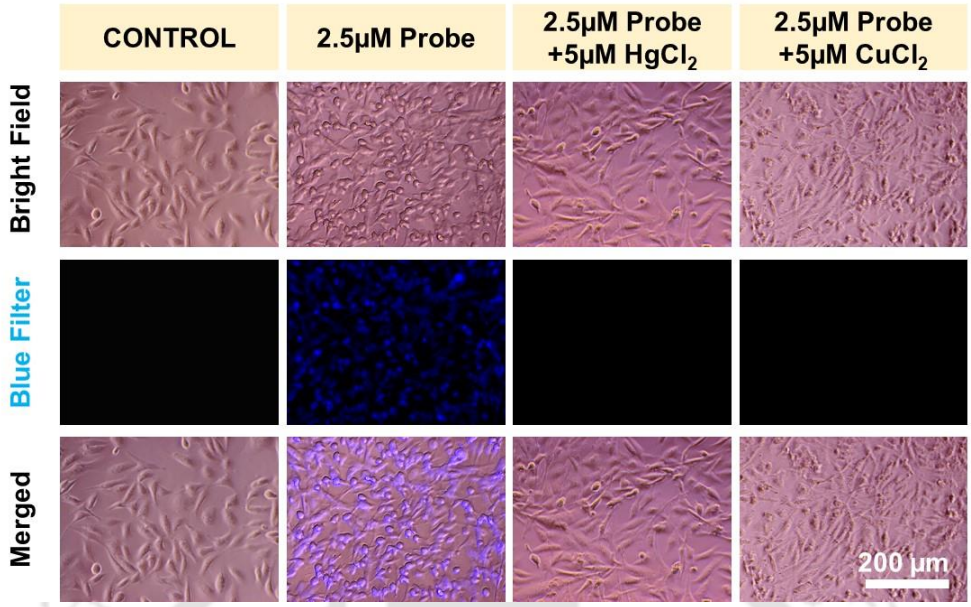

Figure 12. Brightfield, fluorescence and merged microscopic images of live MDA-MB-231 cells when incubated with 2.5 μM **L1H** and its subsequent quenching after the addition of 5 μM $HgCl_2$ and $CuCl_2$. Scale bar: 200μm

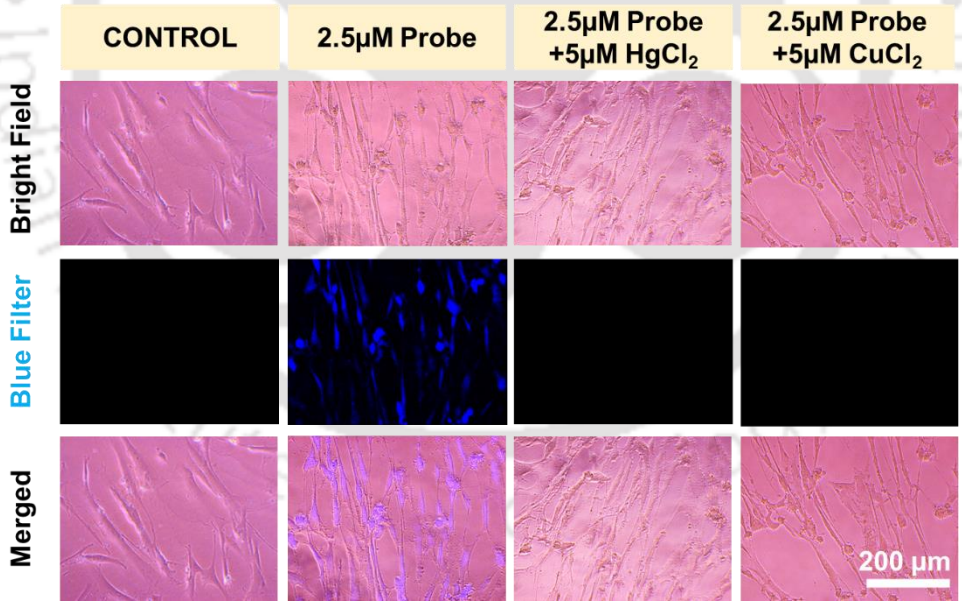

Figure 13. Brightfield, fluorescence and merged microscopic images of live HDF cells when incubated with 2.5 μM **L1H** and its subsequent quenching after the addition of 5 μM $HgCl_2$ and $CuCl_2$. Scale bar: 200μm

2.4 Conclusion

The probe **L1H** has been evaluated as a metal ion sensor by various spectrophotometric methods. Its conjugate base $\mathbf{L1^-}$, by virtue of having five nitrogen donor sites, acts as a di-bridging ligand, simultaneously coordinating in tridentate and bidentate fashions. This probe is rare with its ability to detect copper and mercury selectively. The LOD value towards Cu^{2+} and Hg^{2+} ions are 0.77 and 1.58 μM, respectively and the binding stoichiometry per **L1H** were found to be 2 for both metal ions. The large binding constant value indicate the formation of a stable complex between **L1H** and Cu^{2+} / Hg^{2+} ions. The pH window of the probe towards Cu^{2+} ion is large (3–11) and since the selectivity of the probe depends on pH of the test solution, it can be copper-selective beyond the pH range of 6-8 wherein the pH window of Hg^{2+} ion exists. The probe **L1H** is reusable for several cycles and filter papers adsorbed with **L1H** can be adopted for ready usability. TDDFT calculations indicate the presence of metal *d*-orbitals in between the ligand π and π^* orbitals facilitating efficient fluorescence quenching. Fluorescence imaging study in live cells (MDA-MB-231 and HDF) also showed similar behavior on *in-vitro* incubation with the probe and probe plus analyte. The quenching of fluorescence happens inside cells, confirming that sensing is possible inside cells with the **L1H**.

References

[1] P. Verwilst, K. Sunwoo, J. S. Kim, *Chem. Commun.* **2015**, *51*, 5556–5571.

[2] M. C. Linder, M. Hazegh-Azam, *Am. J. Clin. Nutr.* **1996**, *63*, 797S-811S.

[3] I. H. Scheinberg, I. Sternlieb, *Am. J. Clin. Nutr.* **1996**, *63*, 842S-845S.

[4] V. A. Coronado, J. A. Bonneville, H. Nazer, E. A. Roberts, D. W. Cox, *Clin. Genet.* **2005**, *68*, 548–551.

[5] M. S. Tanner, *Am. J. Clin. Nutr.* **1998**, *67*, 1074S-1081S.

[6] T. Müller, H. Feichtinger, H. Berger, W. Müller, *Lancet* **1996**, *347*, 877–880.

[7] R. Mehta, D. M. Templeton, P. J. O'Brien, *Chem. Biol. Interact.* **2006**, *163*, 77–85.

[8] P. Li, X. B. Feng, G. L. Qiu, L. H. Shang, Z. G. Li, *J. Hazard. Mater.* **2009**, *168*, 591–601.

[9] R. A. Bernhoft, *J. Environ. Public Health* **2012**, *2012*, 1-10.

[10] B. Fernandes Azevedo, L. Barros Furieri, F. M. I. Peçanha, G. A. Wiggers, P. Frizera Vassallo, M. Ronacher Simões, J. Fiorim, P. Rossi De Batista, M. Fioresi, L. Rossoni, I. Stefanon, M. J. Alonso, M. Salaices, D. Valentim Vassallo, *J. Biomed. Biotechnol.* **2012**, *2012*, 1-11.

[11] K. M. Rice, E. M. Walker Jr, M. Wu, C. Gillette, E. R. Blough, *J. Prev. Med. Public Health* **2014**, *47*, 74–83.

[12] Q. Gao, Y. Jiao, C. He, C. Duan, *Mol.* **2019**, *24*, 2268.

[13] D. Udhayakumari, S. Velmathi, P. Venkatesan, S.-P. Wu, *J. Lumin.* **2015**, *161*, 411–416.

[14] W.-C. Lin, C.-Y. Wu, Z.-H. Liu, C.-Y. Lin, Y.-P. Yen, *Talanta* **2010**, *81*, 1209–1215.

[15] K. Wang, Q. Kong, X. Chen, J. Yoon, K. M. K. Swamy, F. Wang, *Chinese Chem. Lett.* **2020**, *31*, 1087–1090.

[16] S. Bayindir, *J. Photochem. Photobiol. A Chem.* **2019**, *372*, 235–244.

[17] E. G. C. Ergun, *New J. Chem.* **2021**, *45*, 4202–4209.

[18] G. Zhao, Y. Sun, H. Duan, *New J. Chem.* **2021**, *45*, 685–695.

[19] E. M. Nolan, S. J. Lippard, *J. Am. Chem. Soc.* **2003**, *125*, 14270–14271.

[20] Shaily, A. Kumar, N. Ahmed, *Supramol. Chem.* **2017**, *29*, 146–152.

[21] S. Xiao, Z. Liu, J. Zhao, M. Pei, G. Zhang, W. He, *RSC Adv.* **2016**, *6*, 27119–27125.

[22] H. Wang, X. Xu, J. Yin, Z. Zhang, L. Xue, *ChemistrySelect* **2021**, *6*, 6454–6459.

[23] J. T. Hutt, J. Jo, A. Olasz, C.-H. Chen, D. Lee, Z. D. Aron, *Org. Lett.* **2012**, *14*, 3162–3165.

[24] G. Volpi, B. Lace, C. Garino, E. Priola, E. Artuso, P. Cerreia Vioglio, C. Barolo, A. Fin, A. Genre, C. Prandi, *Dye. Pigment.* **2018**, *157*, 298–304.

[25] Q. Yuan, L.-L. Chen, X.-H. Zhu, Z.-H. Yuan, Y.-T. Duan, Y.-S. Yang, B.-Z. Wang, X.-M. Wang, H.-L. Zhu, *Talanta* **2020**, *217*, 121087.

[26] D. Niculescu-Duvaz, I. Niculescu-Duvaz, B. M. J. M. Suijkerbuijk, D. Ménard, A. Zambon, L. Davies, J.-F. Pons, S. Whittaker, R. Marais, C. J. Springer, *Bioorg. Med.*

Chem. **2013**, *21*, 1284–1304.

[27] I. M. Buck, J. W. Black, T. Cooke, D. J. Dunstone, J. D. Gaffen, E. P. Griffin, E. A. Harper, R. A. D. Hull, S. B. Kalindjian, E. J. Lilley, I. D. Linney, C. M. R. Low, I. M. McDonald, M. J. Pether, S. P. Roberts, N. P. Shankley, M. E. Shaxted, K. I. M. Steel, D. A. Sykes, M. J. Tozer, G. F. Watt, M. K. Walker, L. Wright, P. T. Wright, *J. Med. Chem.* **2005**, *48*, 6803–6812.

[28] M. Juchum, M. Günther, E. Döring, A. Sievers-Engler, M. Lämmerhofer, S. Laufer, *J. Med. Chem.* **2017**, *60*, 4636–4656.

[29] M. Yar, M. Bajda, S. Shahzad, N. Ullah, M. A. Gilani, M. Ashraf, A. Rauf, A. Shaukat, *Bioorg. Chem.* **2015**, *58*, 65–71.

[30] M. Ismael, A. Abdou, A.-M. Abdel-Mawgoud, *Zeitschrift für Anorg. und Allg. Chemie* **2018**, *644*, 1203–1214.

[31] V. K. Fulwa, R. Sahu, H. S. Jena, V. Manivannan, *Tetrahedron Lett.* **2009**, *50*, 6264–6267.

[32] Y.-J. Ou, Y.-J. Ding, Q. Wei, X.-J. Hong, Z.-P. Zheng, Y.-H. Long, Y.-P. Cai, X.-D. Yao, *RSC Adv.* **2015**, *5*, 27743–27751.

[33] Y. Qin, Y. Chen, J. Liu, J. Zhao, D. Gao, Y. Li, W. Liu, W. Li, *Inorg. Chem. Commun.* **2015**, *56*, 58–61.

[34] N. Behera, V. Manivannan, *ChemistrySelect* **2016**, *1*, 4016–4023.

[35] S. Mahata, G. Janani, B.B. Mandal, V. Manivannan, *J. Photochem. Photobiol. A Chem*. **2021**, *417*, 113340.

[36] S. Mahata, A. Bhattacharya, J.P. Kumar, B.B. Mandal, V. Manivannan, J. *Photochem. Photobiol. A Chem.* **2020**, *394*, 112441.

[37] D. J. Fitzgerald, *Am. J. Clin. Nutr.* **1998**, *67*, 1098S-1102S.

[38] S. Martin, W. Griswold, Environmental Science and Technology Briefs for Citizens Human Health Effects of Heavy Metals, **2009**

[39] L. K. Fraiji, D. M. Hayes, T. C. Werner, *J. Chem. Educ.* **1992**, *69*, 424.

[40] J.R. Lakowicz, Quenching of Fluorescence. In: J.R. Lakowicz (Eds) Principles of Fluorescence Spectroscopy. Springer, Boston, MA, **2006**, 278-327

[41] A. Báez-Castro, J. Baldenebro-López, D. Glossman-Mitnik, H. Höpfl, A. Cruz-Enríquez, V. Miranda-Soto, M. Parra-Hake, J.J. Campos-Gaxiola, *J. Mol. Struct*. **2015**,*1099*, 126–134.

Appendix

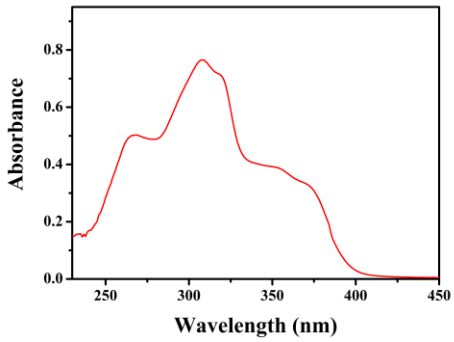

Figure A1. UV-Vis spectrum of **L1H** in 1:1 EtOH/HEPES buffer solution

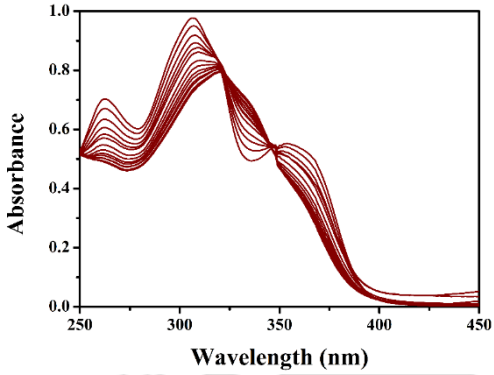

Figure A2. UV titration plot for **L1H** with Hg^{2+} ion.

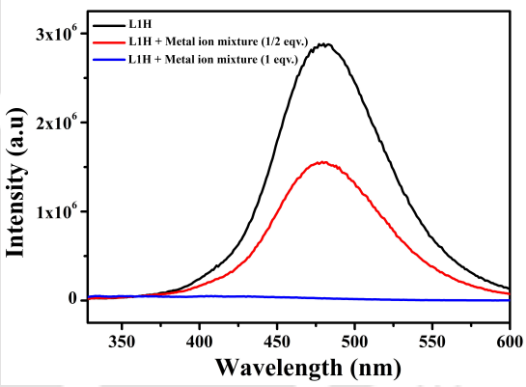

Figure A3. Fluorescence response of **L1H** towards mixture of Cu^{2+} and Hg^{2+} ions.

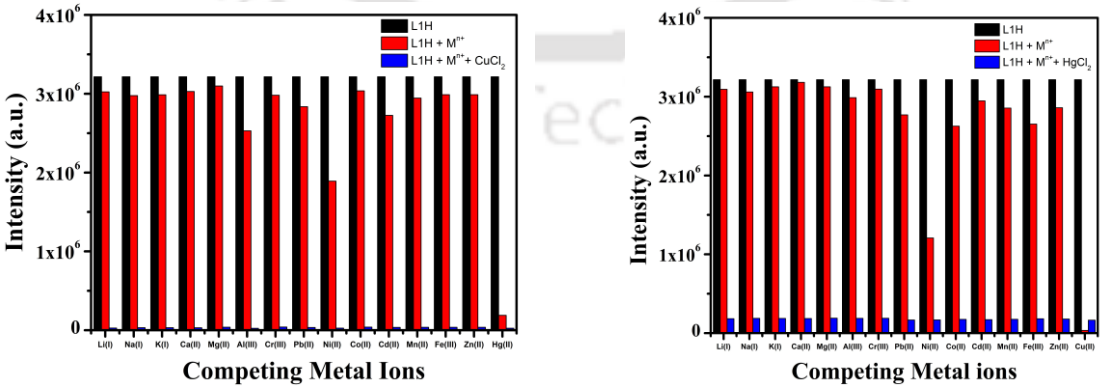

Figure A4. Fluorescence response of **L1H** towards Cu^{2+} ion (left) and Hg^{2+} ion (right) over other metal ions.

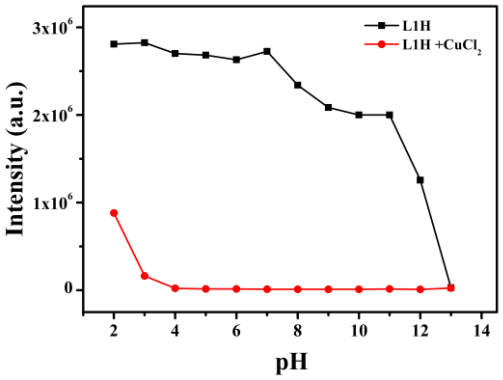

Figure A5. Effect of pH on the fluorescence sensing of $CuCl_2$

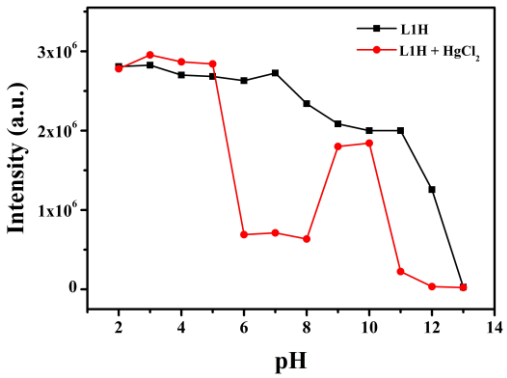

Figure A6. Effect of pH on the fluorescence sensing of $HgCl_2$.

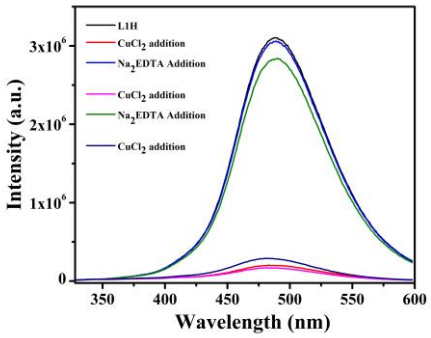

Figure A7. Reversibility test for Cu^{2+} ion

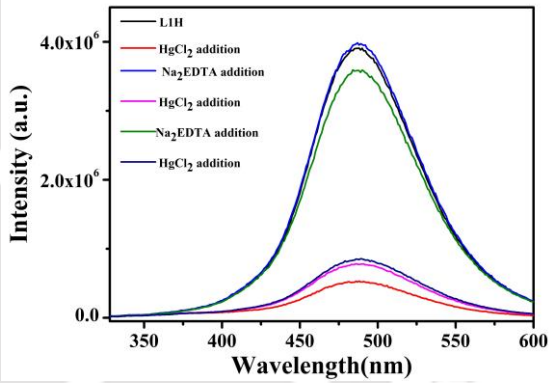

Figure A8. Reversibility test for Hg^{2+} ion.

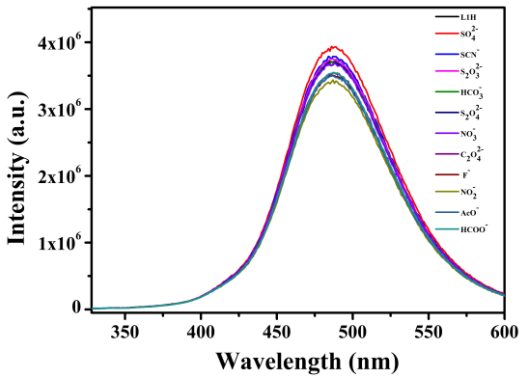

Figure A9: Effect of counter anions.

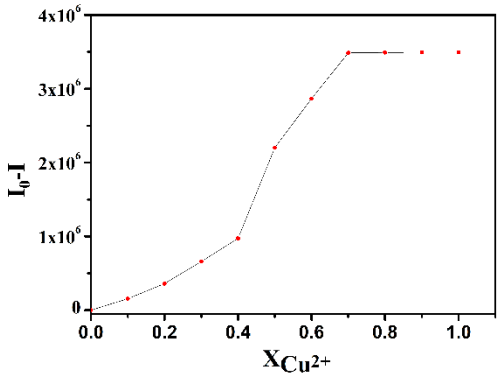

Figure A10. Job's Plot for **L1H** – Cu^{2+} complex

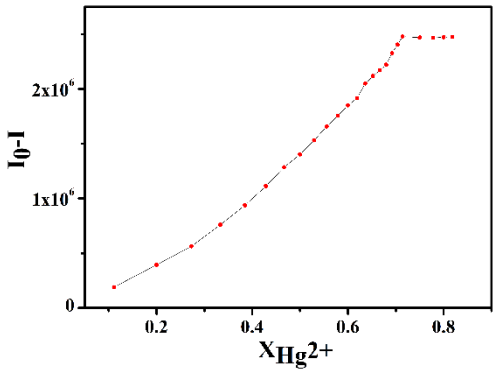

Figure A11. Job's Plot for **L1H** – Hg^{2+} complex

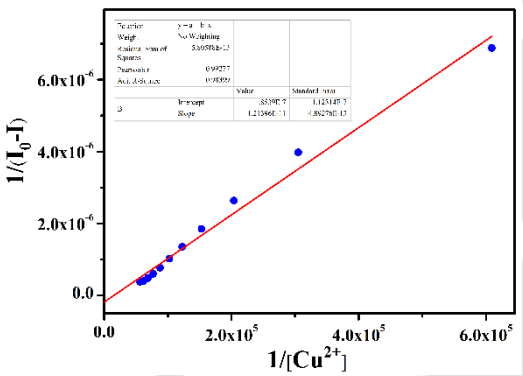

Figure A12. Benesi-Hildebrand plot for Cu^{2+} ion.

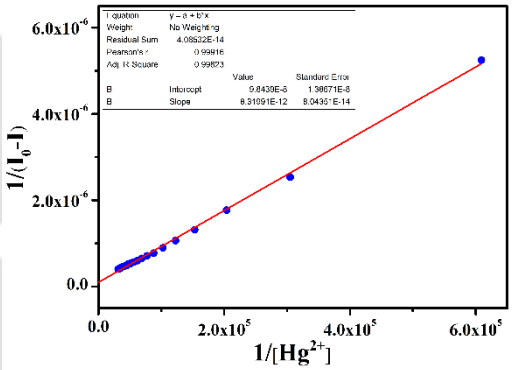

Figure A13. Benesi-Hildebrand plot for Hg^{2+} ion

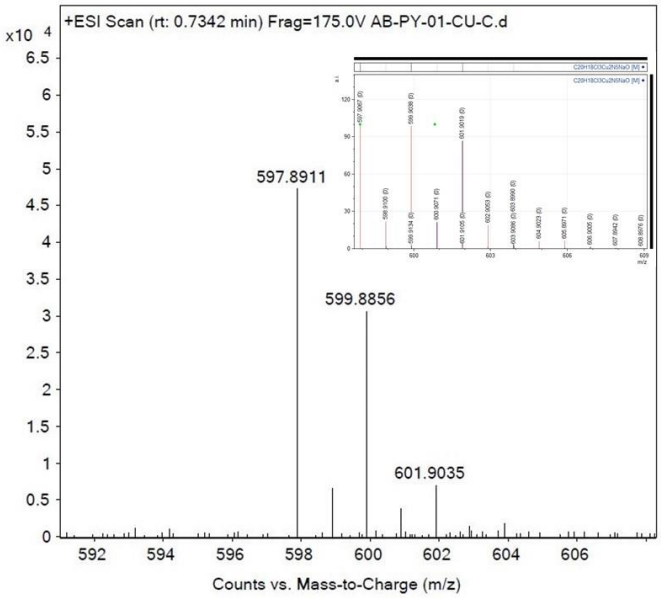

Figure A14. ESI (+) Mass spectrum and calculated spectrum (in-set) of **1**.

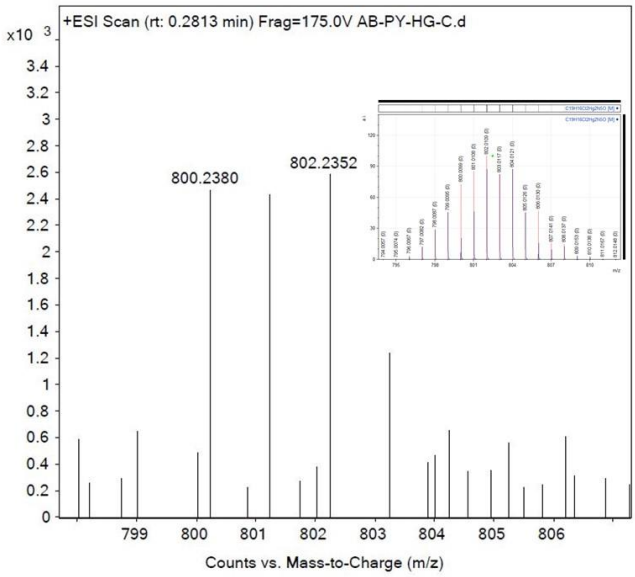

Figure A15: ESI (+) Mass spectrum and calculated spectrum (in-set) of **2**.

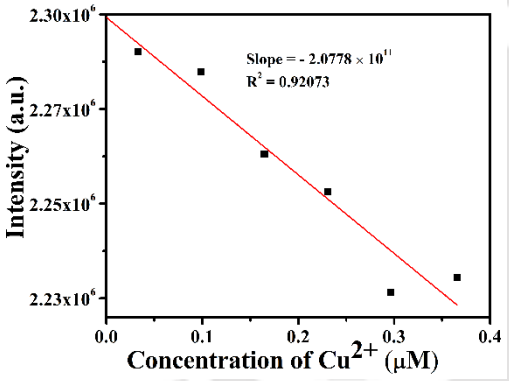

Figure A16. Calibration for the limit of detection for Cu^{2+} ion.

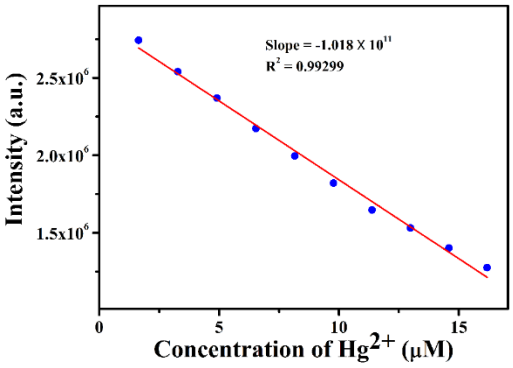

Figure A17. Calibration for the limit of detection for Hg^{2+} ion.

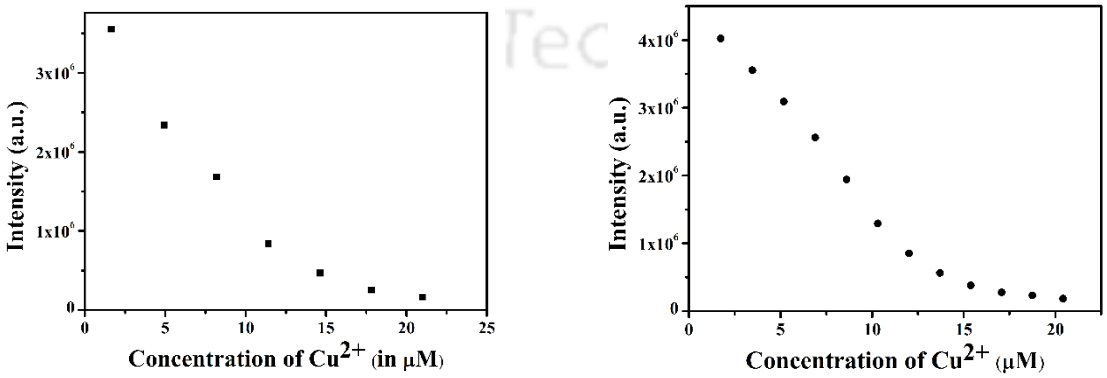

Figure A18. Titration of **L1H** with Cu^{2+} ion in tap water (left) and river water (right).

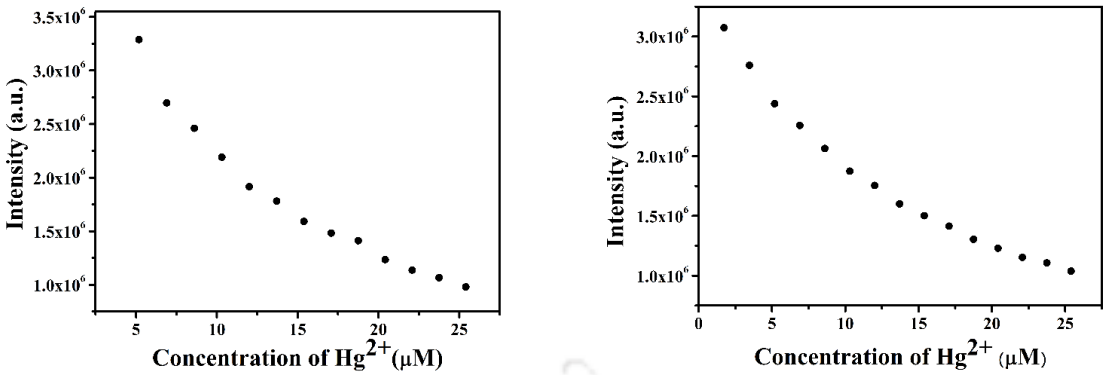

Figure A19. Titration of **L1H** with Hg^{2+} ion in tap water (left) and river water (right).

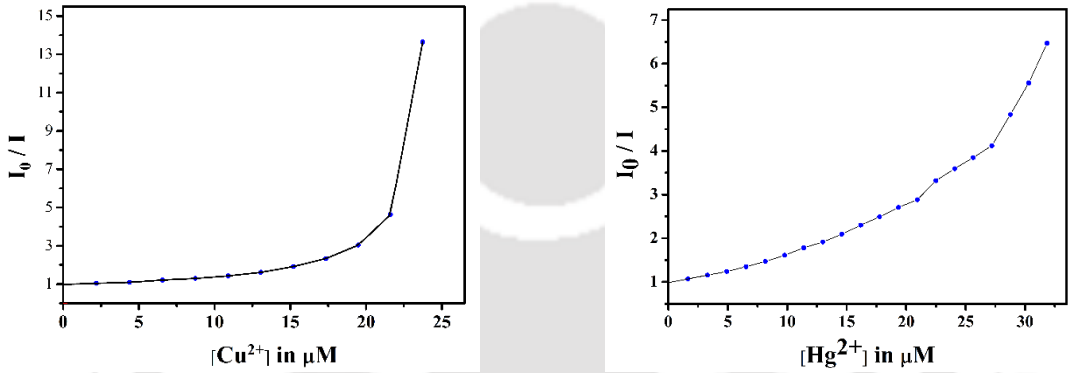

Figure A20. Stern Volmer plots for Cu^{2+} ion (left) and Hg^{2+} ion (right).

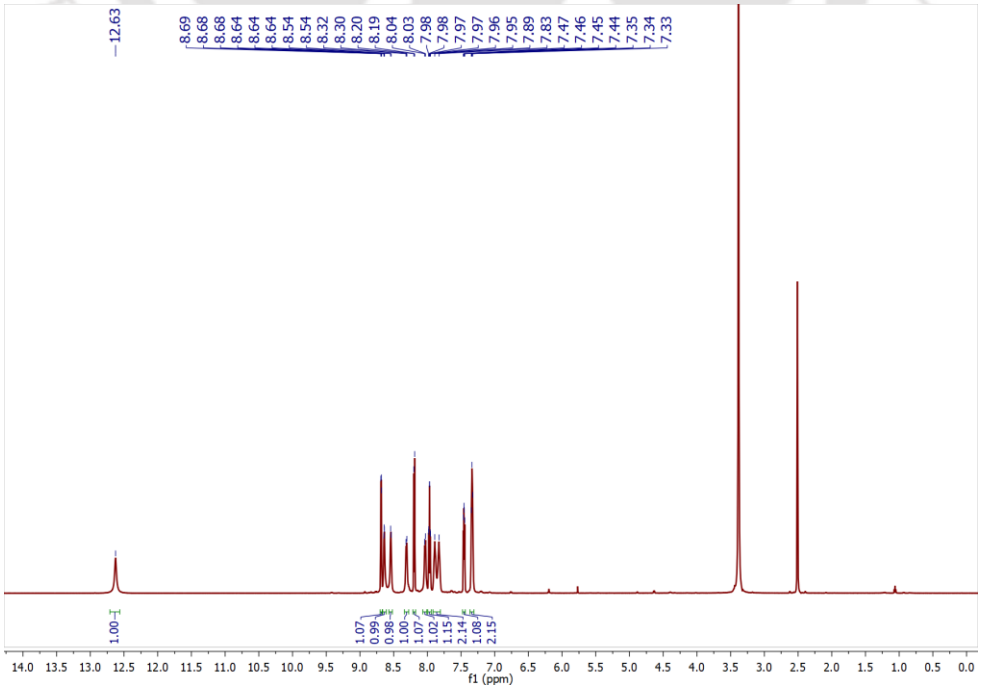

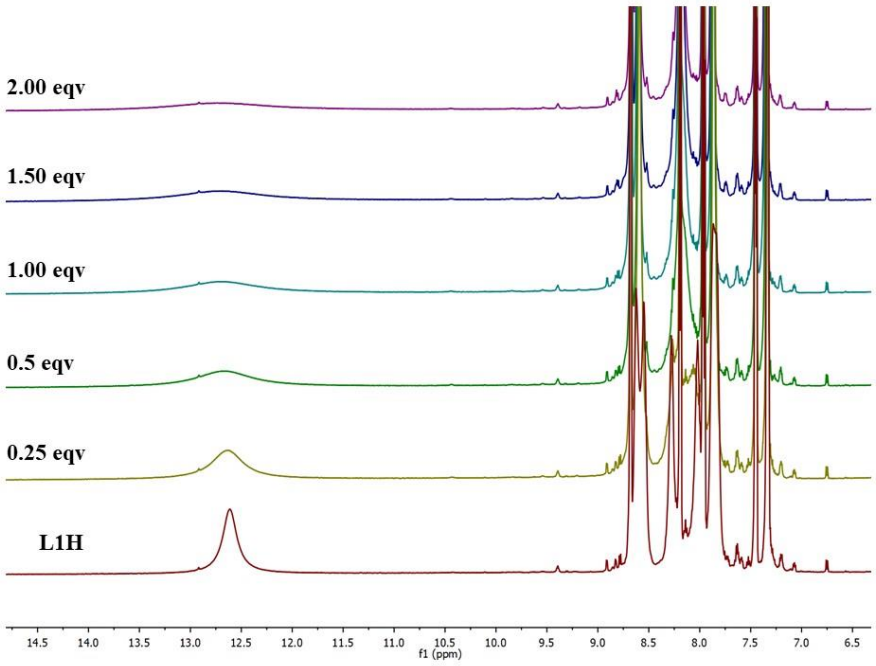

Figure A21. ^{1}H NMR of **L1H** (above) and the titration of **L1H** with $HgCl_2$ (below) in DMSO-D_6

Table A1. Frontier MOs of **1** and **2**

	1	**2**
LUMO+1	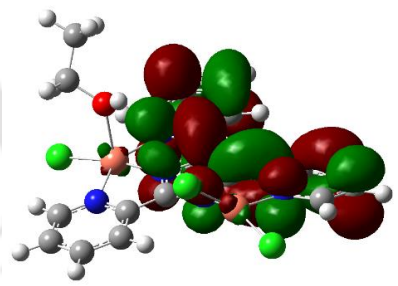 **E = -2.704 eV**	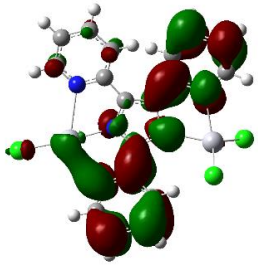 **E = -2.426 eV**
LUMO	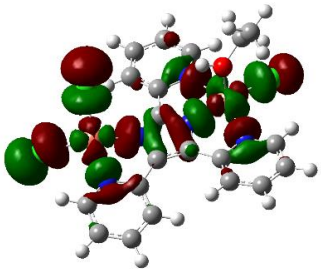 **E = -4.752 eV**	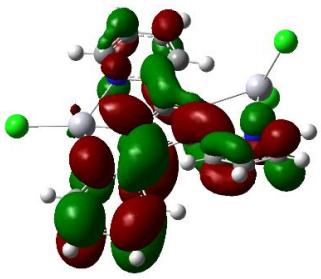 **E = -2.761 eV**

HOMO	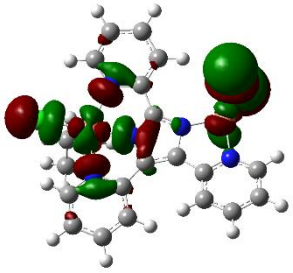	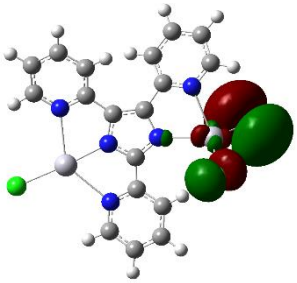
	E = -5.343 eV	**E = -6.511 eV**
HOMO-1	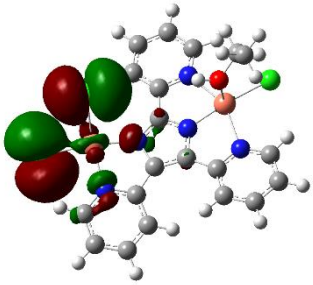	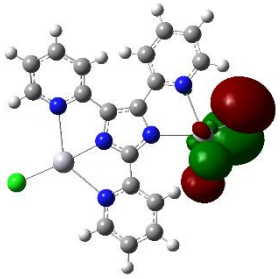
	E = -6.045 eV	**E = - 6.580 eV**
HOMO-2	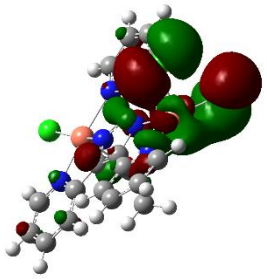	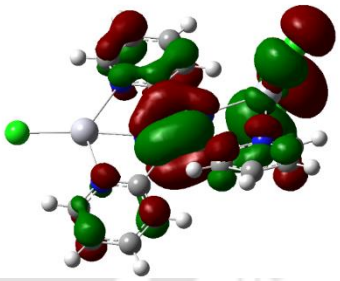
	E = -6.291 eV	**E = - 6.646 eV**
HOMO-3	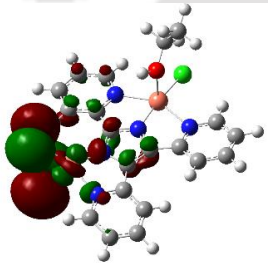	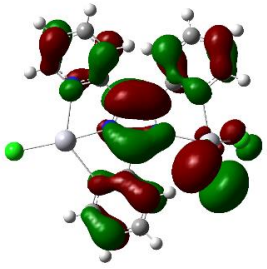
	E = -6.446 eV	**E = - 6.683 eV**
HOMO-4	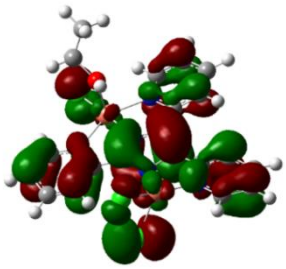	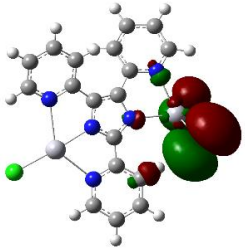
	E = -6.606 eV	**E = - 6.811 eV**

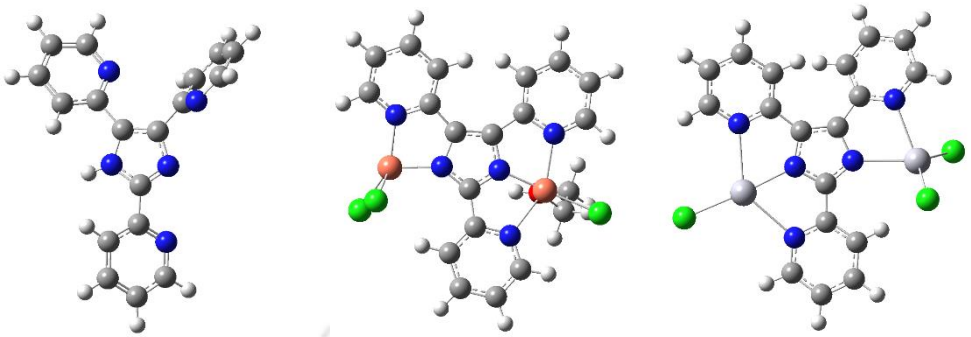

L1H **1** **2**

Figure A22. Optimised structures of the ligands and its Cu(II) and Hg(II) complexes

Table A2: Atomic Coordinates

Probe **L1H**				
Atom	Atomic No.	Coordinates (angstrom)		
		X	Y	Z
C	6	-1.66169	-0.09666	-0.05983
C	6	0.383781	-0.68655	-0.03307
C	6	0.398552	0.67492	-0.09182
N	7	-0.9301	1.041853	-0.07853
H	1	-1.27932	1.949271	-0.28223
N	7	-0.9071	-1.14167	-0.01237
C	6	-3.14319	-0.08143	-0.06697
C	6	-3.84015	0.900005	0.631192
C	6	-5.22455	0.881046	0.598003
H	1	-3.31576	1.636866	1.211317
C	6	-5.06897	-1.04748	-0.77751
C	6	-5.8599	-0.11385	-0.12207
H	1	-5.79169	1.621554	1.133622
H	1	-5.52264	-1.83927	-1.34783
H	1	-6.9312	-0.17384	-0.17524
C	6	1.468609	1.687672	-0.07515
C	6	2.312909	3.820489	0.604386
C	6	3.558356	2.308275	-0.7301
C	6	3.478736	3.531679	-0.08531
H	1	2.203641	4.750453	1.133909
H	1	4.446668	2.038085	-1.27454
H	1	4.29975	4.223374	-0.12095

C	6	1.507165	-1.6565	0.071529
C	6	2.415822	-1.82847	-0.96632
C	6	2.511717	-3.27353	1.314515
C	6	3.407645	-2.78264	-0.82719
H	1	2.343094	-1.22374	-1.84833
C	6	3.462531	-3.5269	0.339099
H	1	2.518083	-3.82629	2.238256
H	1	4.121972	-2.94281	-1.61568
H	1	4.213766	-4.28003	0.49232
N	7	-3.75129	-1.03248	-0.75689
N	7	1.559901	-2.36764	1.187447
N	7	2.584375	1.417146	-0.73637
C	6	1.293721	2.886636	0.618438
H	1	0.396552	3.065596	1.181393

Table A3: Atomic Coordinates

Complex **1**				
Atom	Atomic No.	Coordinates (angstrom)		
		X	Y	Z
Cu	29	-2.65105	-0.15228	-0.54409
N	7	-0.75889	0.158916	-0.43641
C	6	0.164655	-0.81815	-0.43413
C	6	-0.16684	1.392784	-0.30313
C	6	1.22303	1.134818	-0.25054
C	6	-2.41475	-3.27124	-1.13487
C	6	-0.37508	-2.16279	-0.68833
C	6	-1.74529	-4.50146	-1.2904
H	1	-3.49009	-3.1727	-1.24763
C	6	0.35345	-3.35409	-0.82815
C	6	-0.34805	-4.53653	-1.13168
H	1	-2.31074	-5.39742	-1.52494
H	1	1.425581	-3.3557	-0.67652
H	1	0.195098	-5.47103	-1.23802
N	7	-1.74488	-2.14001	-0.83756
N	7	1.401881	-0.26425	-0.29981
C	6	-1.16397	2.475186	-0.23631
C	6	-0.94795	3.82695	0.094039
C	6	-3.49146	2.868156	-0.46811
C	6	-2.0411	4.712536	0.113619
H	1	0.040374	4.175229	0.368506

C	6	-3.33105	4.238171	-0.1846
H	1	-4.45923	2.423728	-0.68165
H	1	-1.88535	5.75753	0.367456
H	1	-4.19213	4.898032	-0.18892
N	7	-2.44146	2.023808	-0.49084
Cu	29	3.240929	-0.82819	0.256934
C	6	4.804325	1.768213	0.024229
C	6	2.453184	1.926263	-0.23163
C	6	4.961832	3.147223	-0.1924
H	1	5.639459	1.097613	0.199142
C	6	2.554192	3.308216	-0.49325
C	6	3.817703	3.920358	-0.46643
H	1	5.952203	3.588485	-0.16363
H	1	1.673885	3.880315	-0.75821
H	1	3.909401	4.983596	-0.67107
N	7	3.582523	1.188513	0.005519
Cl	17	-4.8375	-0.44565	-1.13855
Cl	17	2.512371	-2.50619	1.656279
Cl	17	5.410948	-1.49778	0.001174
O	8	-2.88631	-0.38931	1.710544
H	1	-2.08874	-0.59958	2.238839
C	6	-4.11668	-0.87455	2.374596
H	1	-4.9054	-0.65731	1.651503
H	1	-4.04951	-1.96448	2.502931
C	6	-4.34947	-0.16655	3.711764
H	1	-5.29936	-0.49775	4.152394
H	1	-3.55036	-0.38581	4.433401
H	1	-4.39837	0.91898	3.566253

Table A4: Atomic Coordinates

Complex **2**				
Atom	Atomic No.	Coordinates (angstrom)		
		X	Y	Z
N	7	-1.27652	0.125162	0.163141
C	6	-0.23354	-0.73653	0.043584
C	6	-0.77967	1.411196	0.173286
C	6	0.630352	1.293359	0.033729
C	6	-2.1517	-3.82396	-0.38089
C	6	-0.49784	-2.18279	-0.03175
C	6	-1.21487	-4.86201	-0.23183

H	1	-3.19856	-4.03405	-0.57978
C	6	0.487056	-3.17037	0.160927
C	6	0.121099	-4.52317	0.05274
H	1	-1.53135	-5.89569	-0.32409
H	1	1.498298	-2.89611	0.441116
H	1	0.869128	-5.2958	0.203735
N	7	-1.80663	-2.51836	-0.28429
N	7	0.948655	-0.06608	-0.03149
C	6	-1.75893	2.497	0.36519
C	6	-1.44657	3.775805	0.878759
C	6	-4.04504	3.078454	0.247829
C	6	-2.47079	4.720946	1.051041
H	1	-0.42971	4.010629	1.169421
C	6	-3.79546	4.379154	0.718591
H	1	-5.05188	2.750212	0.005623
H	1	-2.23961	5.703905	1.452142
H	1	-4.61204	5.083611	0.835903
N	7	-3.06162	2.163424	0.079017
C	6	4.001537	2.769362	-0.00311
C	6	1.693848	2.300234	-0.13732
C	6	3.821046	4.08027	-0.47166
H	1	4.990984	2.385496	0.221858
C	6	1.451873	3.590027	-0.66443
C	6	2.520096	4.486134	-0.82247
H	1	4.674679	4.73925	-0.58823
H	1	0.454941	3.866991	-0.98551
H	1	2.343497	5.475818	-1.23478
N	7	2.969072	1.908434	0.165581
Cl	17	-5.80487	-0.95725	-0.41549
Cl	17	3.413645	-2.14833	2.114091
Cl	17	4.857142	-0.40962	-1.93764
Hg	80	-3.40018	-0.46127	-0.15865
Hg	80	3.373996	-0.56277	0.120012

Figure A23. Paper based sensing

Table A5

Sample	τ (ns)	χ^2
L1H	2.115	1.003
1	2.101	1.001
2	2.157	1.003

Table A6

Probes	Metal ion(s)	λ_{em} (nm)	LOD (M^{-1})	Application	Solvent
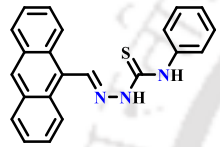	Hg^{2+} and Cu^{2+}	450 (Hg^{2+}) 475 (Cu^{2+})	0.28×10^{-9} and 0.53×10^{-8}	In macrophage (RAW 264.7) cells	CH_3CN and H_2O
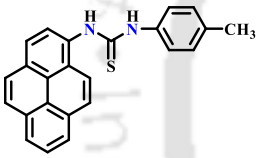	Hg^{2+} and Cu^{2}	401 (Hg^{2+}) 439 (Cu^{2+})	0.24×10^{-6} and 0.27×10^{-6}	Naked Eye Detection	DMSO/H_2O (4:1) [HEPES Buffer, pH=7.8]
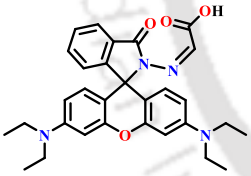	Hg^{2+} (fluorimetrically) and Cu^{2+} (Colorimetrically)	580 (Hg^{2+})	–	No cellular imaging	CH_3CN/ HEPES buffer (1:9) pH =7.4
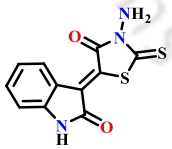	Hg^{2+} and Cu^{2+}	515 (Hg^{2+}) 498 (Cu^{2+})	3.36×10^{-6} and 2.31×10^{-6}	Solvent sensitive sensing	CH_3CN/HEPES buffer (1:9) and (1:1)
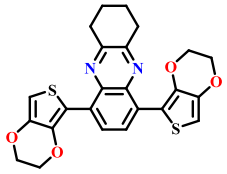	Hg^{2+}	558	40×10^{-6}	Paper and Silica based fluorescence quenching sensor	THF and water
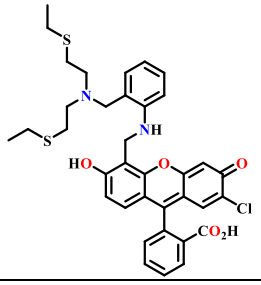	Hg^{2+}	528	< 2 ppb	Solution based sensing	50 mM PIPES buffer, 100 mM KCl buffer

Chapter 3

Ratiometric detection of Zn(II) and Cd(II) ions by a benzobisimidazole based probe in aqueous systems and theoretical calculations*

Abstract:

The probe 2,6-di(2-pyridyl)-1,5-dihydroimidazo[4,5-*f*]benzimidazole (**L2H$_2$**) was investigated for its sensing application towards metal ions. This probe can detect Zn^{2+} and Cd^{2+} ions in three different aqueous systems viz., water, DMSO/HEPES buffer (1:1, *p*H = 7.34, rt), and DMSO/water (1:1, rt). In water a "*turn-on*" response was observed for both metal ions, whereas in the latter two solvent systems, a ratiometric change in fluorescence maximum was observed. The detection limit of this probe is as low as 0.3 μM and 0.62 μM (in water) for Zn^{2+} and Cd^{2+} ions, respectively. In both DMSO/HEPES buffer and DMSO/water (1:1), LOD values were identically 1.67 μM (for Zn^{2+}) and 1.93 μM (for Cd^{2+}). This probe has a good pH tolerance range which is 4–8 (for Zn^{2+}) and 4–11 (for Cd^{2+}). Lehrer and Chipman plot and Job's plot suggested a 2:1 binding ratio between metal ion and **L2H$_2$**. The high binding constants obtained from the Lehrer and Chipman method are suggestive of the formation of a very stable complex in the solution. The binding of Zn^{2+} and Cd^{2+} ions to the probe was further confirmed by the NMR titration method which indicated the intensity of N–H protons is halved upon addition of the respective metal ion solution in DMSO-d_6. Reversibility of the detection was also established using Na_2EDTA solution. DFT/ TD-DFT calculation supported the experimentally observed red-shift of the absorption band.

* This work has been published in:

A. Bhattacharya, V. Manivannan, *J. Photochem. Photobiol. A Chem.* **2023**, *444*, 114913.

3.1 Introduction:

Bivalent zinc is the second most abundant essential transition metal ion present in the human body. Many (almost 10%) proteins bind zinc by coordination through its side chain groups having N, O and S donor atoms for their *in vivo* biological activity [1]. Since the zinc(II) ion is redox inactive, it has been found to play a vital role in the catalytic, structural and regulatory function of proteins in human body [2]. It was first found in erythrocyte carbonic anhydrase and later discovered in more than 3000 metalloenzymes [3] that include alcohol dehydrogenase, carboxypeptidase, β-lactamase, *etc*., [4–6]. Human and animal cells are known to produce zinc finger antiviral protein which targets the viral mRNA to stop the spread of the virus [7,8]. Recently the world has been through a pandemic situation due to the spread of the SARS-CoV2 virus which infects the human body by releasing mRNA after entering through the nasal or oral passage. In recent studies and hypotheses, it has been suggested that due to the antiviral activity of Zn, which includes inhibition of metabolism of RNA viruses, cellular regeneration, inhibition of RdRp enzyme, supplementation of Zn along with antiviral drugs may help infected people to heal and survive [9–13]. As the essential requirement of Zn is described above, it is also evident that its deficiency may cause several other health issues. Deficiency of Zn may affect the motor and cognitive development of children which may lead to neurophysiological problems and delayed sexual growth [14,15]. Other effects of zinc deficiency include infertility, a weak immune system etc [16–18]. Although this metal has enormous beneficial effects but its overaccumulation or imbalance may cause neurological diseases like cerebral ischemia and Alzheimer's disease [19,20].

On the other hand, cadmium which belongs to the same group, is a potential threat to living being due to its toxicity. Cadmium can enter into living organisms through industrial wastes that are released into the environment. Apart from that, Cd is found in PVC products, colour pigments, batteries, the exhaust gas of fossil fuel combustion, phosphate fertilizers *etc*. [21] When the soil gets polluted Cd gets accumulated in green leafy vegetables, thereby entering the food chain [22]. It is a non-essential metal known to disrupt many cellular mechanisms and lead to cancer development. Cadmium also creates oxidative stress by generating reactive oxygen species like hydroxide and superoxide radicals as well as hydrogen peroxide molecules. These reactive oxygen species can react with biological macromolecules, thereby increasing the chance of developing cancer [23–25]. Cadmium also induces neurological diseases due to its neurotoxic properties [26–30]. People who live in Cd-contaminated zones are often diagnosed

with bone diseases, Itai-itai disease that happened in the Jinzu river basin is a well-known incident of extreme Cd toxicity [31].

Hence, it is necessary to devise proper sensing protocols to monitor the levels of Zn^{2+} and Cd^{2+} ions. Among all the sensing and quantification techniques, the fluorometric and colorimetric sensing method is the cheapest, which can detect the presence of an analyte rapidly and precisely. Researchers worldwide have been exploring this topic meticulously and reported several such sensing protocols for Zn^{2+} and Cd^{2+} ions. An 8-aminoquinoline-based chemosensor [32] has been reported for the detection of Zn^{2+}, and it exhibited a fluorescence enhancement upon coordination with the Zn^{2+} ion. Two 2,5-diphenyl [1,3,4] oxadiazole-based chemosensors [33] were found to operate by CHEF mechanism for the detection of Zn(II) and Cd(II) ions in aqueous or alcoholic-aqueous media. The 1,8-naphthalimide-based ratiometric fluorescence sensor [34] has been reported to exhibit different fluorescence signals for Zn(II) and Cd(II) ions. A relatively simple fluorene-based probe [35] was able to detect Zn(II) and Cd(II) ions by a turn-on fluorescence mechanism. A pyrene-derived rotaxane [36] based chemosensor was developed, acting as a good Zn^{2+} sensing agent. The quinoline-based ratiometric fluorescent probe was also reported for discriminative detection [37] of Zn^{2+} and Cd^{2+} through different binding modes. The coumarin-based probe [36] was shown to detect Fe^{3+} ion colorimetrically and Zn^{2+} and Cu^{2+} ions fluorimetrically. The *N*-(quinoline-8-yl)pyridine-2-carboxamide [37] and other pyrene based [38] ligands were reported as sensors for Zn^{2+} ion, which operate through yellow fluorescence "*turn on*" response upon coordination. A simple fluorescent quinoline-based amide sensor [39] were synthesized and reported to detect Zn^{2+} in live cells. The benzothiazole functionalized ninhydrin-based receptor [40] was also reported for NIR sensing of Zn^{2+} ion.

We have reported a single (Zn^{2+}) [43] and a multi-metal (Al^{3+}, Zn^{2+} and Cd^{2+}) ion detecting probes [41,42] earlier. Recently a coumarin-based sensor for Al^{3+}, Cr^{3+} and Fe^{3+} ions [45] and a 1,8-naphthalimide-based probe [43,44] were also reported by us along with a "*turn off*" sensor [45] for Cu^{2+} and Hg^{2+} ions. As a part of our continuing interest in the search for new probes for the detection of metal ions, we come across benzobisimidazole moiety being used as fluorescent tunable dyes [46,47], in sensing of CO_2 [48] and preparation of fluorescent metal–organic framework [47]. In this Chapter, the utility of 2,6-di(2- pyridyl)-1,5-dihydroimidazo[4,5-*f*]benzimidazole (**L2H$_2$**), synthesized from 1,2,4,5-tetraaminobenzene tetrachloride and 2-picolylamine [49], as sensor for Zn^{2+} and Cd^{2+} ions were reported.

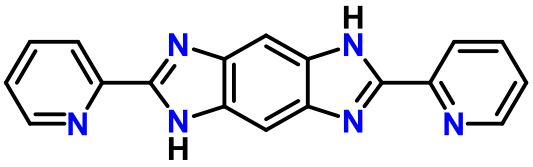

L2H$_2$

3.2 Experimental Section:

3.2.1 Determination of the Binding Stoichiometry

The association constant of the 2:1 complexes were determined by Lehrer and Chipman method

$$ln\left[\frac{(F-F_0)}{(F-F_\alpha)}\right] = n\ln[M^{2+}] + n\ln K_A$$

Where F = Absorbance with respect to a definite concentration of metal ion
F_0 = Absorbance of the ligand **L2H$_2$** in the absence of any metal ion
F_α = Absorbance of the ligand **L2H$_2$** at saturation point
n = No. of metal ions attached to the ligand
K_A = Association constant

The binding stoichiometry of the ligand **L2H$_2$** with Zn^{2+} and Cd^{2+} ions were also determined by Job's Plot.

3.3 Results and Discussion

The ligand **L2H$_2$** was synthesized according to the procedure reported by Siri and coworkers [49]. It was dissolved in DMSO and used for all the spectroscopic studies. This ligand has two 2-pyridinyl and two imidazolyl nitrogen donor atoms which can coordinate to the metal ions in a bis-bidentate fashion. Also, because of the presence of two dissociable protons, it may coordinate as **L2H$_2$** (neutral molecule) or **L2H$^-$** (mono anion) or **L2^{2-}** (di-anion).

3.3.1 UV-Visible spectra

In DMSO/HEPES buffer, ligand **L2H$_2$** showed an absorption maximum at 354 nm corresponding to the π-π* transition, along with a shoulder at 370 nm. UV visible spectra of **L2H$_2$** were recorded in the presence of metal ions (Figure 1) such as Li^+, Na^+, K^+, Mg^{2+}, Ca^{2+}, Al^{3+}, Fe^{3+}, Co^{2+}, Cu^{2+}, Cd^{2+}, Hg^{2+}, Pb^{2+}, Au^{3+}, Ag^+, Pd^{2+}, Zn^{2+}, Cr^{3+}, Ni^{2+} and Mn^{2+}. From these spectra, it was observed that there was a shift in the peak from 354 to 368 nm (in Zn^{2+}), 370 nm (in Cd^{2+}), 365 nm (in Hg^{2+}), 376 nm (in Cu^{2+}), and 377 nm (in Co^{2+} and Ni^{2+}). In case of Fe^{3+}, the intensity of the 354 nm peak increased (~30%), while in Ag^+, got decreased (70 %).

Spectral features for the rest of the metal ions, *viz*., Na^{+}, K^{+}, Al^{3+}, Pb^{2+}, Pd^{2+} and Cr^{3+}, remained nearly identical. This indicates that the shift in absorption maximum occurs when the probe **L2H₂** gets coordinated with Zn^{2+}, Cd^{2+}, Hg^{2+}, Cu^{2+}, Co^{2+} and Ni^{2+} ions. As the fluorescence titration study (*vide infra*) of the probe **L2H₂** with these metal ions indicated that a shift in the emission maximum was observed with only Zn^{2+} and Cd^{2+} ions, hence, UV–Vis titration experiment was carried out by gradual addition of $ZnCl_2$ and $CdCl_2$ until saturation (3 equivalent) (Figure 2). Upon titration, with $ZnCl_2$, a perceptible change in the spectra was observed with the shift of λ_{max} from 354 to 368 nm along with appearance of an isosbestic point at 377 nm. In the case of $CdCl_2$, the intensity of the 354 nm peak decreased slightly to become nearly equal to the shoulder at 370 nm accompanied by an isosbestic point at 377 nm.

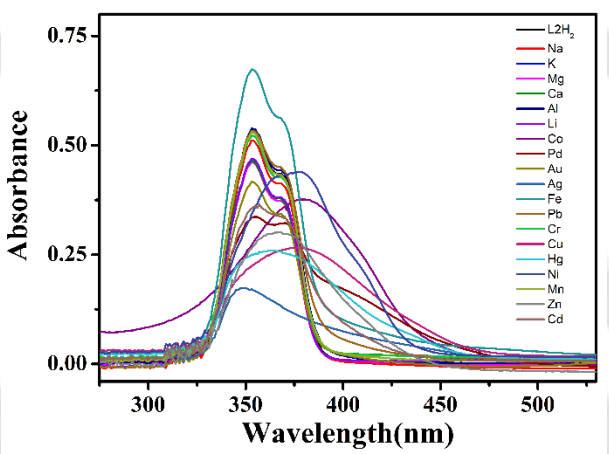

Figure 1: Absorption spectra of **L2H₂** (1.315×10^{-5} M) in presence of different metal ions (3 equivalents) in DMSO/HEPES buffer (5 mM, pH = 7.34, 1:1, *v/v*).

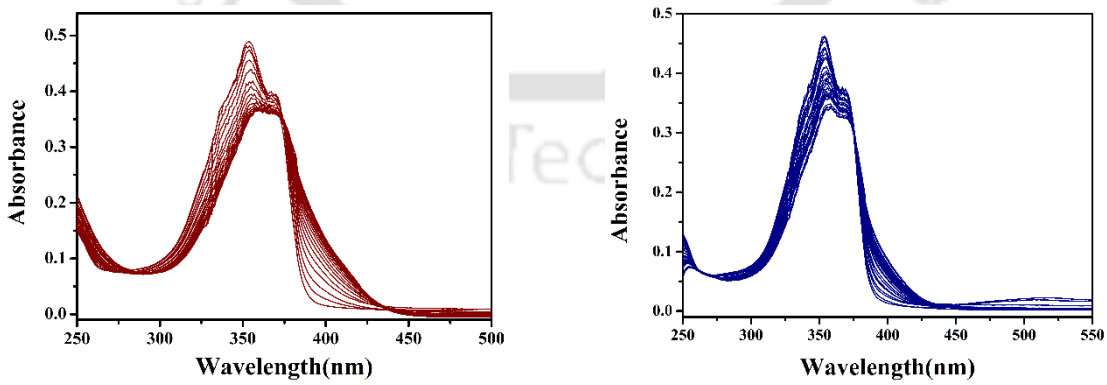

(a) **(b)**

Figure 2: UV-Visible titration of **L2H₂** (1.315×10^{-5} M) with (a) $ZnCl_2$ (0-3 eqv.) and (b) $CdCl_2$ (0-3 eqv.) in DMSO/HEPES buffer (5 mM, pH = 7.34, 1:1, *v/v*).

3.3.2 Emission spectra

The probe is a fluorescent molecule when observed under the long UV light lamp, showing a purple fluorescence. Probe **L2H2** has an absorption band at λ_{max} = 354 nm; upon excitation with 354 nm light an emission band having a peak at 412 nm was observed in DMSO/HEPES. In DMSO, **L2H2** also exhibited emission at λ_{em} = 412 nm, the intensity of which gradually reduced with an increase in water content percentage. Examination of the fluorescence behavior of **L2H2** in various ratios of DMSO:H_2O revealed that intensity decreased with an increasing amount of water which eventually got quenched in 100% H_2O. This quenching is due to Aggregation Caused Quenching (ACQ) of fluorescence intensity of **L2H2** in water (Figure A1). Hence the probe is non-fluorescent in water, can possibly function as a "*turn-on*" sensor if the aggregation of **L2H2** gets dismantled in the presence of metal ions. Indeed, this was observed upon adding Zn^{2+} and Cd^{2+} ions to the solution of **L2H2** thereby acting as a "*turn-on*" fluorescence sensor towards these two ions (Figure A1). In a typical titration experiment, a 20 μL stock solution of **L2H2** was added to 3.0 mL of water and the emission spectrum was recorded. The resultant solution was weakly emissive (λ_{em} = 422 nm) but upon gradual addition of $ZnCl_2$ solution, this emission peak shifted gradually to λ_{em} = 457 nm and also grew in intensity (~4.7 times), which reached a maximum after the addition of 3 equivalents. Similar behaviour was observed while adding $CdCl_2$ solution with λ_{em} shifting to 455 nm (Figure 3). With the addition of all other metal ions *viz*., Li^+, Na^+, K^+, Mg^{2+}, Ca^{2+}, Al^{3+}, Fe^{3+}, Co^{2+}, Cu^{2+}, Cd^{2+}, Hg^{2+}, Pb^{2+}, Au^{3+}, Ag^+, Pd^{2+}, Zn^{2+}, Cr^{3+}, Ni^{2+} and Mn^{2+} any perceptible change in emission profile was not observed. Thus, **L2H2** was indeed able to detect Zn^{2+} and Cd^{2+} ions in water through "turn-on" fluorescence mechanism.

The selective recognition by **L2H2** towards Zn^{2+} and Cd^{2+} ions was checked in DMSO/water (1:1) system (Figure 4) as well as in DMSO/HEPES buffer. Titration study in DMSO/water (1:1) and DMSO/HEPES buffer by gradual addition of metal ions (up to 3 equivalents) to **L2H2** indicated that the fluorescence intensity was (a) entirely quenched by Cu^{2+}, Ni^{2+} and Ag^{2+}, (b) partially by Hg^{2+} (91%), Co^{2+} (67%), Au^{3+} (31%), (c) a slight decrease in intensity in Mn^{2+}, Ca^{2+}, Pb^{2+}, Fe^{3+}, Cr^{3+}, Pd^{2+}, (d) intensity remained same in Li^+, Na^+, K^+, Mg^{2+}, Al^{3+} and (e) a red shift in emission from λ_{em} = 412 to 439 nm upon adding Zn^{2+} and Cd^{2+} ions was observed (Figure 5). In DMSO/water (1:1) medium the initial emission band observed at 412 nm got red shifted to 445 nm upon addition of $ZnCl_2$ to **L2H2** with appearance of an isoemissive point at 425 nm. The probe showed ratiometric characteristics in presence of Zn^{2+} ions. In case of $CdCl_2$

similar observation was obtained where the emission band was red-shifted to 435 nm. In DMSO/HEPES, during titration of **L2H₂** with $ZnCl_2$, the intensity of the 412 nm peak decreased slightly (20%) and got red-shifted to 439 nm with the presence of an isoemissive point at 439 nm. In titration with $CdCl_2$, intensity of 412 nm peak also decreased by 39% and got red-shifted to 439 nm. Concomitantly, the isoemissive point appeared at 451 nm. In both cases the red shift was observed which suggested that the excited state was stabilised by coordination of metal ions (Figure 6).

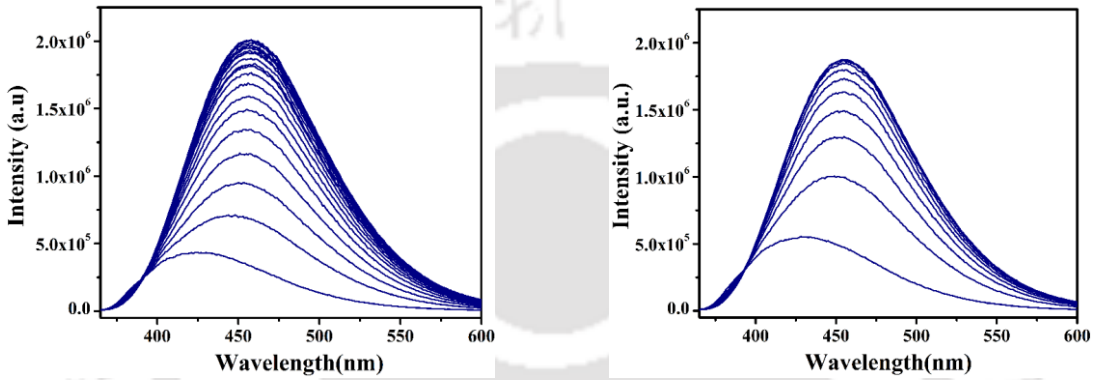

(a) **(b)**

Figure 3: Fluorescence titration (λ_{ex} = 354 nm) of **L2H₂** (1.315×10^{-5} M) in water (100%, *v*/*v*) with (a) $ZnCl_2$ (0-3 eqv.) and (b) $CdCl_2$.(0-3 eqv.)

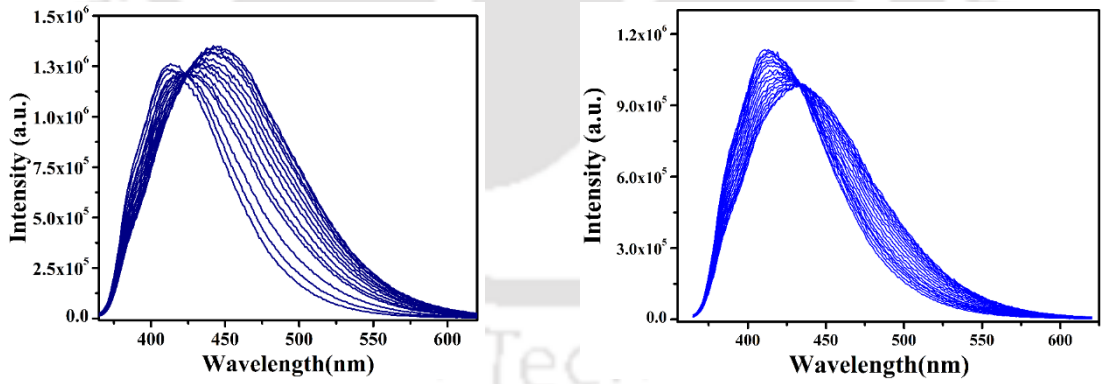

(a) **(b)**

Figure 4: Fluorescence titration (λ_{ex} = 354 nm) of **L2H₂** (1.315×10^{-5} M) in DMSO/Water (1:1) with (a) $ZnCl_2$ (0-3 eqv.) and (b) $CdCl_2$.(0-3 eqv.)

3.3.3 Binding stoichiometry

For a sensor that involves forming a metal to ligand complex, determining the binding stoichiometry is essential and Job's plot of continuous variation was employed in this case (in DMSO/HEPES). Typically, the variation in the intensity of absorption peak at λ_{max} = 354 nm

of **L2H₂** upon gradual addition of analyte ($ZnCl_2$ and $CdCl_2$) was used to obtain the Job's Plot. The ratio of 2:1 (M^{2+}:**L2H₂**) was unequivocally obtained from the plot (Figure A2), which indicated that one ligand got coordinated with two Zn^{2+} and Cd^{2+} ions. Thus, one molecule of **L2H₂** sequestered two metal ions by coordinating in a bis-bidentate fashion with the rest of the two coordination sites occupied by solvent water and/or chloride ions.

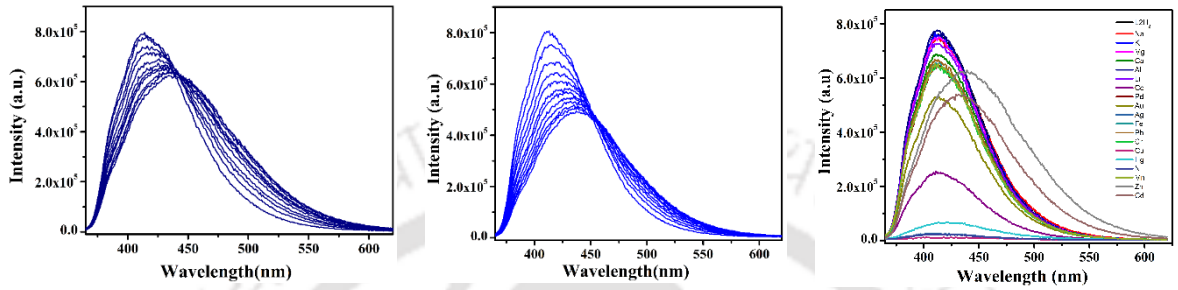

Figure 5: Fluorescence titration experiment in DMSO/HEPES buffer (5 mM, pH = 7.34, 1:1, *v*/*v*) for (a) Zn^{2+} and (b) Cd^{2+} ions. (c) Comparison of emission spectra in the presence of different metal ions.

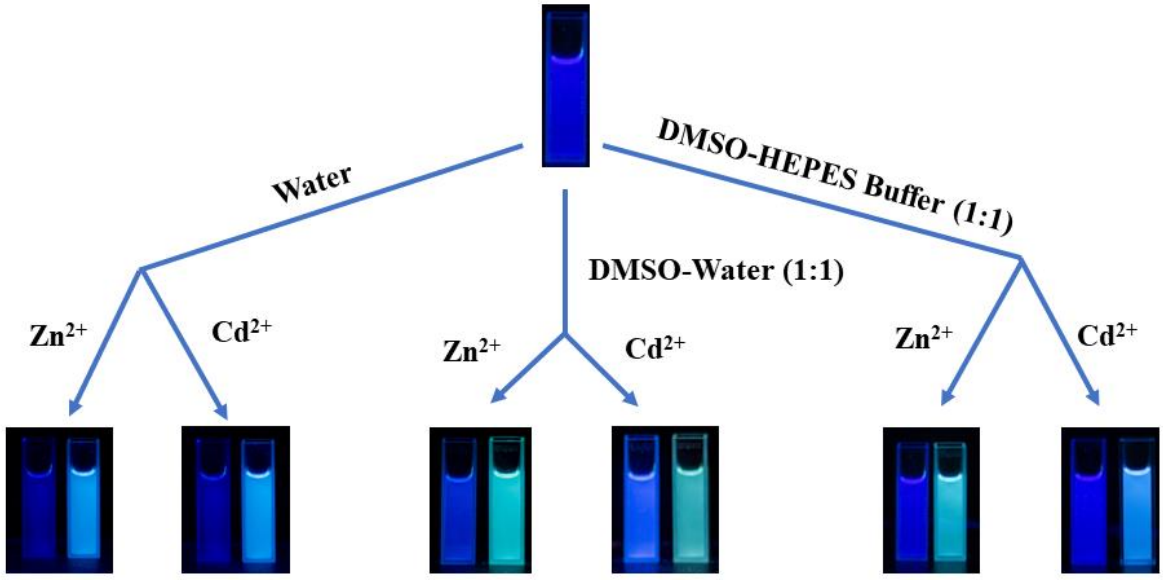

Figure 6: Schematic representation of the ratiometric/turn on response in presence of Zn^{2+} and the Cd^{2+} metal ion solutions

Since Job's plot in DMSO/HEPES buffer system was obtained as 2:1 (M^{2+}:**L2H₂**), Benesi-Hildebrand plot could not be of any help in determining the binding constants as it is applicable to binding ratio of 1:1. So, the method coined by Lehrer and Chipman was used [50–52] to obtain the binding constant of the complexes. The binding constant in DMSO-water were calculated

to be 1.79×10^5 M^{-2} (for Zn- **L2H₂**) and 6.48×10^4 M^{-2} (for Cd- **L2H₂**) with respective slopes as 1.78 and 1.94 (Figure A3). In water, the same was calculated as 2.733×10^5 M^{-2} (for Zn- **L2H₂**) and 2.02×10^5 M^{-2} (for Cd- **L2H₂**) with slopes of 1.75 and 1.83, respectively (Figure S4). As the binding constant values are indicative of stability of the metal- **L2H₂** complex, from these values one can understand the stability of the metal:ligand complex that has formed *in-situ*. From high binding constant values, it is evident that a stable complex is formed between **L2H₂** and both metal (Zn^{2+} and Cd^{2+}) ions. The slope of the fitted line in the Lehrer and Chipman method is equal to the number of guest molecules attached to the host. Values obtained from these slopes lie in the range of 1.75 – 1.94, consistent with the stoichiometry of 2:1 (M^{2+}: **L2H₂**) as observed in the Jobs method. The binding stoichiometry of 2:1 (between metal and ligand) has been ascertained by ESI(+) mass spectrometric analysis. The obtained *m*/*z* values of 512.19 and 685.44 matched well with the calculated values of 512.90 and 685.85 for $[Zn_2(\mathbf{L2H})Cl_2]^+$ (M+) and $[Cd_2(\mathbf{L2H})(CH_3CN)Cl_3+H]^+$ respectively (Figure A11 and A12).

3.3.4. Limit of detection

The limit of detection (LOD) of a probe towards its analytes is a crucial parameter to understand the accuracy and practical applicability. Here we examined the probe's limit of detection in DMSO/HEPES buffer (1:1, pH = 7.34, rt, *v*/*v*) and in water. In the case of DMSO/HEPES buffer system, the emission intensity at λ_{em} = 412 nm was used for constructing the calibration plot (Figure A5) and for 100% water solvent emission intensity (after the addition of the metal ions) at λ_{em} = 457 nm (for Zn^{2+}) and λ_{em} = 455 nm (for Cd^{2+}) were used (Figure A6). The LOD of **L2H₂** in DMSO/HEPES and in DMSO:H_2O (1:1) mixture was calculated to be 1.67 µM and 1.93 µM (for Cd^{2+}), as the change in the fluorescence response were nearly comparable in both solvent systems. But the LOD of the probe became better with 0.3 µM (for Zn^{2+}) and 0.62 µM (for Cd^{2+}) when tested in water. The LOD of this probe **L2H₂** is comparable with those listed in Table A1. It makes water a better-suited solvent for utilizing **L2H₂** as a more viable sensor for Zn^{2+} and Cd^{2+} ions due to lower values of the limit of detection.

3.3.5 Effect of pH

Probe **L2H₂** has four sp^2 hybridised nitrogen atoms which are basic in character and two dissociable protons; hence, for detecting metal ions in solution, the pH of the medium is essential factor for sensing ability of a probe. Solutions of different pH of the range 2-13 were mixed with DMSO in a 1:1 ratio. To this, **L2H₂** was added and fluorescence spectra were

recorded firstly for the free probe and then after adding metal ions to **L2H₂**. The λ_{em} of **L2H₂** was found to be 454 nm at pH = 2, 445 nm at pH = 3, 419 nm at pH = 4 and 412 nm at pH = 5. Emission spectrum of **L2H₂** at pH ≥ 4 started resembling to that of **L2H₂** in 1:1 DMSO:H_2O and upon increasing the pH further, the intensity of the peak at 412 nm peak decreased gradually as shown in Figure A7. From Figure A7, it was understandable that the emission band was red-shifted below pH = 4, and the probe showed its original emission band (as observed in DMSO:H_2O) above pH = 4. Upon adding $ZnCl_2$ to the probe, the shift of 412 nm peak to 460 nm was observed in the pH range 4-8 (Figure A8), so the Zn^{2+} ion was detectable only in this range. Above pH = 8, characteristic emission spectra of the free ligand were observed. However, upon adding $CdCl_2$, 412 nm peak shifted to 439 nm, which was preserved in the pH range of 4-11. Beyond that pH window, the fluorescence intensity got diminished and shifted toward 412 nm.

As this probe showed selectivity towards both Zn^{2+} and Cd^{2+} and the color of the fluorescence was also non differentiable but the only difference is the pH window. That is within the pH window of 4-8 both metal ions are detectable and in the pH range 9-11 only Cd^{2+} ion can be detected. Thus, if the red shift is observed only in the pH range of 4-8 but no such shift beyond pH = 8 then the sample contains only Zn^{2+} ion and there is no Cd^{2+} ion. If the probe shows red shift of emission peak beyond pH = 8 then the sample contains only Cd^{2+} ions.

3.3.6 Reversibility of binding

For testing the reversibility of **L2H₂** in the detection of Zn^{2+} and Cd^{2+} ions, the sequestering agent, Na_2EDTA was used. To the solution containing probe bound to metal ions (Zn^{2+} and Cd^{2+} ions) in DMSO/HEPES, an aqueous solution of Na_2EDTA was added, which resulted in the release of free **L2H₂** while $Zn(EDTA)^{2-}$ and $Cd(EDTA)^{2-}$ remained in solution. This cycle was repeated three times and the characteristic emission spectrum of free **L2H₂** reappeared every time. Figures A9 and A10 establish that the probe can be used for several cycles to detect the metal ions Zn^{2+} and Cd^{2+} ions.

3.3.7 ^{1}H NMR titration

For ascertaining the binding of **L2H₂** with Zn^{2+} and Cd^{2+} ions, ^{1}H NMR titration experiment was carried out in DMSO-d_6 as the solvent. The DMSO-d_6 solutions of $ZnCl_2$ and $CdCl_2$ were gradually added to the solution of **L2H₂** and ^{1}H NMR spectra were recorded after each addition.

In general, peaks in the aromatic region and the one at 12.93 ppm due to N–H proton, broadened slightly (Figure 7 and 8).

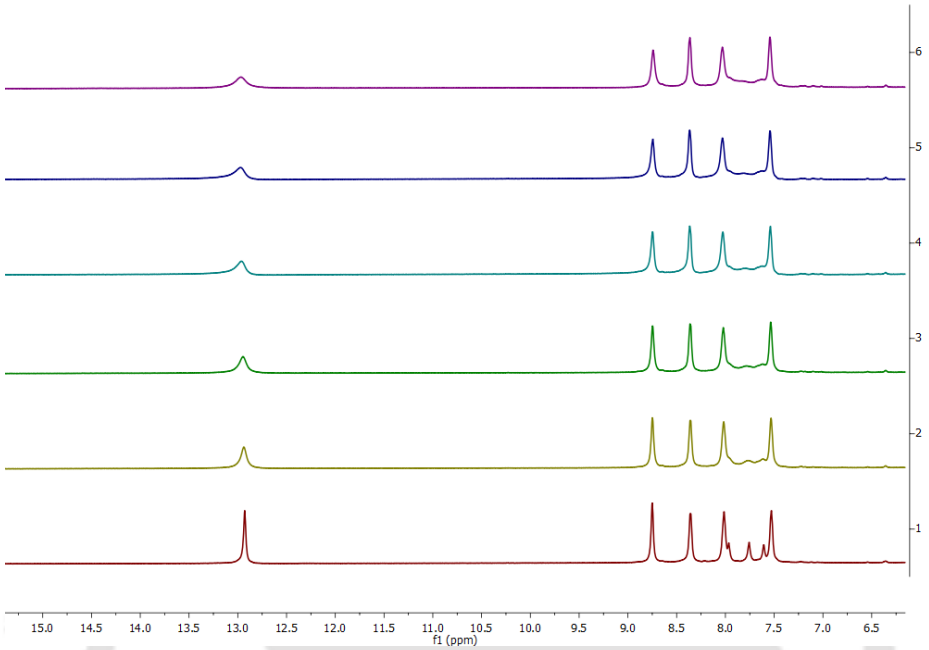

Figure 7: ^{1}H NMR titration of **L2H$_2$** with $ZnCl_2$ (0-2 eqv.)

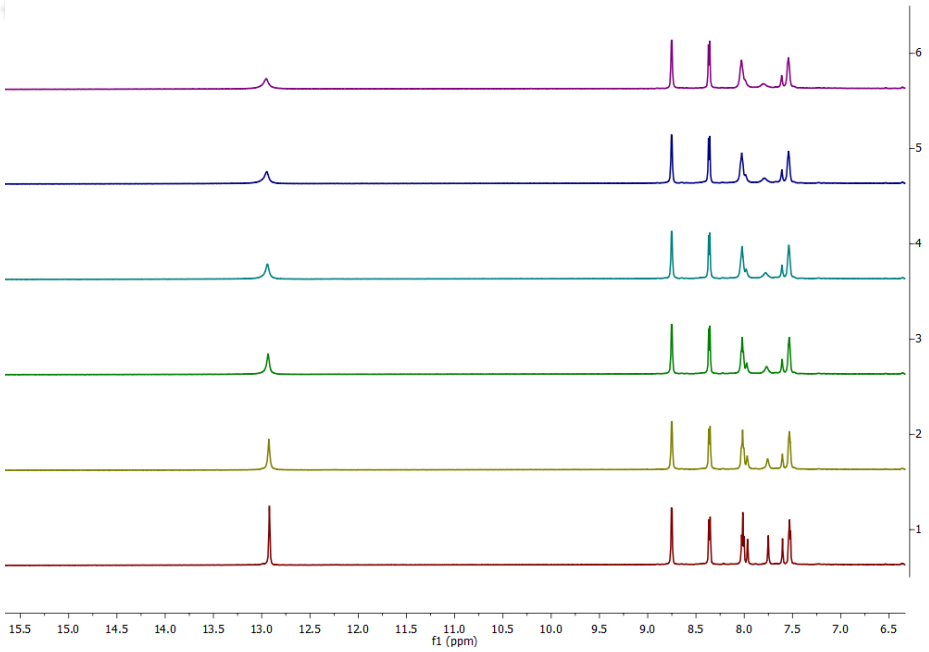

Figure 8: ^{1}H NMR titration of **L2H$_2$** with $CdCl_2$. (0-2 eqv.)

In NMR titration experiment, it is observed that the intensity of N–H proton at 12.93 ppm got halved upon the addition of 2 equivalents of metal ions to the solution of **L2H$_2$** in DMSO-d_6.

This indicates that, among two dissociable N–H protons, only one got dissociated in the presence of $ZnCl_2$ and $CdCl_2$. Hence the composition $[M_2(\mathbf{L2H})(H_2O)Cl_3]$ (M = Zn, Cd) was formulated and this result is supported by the Gaussian Calculations.

3.3.8 Time resolved photo-luminescence and quantum yield

Time dependent photo luminescence study was also carried out to obtain the excited state lifetime of **L2H₂** and the effect of the presence of Zn^{2+} and Cd^{2+} ions on lifetime (Figure 9). The excited state lifetime of **L2H₂** was found to be 0.597 ns which increased significantly to 3.600 ns with $ZnCl_2$ and 2.847 ns with $CdCl_2$ (Table 1). This observation supports the fact that there is strong coordination of **L2H₂** with both these metal ions. Coordination with the metal ions makes the ligand framework rigid by preventing rotation around single bond, thus increasing the chance of ICT process between benzobisimidazole moiety and terminal pyridine rings.

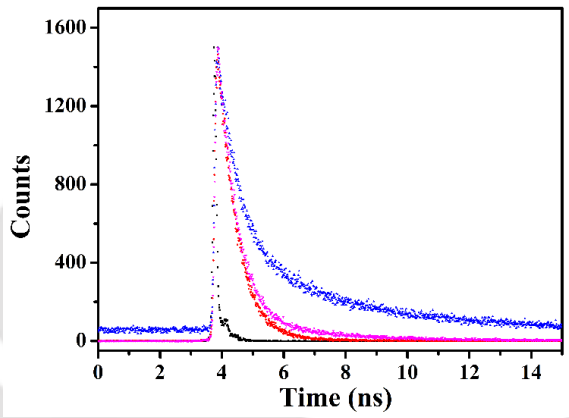

Figure 9: Fluorescence decay profile of **L2H₂** (red), in presence of $ZnCl_2$ (blue), $CdCl_2$ (pink) and IRF (black).

Quantum yield (Φ) of the probe and its complexes were determined in relative method [53–55] taking quinine sulphate (dissolved in 0.1 M H_2SO_4) as reference. From Φ values it is understandable that upon coordination with metal ions, the probe exhibited "*turn-on*" response in water medium wherein Φ got enhanced to 19.75% and 16.07% (for Zn-**L2H₂** and Cd-**L2H₂** respectively) from 3.54% (for **L2H₂**). The same trend was followed in DMSO/Water (1:1) medium as well wherein Φ of 15.08% (for **L2H₂**) got enhanced to 27.20% (for Zn- **L2H₂**) and 20.50% (Cd- **L2H₂**) complexes. In DMSO/HEPES buffer (5 mM, pH = 7.34, 1:1, *v*/*v*) the enhancement was relatively less, which was due to decrease in intensity of the emission band after addition of $ZnCl_2$ and $CdCl_2$. These quantum yield data (Table 2) support the fact that

upon coordination the ligand framework attained the rigid form and as a result there was increase in Φ values.

Table 1: Fluorescence lifetime of **L2H$_2$**, Zn-**L2H$_2$** and Cd-**L2H$_2$**.

	L2H$_2$	Zn-**L2H$_2$**	Cd-**L2H$_2$**
Lifetime (ns)	0.597	3.600	2.847
χ^2	1.000	1.070	1.063

Table 2: Quantum yield (Φ, in %) of quinine sulfate (reference), **L2H$_2$**, **L2H$_2$** with $ZnCl_2$ and **L2H$_2$** with $CdCl_2$.

Solvent	**L2H$_2$**	**L2H$_2$** with $ZnCl_2$	**L2H$_2$** with $CdCl_2$	**Reference**
Water	3.54	19.75	16.07	54.00
DMSO/Water (1:1)	15.08	27.20	20.50	
DMSO/HEPES buffer (5 mM, pH = 7.34, 1:1, *v*/*v*)	14.69	15.88	18.08	

3.3.9 Computational analysis

To support UV-Vis spectral observations, DFT/TDDFT calculation were performed on **L2H$_2$**, [Zn_2(**L2H**)(H_2O)Cl_3] (**1**) and [Cd_2(**L2H**)(H_2O)Cl_3] (**2**) complexes. The optimization and TD-DFT energy calculation of **L2H$_2$** was done in 6-31+G(d,p) basis set at B3LYP level, while for **1** and **2**, LANL2DZ was used. From optimised the structure of **L2H$_2$**, it was observed that, two pyridine rings were not in the same plane with the central benzobisimidazole ring. The dihedral angles between the central ring and terminal pyridine rings in **L2H$_2$** were calculated to be 25.8°. However, in **1** and **2**, it was found to be 2.0°, indicating that near planarity was reached upon coordination of **L2H$^-$**, to metal ions (Table A2). In both **1** and **2**, metal centers have the coordination environment of N_2OCl and N_2Cl_2. Similar calculations performed on [M_2(**L2H$_2$**)Cl_4] (**3** = Zn, **4** = Cd) and [M_2(**L2**)(H_2O)$_2Cl_2$] (**5** = Zn, **6** = Cd) indicated that formulations **1** and **2** were the best suited with the experimental observations.

The HOMO and LUMO of **L2H$_2$** reside at the energy levels -5.6953 eV and -1.9660 eV, respectively with a difference (ΔE) of 3.7293 eV. In the HOMO, electron distribution is

observed to be concentrated mainly on the central benzobisimidazole ring, while in LUMO, distribution is observed to be majorly on imidazole and pyridine rings.

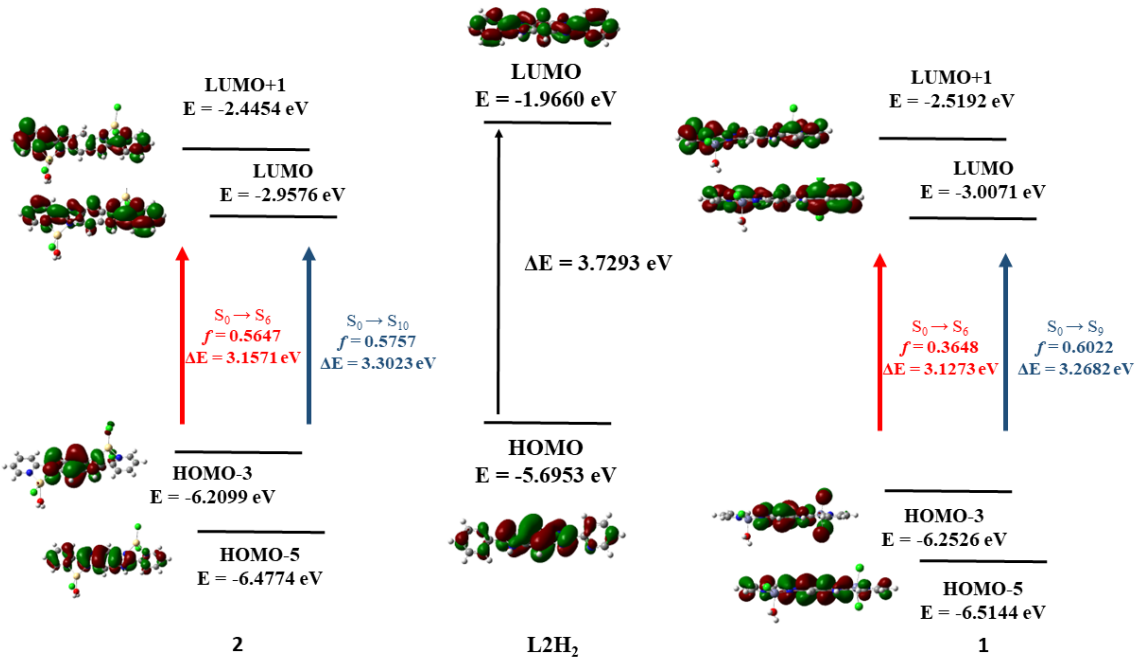

Figure 10: Ligand based FMO and electronic transitions in gas phase

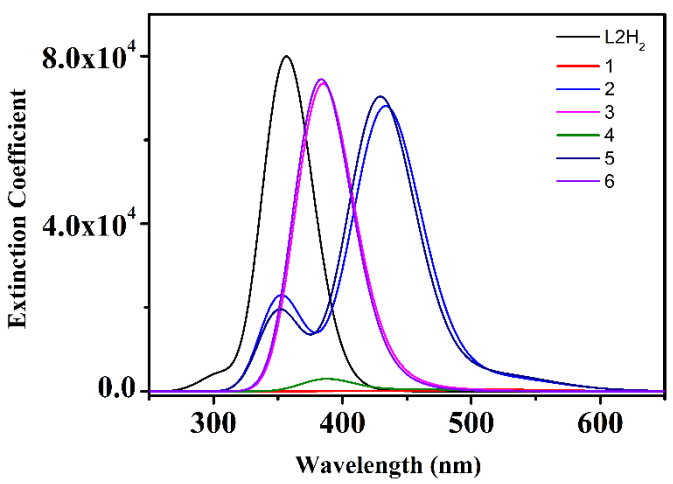

Figure 11: UV-Spectra obtained from the gaussian calculation performed in Gas phase.

In **1** and **2**, HOMO-5 corresponds to HOMO of **L2H2** and HOMO-3, having distribution on the central ring appear in addition, possibly due to an unsymmetrical coordination environment at two metal sites. The remaining FMOs, *viz*., HOMO, HOMO-1, HOMO-2 and HOMO-4 were of lone-pair of electrons on chloride ligands at the $M(N_2Cl_2)$ site (Table A3). LUMO of **1** and **2** correspond to that of **L2H2** and LUMO+1 appeared additionally due to two different

coodination environments. Upon coordination, LUMO and LUMO+1 were observed to be stabilised in both complexes and energies of HOMO-3 and HOMO-5 were lower than that of HOMO in **L2H$_2$** (Figure 10). Electronic transitions were observed to be of $S_0 \rightarrow S_6$ and $S_0 \rightarrow S_{10}$ in origin. The calculated energy of these two transitions were 3.1571 and 3.3023 eV (for **2),** mostly comprised of the transitions between HOMO-3 to LUMO+1 and HOMO-5 to LUMO. For **1** the energy of transitions due to $S_0 \rightarrow S_6$ and $S_0 \rightarrow S_9$ were 3.1273 and 3.2628 eV, respectively corresponding to transitions from HOMO-3 to LUMO+1 and HOMO-5 to LUMO. From these calculations λ_{max} obtained at 356 nm for **L2H$_2$** was shifted to 385 (in **1**) and 383 (in **2**) nm. Net effect of coordination is the decrement of the energy differences resulting in the red-shifting absorption band (Figure 11) of corresponding electronic transition.

3.3.10 Mechanism of Sensing

From the DFT calculation it was found that the dihedral angle between the central ring and two terminal pyridine rings got reduced from 25.8° to 2.0° upon coordination, which forces the molecule to achieve near planarity. In this planar ligand, extended conjugation would be more efficient which lowered the energy of both LUMO and LUMO+1 levels. This was validated experimentally by the red shift of the emission peak upon addition of metal ions to **L2H$_2$**. Due the attainment of rigidity upon coordination, the fluorescence lifetime and quantum yields got enhanced [56] thereby the internal charge transfer process becoming more efficient in these complexes which was refelected as ratiometric shift in emission peak.

3.4. Conclusion:

The probe **L2H$_2$** is fluorescent in DMSO/HEPES buffer and DMSO/Water (1:1), which upon coordination with Zn^{2+} and Cd^{2+} ions, exhibited a significant ratiometric red shift in the emission maximum accompanied by a change in fluorescence colour from violet blue to bluish green, that was comprehensible by the naked eye. In pure water, **L2H$_2$** was non-fluorescent and a "*turn-on*" response was observed in the presence of Zn^{2+} and Cd^{2+} ions. The LOD values were found to be lesser in water than in the other two solvent systems. The metal-to-probe binding stoichiometry was determined as 2:1 and had very high binding constants (~10^5), indicating stable complex formation. For the detection of Zn^{2+} ions, the optimum pH range was found to be 4-8 and for Cd^{2+}, 4-11. The addition of Na_2EDTA solution can free the probe into the solution. The ^1H NMR titration study revealed the loss of one proton upon coordination. Theoretical calculation on **L2H$_2$**, [Zn_2(**L2H**)(H_2O)Cl_3] and [Cd_2(**L2H**)(H_2O)Cl_3], supported

the experimentally observed red-shift of the electronic spectral band. So, as a whole, **L2H$_2$** can potentially be a ratiometric sensor for Zn^{2+} and Cd^{2+} ions in three different solvent systems, specifically as a "*turn-on*" sensor in water.

References:

[1] A. Krężel, W. Maret, *Arch. Biochem. Biophys.* **2016**, *611*, 3–19.

[2] W. Maret, *Int. J. Mol. Sci.* **2017**, *18*, 2285.

[3] W. Maret, *Adv. Nutr.* **2013**, *4*, 82–91.

[4] W. Maret, Y. Li, *Chem. Rev.* **2009**, *109*, 4682–4707.

[5] M. Hambidge, R. J. Cousins, R. B. Costello, *J. Nutr.* **2000**, *130*, 1341S-1343S.

[6] B. L. Vallee, D. S. Auld, *Biochemistry* **1990**, *29*, 5647–5659.

[7] X. Guo, J.-W. N. Carroll, M. R. MacDonald, S. P. Goff, G. Gao, *J. Virol.* **2004**, *78*, 12781–12787.

[8] J. L. Meagher, M. Takata, D. Gonçalves-Carneiro, S. C. Keane, A. Rebendenne, H. Ong, V. K. Orr, M. R. MacDonald, J. A. Stuckey, P. D. Bieniasz, J. L. Smith, *Proc. Natl. Acad. Sci. U S A* **2019**, *116*, 24303–24309.

[9] A. Kumar, Y. Kubota, M. Chernov, H. Kasuya, *Med. Hypotheses* **2020**, *144*, 109848.

[10 I. Wessels, B. Rolles, L. Rink, *Front. Immunol.* **2020**, *11*, 1–11.

[11] A. Pal, R. Squitti, M. Picozza, A. Pawar, M. Rongioletti, A. K. Dutta, S. Sahoo, K. Goswami, P. Sharma, R. Prasad, *Biol. Trace. Elem. Res.* **2020**, *199*, 2882-2892.

[12] A. V. Skalny, L. Rink, O. P. Ajsuvakova, M. Aschner, V. A. Gritsenko, S. I. Alekseenko, A. A. Svistunov, D. Petrakis, D. A. Spandidos, J. Aaseth, A. Tsatsakis, A. A. Tinkov, *Int. J. Mol. Med.* **2020**, *46*, 17–26.

[13] P. G. de Almeida Brasiel, *Clin. Nutr. ESPEN* **2020**, *38*, 65–66.

[14] M. M. Black, *Am. J. Clin. Nutr.* **1998**, *68*, 464S-469S.

[15] M. Hambidge, *J. Nutr.* **2000**, *130*, 1344–1349.

[16] H. Haase, E. Mocchegiani, L. Rink, *Biogerontology* **2006**, *7*, 421–428.

[17] K. H. Brown, S. E. Wuehler, J. M. Peerson, *Food Nutr. Bull.* **2001**, *22*, 113–125.

[18] R. E. Black, *J. Nutr.* **2003**, *3*, 1485–1489.

[19] J. Y. Koh, S. W. Suh, B. J. Gwag, Y. Y. He, C. Y. Hsu, D. W. Choi, *Science* **1996**, *272*, 1013–1016.

[20] A. I. Bush, W. H. Pettingell, G. Multhaup, M. D. Paradis, J. P. Vonsattel, J. F. Gusella, K. Beyreuther, C. L. Masters, R. E. Tanzi, *Science* **1994**, *265*, 1464–1467.

[21] G. Genchi, M. S. Sinicropi, G. Lauria, A. Carocci, A. Catalano, *Int. J. Environ. Res. Public Health* **2020**, *17*, 3782.

[22] Y. Huang, C. He, C. Shen, J. Guo, S. Mubeen, J. Yuan, Z. Yang, *Food Funct.* **2017**, *8*, 1373–1401.

[23] J. Liu, W. Qu, M. B. Kadiiska, *Toxicol. Appl. Pharmacol.* **2009**, *238*, 209–214.

[24] A. Rani, A. Kumar, A. Lal, M. Pant, *Int. J. Environ. Health Res.* **2014**, *24*, 378–399.

[25] J. M. Moulis, F. Thévenod, *BioMetals* **2010**, *23*, 763–768.

[26] B. Wang, Y. Du, *Oxid. Med. Cell Longev.* **2013**, *2013*, 898034.

[27] G. Notarachille, F. Arnesano, V. Calò, D. Meleleo, *BioMetals* **2014**, *27*, 371–388.

[28] B. Wang, Y. Du, *Oxid. Med. Cell Longev.* **2013**, *2013*,12.

[29] A. Minami, A. Takeda, D. Nishibaba, S. Takefuta, N. Oku, *Brain Res.* **2001**, *894*, 336–339.

[30] M. K. Viaene, R. Masschelein, J. Leenders, L. J. V. C. Swerts, M. de Groof, H. A. Roels, *Occup. Environ. Med.* **2000**, *57*, 19–27.

[31] L. Järup, *Nephrol. Dial. Transplant.* **2002**, *17*, 35–39.

[32] Y. Yue, Q. Dong, Y. Zhang, Y. Sun, Y. Gong, *Anal. Methods* **2015**, *7*, 5661–5666.

[33] M. Formica, G. Ambrosi, V. Fusi, L. Giorgi, M. Arca, A. Garau, A. Pintus, V. Lippolis, *New J. Chem.* **2018**, *42*, 7869–7883.

[34] C. Lu, Z. Xu, J. Cui, R. Zhang, X. Qian, *J. Org. Chem.* **2007**, *72*, 3554–3557.

[35] S. B. Roy, J. Mondal, A. R. Khuda-Bukhsh, K. K. Rajak, *New J. Chem.* **2016**, *40*, 9593–9608.

[36] N. Roy, S. Nath, A. Dutta, P. Mondal, P. C. Paul, T. S. Singh, *RSC Adv.* **2016**, *6*, 63837–63847.

[37] M. Sohrabi, M. Amirnasr, S. Meghdadi, M. Lutz, M. Bikhof Torbati, H. Farrokhpour, *New J. Chem.* **2018**, *42*, 12595–12606.

[38] Y. Tang, Y. Huang, L. Lu, C. Wang, T. Sun, J. Zhu, G. Zhu, J. Pan, Y. Jin, A. Liu, M. Wang, *Tetrahedron Lett.* **2018**, *59*, 3916–3922.

[39] H. Liu, Y. Tan, Q. Dai, H. Liang, J. Song, J. Qu, W. Y. Wong, *Dyes Pigm.* **2018**, *158*, 312–318.

[40] A. Gogoi, G. Das, *RSC Adv.* **2014**, *4*, 55689–55695.

[41] N. Behera, V. Manivannan, *ChemistrySelect* **2016**, *1*, 4016–4023.

[42] N. Behera, V. Manivannan, *J. Photochem. Photobiol. A Chem.* **2018**, *353*, 77–85.

[43] S. Mahata, G. Janani, B. B. Mandal, V. Manivannan, *J. Photochem. Photobiol. A Chem.* **2021**, *417*, 113340.

[44] S. Mahata, S. Kumar, S. Dey, B. B. Mandal, V. Manivannan, *Inorganica Chim. Acta* **2022**, *535*, 120876.

[45] A. Bhattacharya, S. Mahata, A. Bandyopadhyay, B. B. Mandal, V. Manivannan, *Luminescence* **2022**, 1–9.

[46] A. J. Boydston, C. S. Pecinovsky, S. T. Chao, C. W. Bielawski, *J. Am. Chem Soc.* **2007**, *129*, 14550–14551.

[47] X. Yin, Y. Song, Y. Wang, L. Zhang, Q. Li, *Sci. China Chem.* **2014**, *57*, 135–140.

[48] Z. Guo, N. R. Song, J. H. Moon, M. Kim, E. J. Jun, J. Choi, J. Y. Lee, C. W. Bielawski, J. L. Sessler, J. Yoon, *J. Am. Chem. Soc.* **2012**, *134*, 17846–17849.

[49] J. Andeme Edzang, Z. Chen, H. Audi, G. Canard, O. Siri, *Org. Lett.* **2016**, *18*, 5340–5343.

[50] S. S. Lehrer, G. D. Fasman, *Biochem. Biophys. Res. Commun.* **1966**, *23*, 133–138.

[51] J. Hatai, S. Pal, G. P. Jose, T. Sengupta, S. Bandyopadhyay, *RSC Adv.* **2012**, *2*, 7033–7036.

[52] S. Saha, A. Ghosh, P. Mahato, S. Mishra, S. K. Mishra, E. Suresh, S. Das, A. Das, *Org. Lett.* **2010**, *12*, 3406–3409.

[53] M. Paul, S. Basu, A. Chattopadhyay, *Langmuir* **2020**, *36*, 754–759.

[54] D. Bano, V. Kumar, V. K. Singh, S. H. Hasan, *New J. Chem.* **2018**, *42*, 5814–5821.

[55] G. A. Crosby, J. N. Demas, *J. Phys. Chem.* **1971**, *75*, 991–1024.

[56] H. Güsten, R. Meisner, *J. Photochem.* **1983**, *21*, 53–60.

Appendix

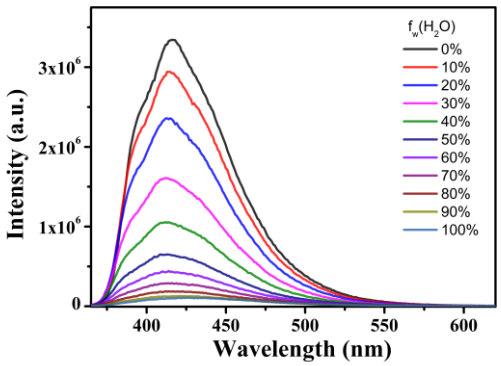

Figure A1: ACQ study of **L2H₂** in different percentage of water in DMSO

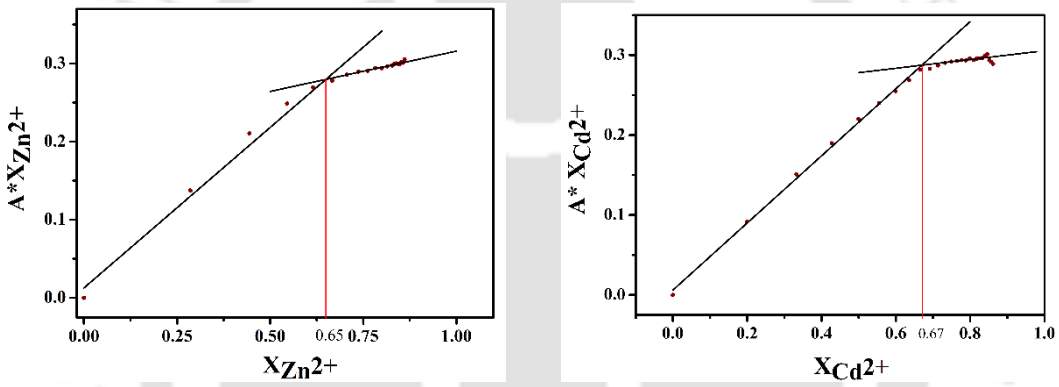

Figure A2. Job's plot analysis of continuous variation for **(a)** Zn^{2+} and **(b)** Cd^{2+} ions with **L2H₂**

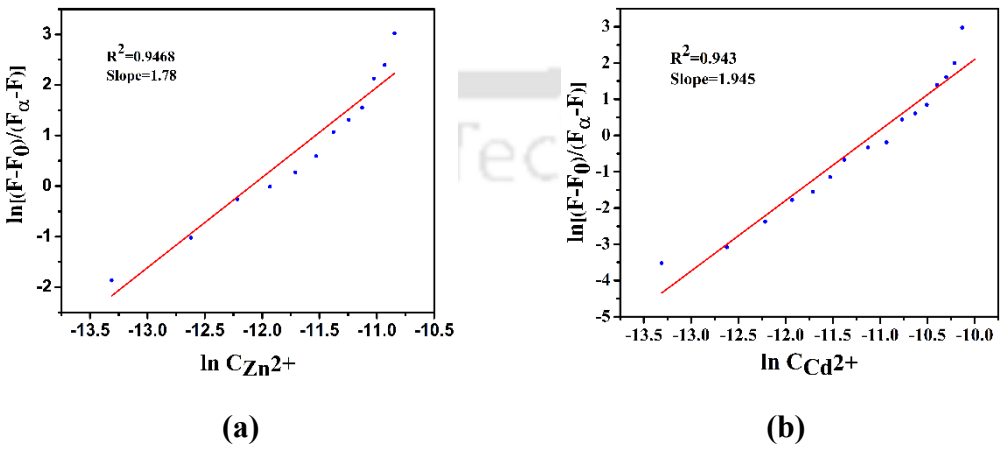

Figure A3. Lehrer and Chipman plot from the data obtained from fluorescence titrations in DMSO/Water(1:1, *v/v*) for (a) Zn^{2+} and (b) Cd^{2+} ions.

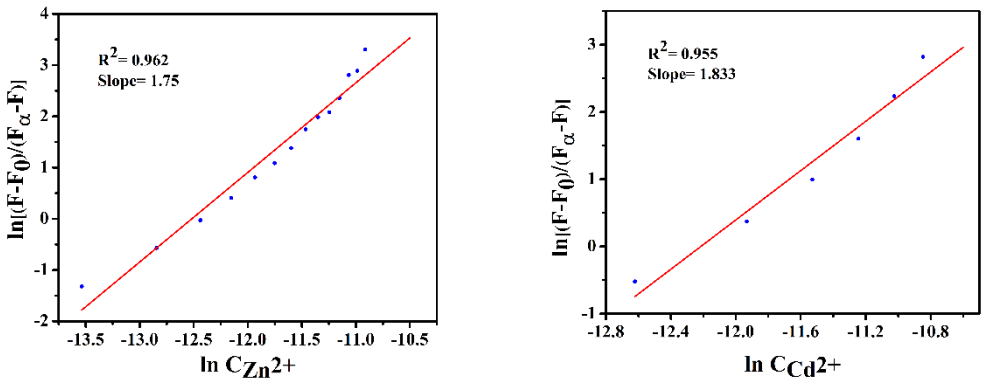

(a) **(b)**

Figure A4. Lehrer and Chipman plot from the data obtained from fluorescence titrations in water for **(a)** Zn^{2+} and **(b)** Cd^{2+} ions.

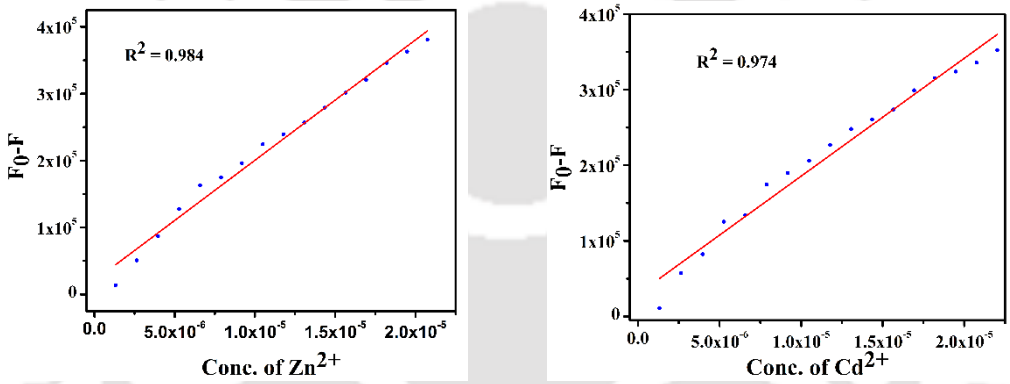

(a) **(b)**

Figure A5: Calibration plot for limit of detection from fluorescence titration data for **(a)** Zn^{2+} and **(b)** Cd^{2+} in DMSO/HEPES buffer (1:1, pH=7.34, rt, *v*/*v*)

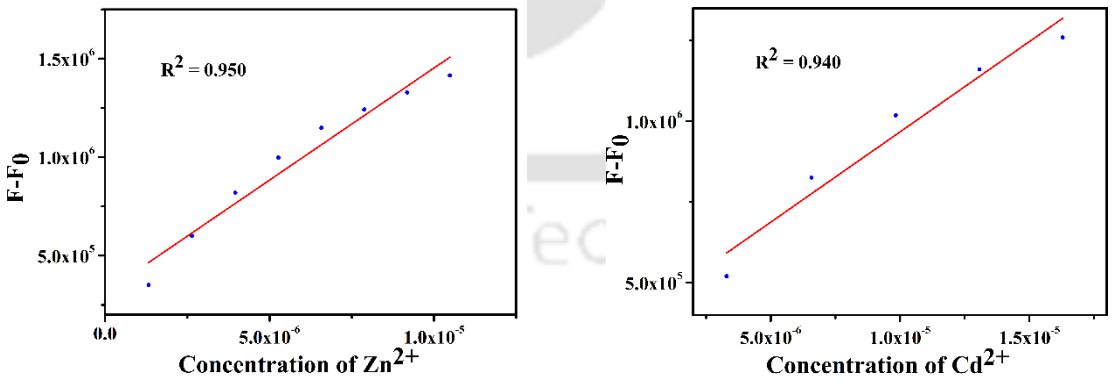

Figure A6: Calibration plot for limit of detection from fluorescence titration data for **(a)** Zn^{2+} and **(b)** Cd^{2+} in water.

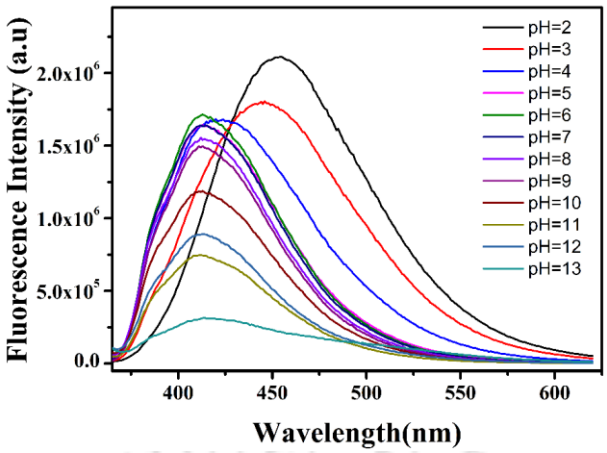

Figure A7. Effect of pH on the emission spectra of Free **L2H₂**.

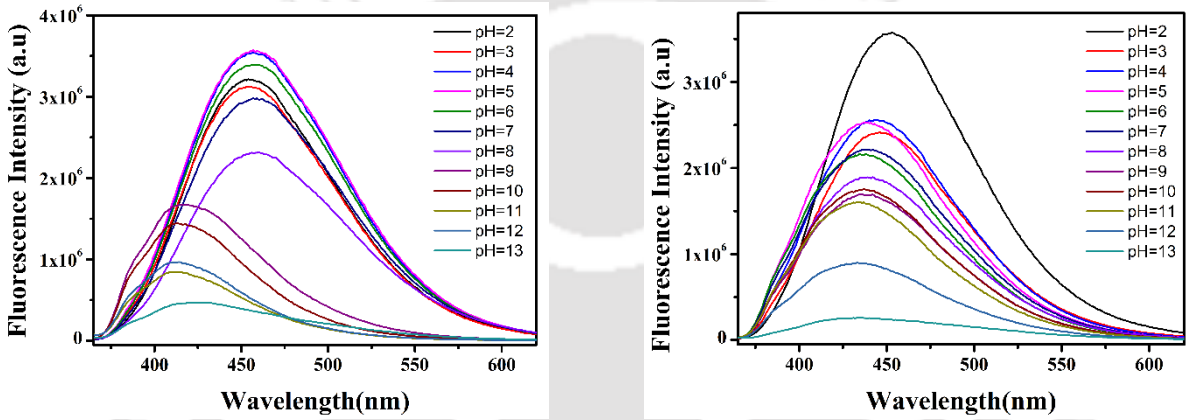

Figure A8. Effect of pH on the emission spectra of (a) **L2H₂** with Zn^{2+} and (b) **L2H₂** with Cd^{2+} ions.

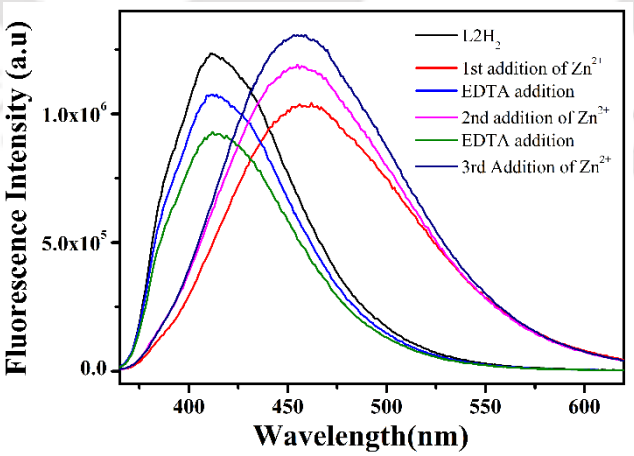

Figure A9. Reversibility test for Zn^{2+} ions

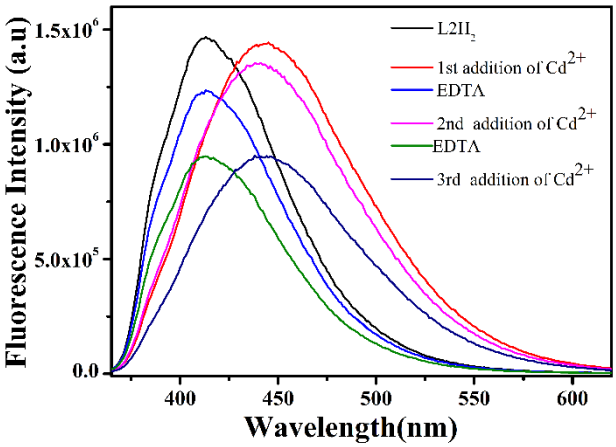

Figure A10. Reversibility test for Cd^{2+} ions.

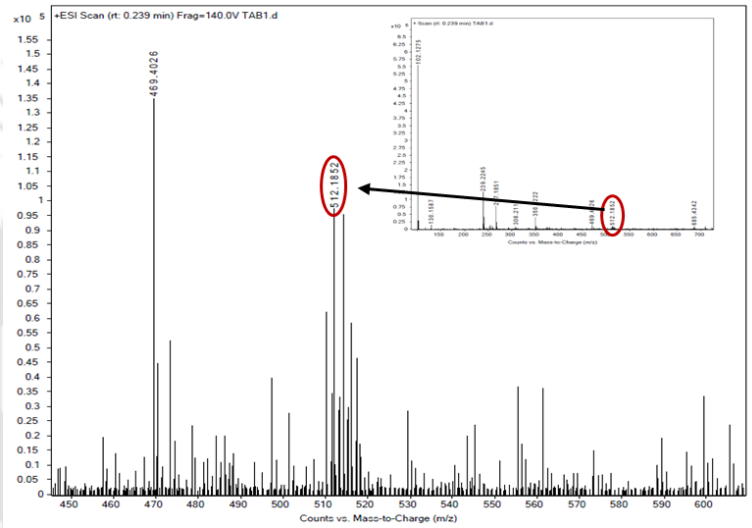

Figure A11. Mass spectrum of **L2H₂** with $ZnCl_2$ in acetonitrile (full range is in inset).

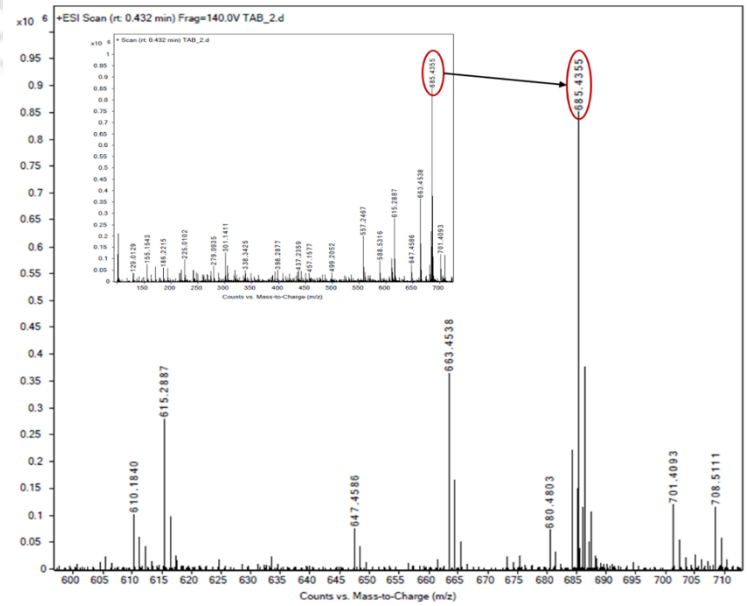

Figure A12. Mass spectrum of **L2H₂** with $CdCl_2$ in acetonitrile (full range is in inset).

Table A1: Some other probes

Sl No.	Probes	Metal ions	Limit of detection (M^{-1})	Solvent	Ref
1	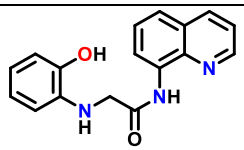	Zn^{2+}	0.256 µM	CH_3OH-TRIS HCl Buffer (4:1)	[1]
2	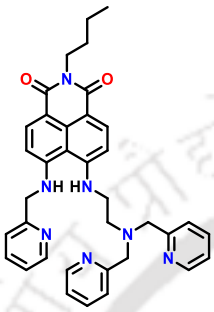	Zn^{2+} and Cd^{2+}	0.1 µM (both)	1:9, *v/v*, 50 mM HEPES buffer, pH =7.2	[2]
3	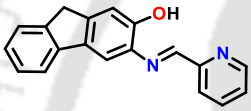	Zn^{2+} and Cd^{2+}	0.61 µM (Zn^{2+}) & 0.53 (Cd^{2+})	CH_3CN:H_2O (8 : 2, *v/v*, 10 mM HEPES) at pH 7.4	[3]
4	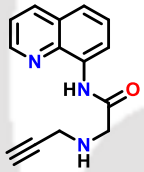	Zn^{2+} and Cd^{2}	0.063 µM(Zn^{2+}) & 0.055 µM(Cd^{2+})	CH_3CN/H_2O (95/5, *v/v*, 10mM HEPES, pH 7.2).	[4]
5	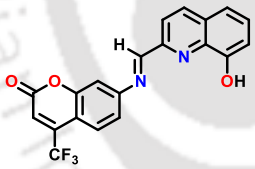	Fe^{3+}(Colorimetrically) Zn^{2+} and Cu^{2+}	--	CH_3OH/H_2O (40 : 60, *v/v*) solution	[5]
6	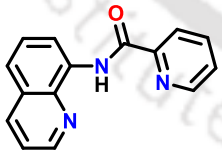	Zn^{2+}(Fluorimetrically) & Co^{2+}(Colorimetrically)	0.7 µM(Zn^{2+}) & 2.2 µM	CH_3CN	[6]
7	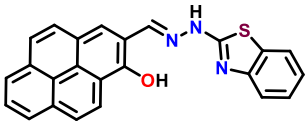	Zn^{2+}	0.2 µM	EtOH-HEPES (65:35, *v/v*, pH = 7.20),	[7]
8	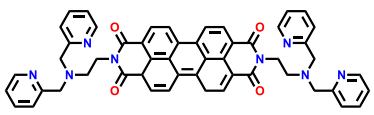	Zn^{2+} and Cd^{2}	32 nM (Zn^{2+}) and 48 nM (Cd^{2+})	CH_3CN–HEPES buffer (1/1, *v/v*, HEPES: 100 mM).	[8]

Table A2: Optimised structures

$L2H_2$	1	2
	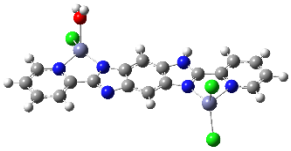	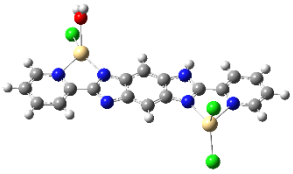

Table A3. Frontier MOs of **1** and **2**

	1	2
LUMO+1	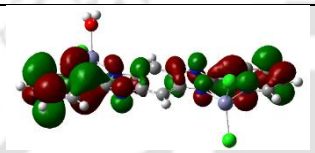 **E = -2.4454 eV**	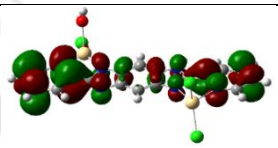 **E = -2.5192 eV**
LUMO	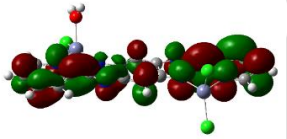 **E = -2.9676 eV**	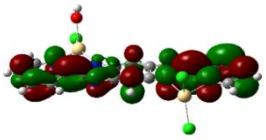 **E = -3.0071 eV**
HOMO	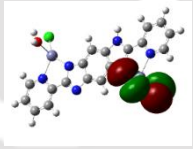 **E = -6.0520 eV**	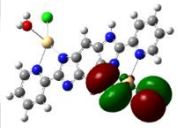 **E = -6.0496 eV**
HOMO-1	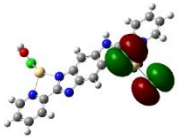 **E = -6.1269 eV**	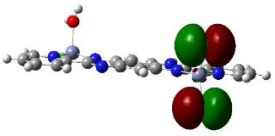 **E = - 6.0899 eV**
HOMO-2	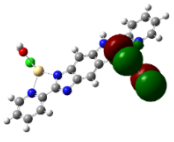 **E = -6.2358 eV**	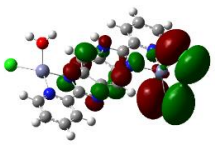 **E = - 6.1636 eV**

HOMO-3	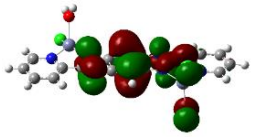	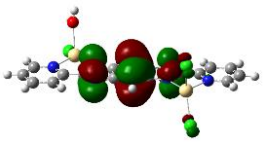
	E = -6.2099 eV	**E = - 6.2526 eV**
HOMO-4	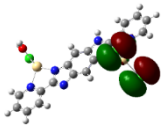	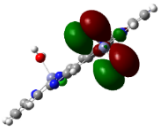
	E = -6.3258 eV	**E = - 6.2689 eV**
HOMO-5	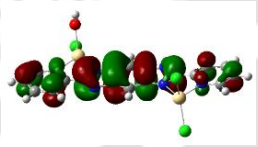	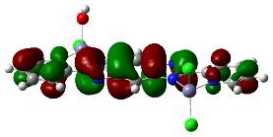
	E = -6.4774 eV	**E = -6.5144 eV**

Chapter 4

Colorimetric detection of Pd^{2+} and Ni^{2+} ions using a probe having benzo[*d*]imidazo[2,1-*b*]thiazole and pyrene rings: application in detection of Pd^{2+} ion in anti-hypertensive drugs*

Abstract:

Pd-complexes are widely used in the pharmaceutical industry to synthesize APIs and drug molecules. It is imperative to detect even trace amounts of Pd impurities in them. A probe *N*'-(pyren-1-ylmethylene)benzo[*d*]imidazo[2,1-*b*]thiazole-2-carbohydrazide (**L3H**) having benzo[*d*]imidazo[2,1-*b*]thiazole and pyrene rings has been synthesized. **L3H** was found to exhibit a change from colourless to yellowish green–in presence of Pd^{2+} and Ni^{2+} ions. This colorimetric "*turn on*" response has also been observed with Pd^{2+} ions in the presence of "sartan" drugs, namely telmisartan, valsartan, irbesartan, olmesartan medoxomil and losartan potassium. The limit of detection ranged from 46.1 to 93.9 nM (4.9 to 6.0 ppb) for $PdCl_2$ and 10.6 to 19.6 nM (1.1 to 2.1 ppb) for $Pd(PPh_3)_2Cl_2$ and these are lower than the limit suggested by the EMA. The LOD values of Ni^{2+} ion was 9.301 nM which is also lower than the WHO guideline value. This probe showed a remarkable ability to recover Pd^{2+} ions from the spiked solution of drug samples. The probe formed stable 1:1 complexes with both the metal ions. Binding constant values of Pd-**L3** complex increased in the presence of drug molecules, thereby indicating the absence of interference. The pH tolerance of the probe was found to be in the range of 3-11 (for Ni^{2+}) and 2-11 (for Pd^{2+}). DFT/TDDFT studies performed on **L3H**, [Pd(**L3**)(CH_3CN)Cl] and [Ni(**L3H**)(H_2O)(CH_3CN)Cl_2] in CPCM continuum solvation model in CH_3CN, showed good correlation between calculated UV-Vis and experimental spectra.

*Manuscript under revision

4.1 Introduction:

Pd is a rare metal with a silvery shiny appearance discovered by William Hyde Wollaston in 1803 in South African crude Platinum ore[1]. Since then, Pd has been used for several purposes, such as catalytic converters in automobiles and industries, components of alloys for dental casting, catalysts for industrial production of various chemicals and API (Active Pharmaceutical Ingredients) manufacturing. Besides that, due to its high adsorptive ability for hydrogen gas, Pd is often used to purify and activate H_2 gas. In the last few decades, Pd-complexes have become the backbone of organic synthesis for their fantastic catalytic activity in several organic reactions such as alkylation, arylation, cyclization, hydrogenation, oxidation, isomerization, cross-coupling, cascade, radical reactions[2] etc. The coupling reactions such as Heck[3,4] , Suzuki-Miyura[5], Kumada[6], Negishi[7,8], Stille[9] Sonogashira[10,11], Buchwald[12] *etc* primarily use Pd complexes as catalysts. Although Pd metal is practically non-toxic, its water-soluble chlorides have toxic effects on living beings. The LD_{50} value (in rats) of $PdCl_2$ solution ranges from 3 mg/kg to 200 mg/kg depending on the route of exposure (oral, intravenous or inhalation)[13] which puts the metal salt in high to moderately toxic category[14].

On the other hand, $Ni^{2+,}$ which belongs to the same group (Group 10) in the periodic table, has several applications as it is an essential trace element in biosynthesis and metabolism[15]. Nickel is found in many metalloenzymes[16–18] such as glyoxalase I, acireductone dioxygenase, urease, superoxide dismutase, [NiFe]-hydrogenase, carbon monoxide dehydrogenase and acetyl-coenzyme A synthase/decarbonylase which are responsible for maintaining different biological processes in living organisms. Ni-metalloenzymes are vital in maintaining the carbon cycle[19] on Earth. However, over-accumulation of Ni may lead to several adverse effects on humans and other species of plants and animals. Ni is a potentially toxic heavy metal that can affect multiple organs in living beings[20], and it can show its toxicity through oxidative stress pathways. Excessive accumulation of Ni^{2+} in plants may lead to deficiencies[21] of other metal ions as it can replace other essential minerals by forming chelate complexes, thereby reducing germination, plant growth, induction of chlorosis and wilting of leaves.

As Pd catalysts are often used in large-scale production of the API (Active Pharmaceutical Ingredients) and drug molecules, residual Pd salts may be present as impurities. Colorimetric and fluorometric methods are the cheapest methods for detecting any analyte in a mixture. Allyl Pittsburgh Green Ether is a commercially available molecule used in the testing kit to detect

impurities in API products[22]. Hypertension is one of the leading causes of mortality[23,24] in developing nations. For this reason, anti-hypertensive drug manufacturing is on the rise, and Pd-catalysts are used to synthesize different genres of drug molecules[25–27]. Among the anti-hypertensive medications, Angiotensin II Receptor Antagonists/Blockers (ARB) are commonly used, and the Sartan group of drugs are the ARBs majorly used for those purposes[28]. Many of these Sartan drugs are synthesized through Pd-Catalyst mediated synthetic pathways, as reported by many groups[29–39]. According to the Guideline for Elemental Impurity Q3D of the International Conference on Harmonisation Principles (ICH) published by the European Medicines Agency (EMA), the permitted daily exposure (PDE) of elemental Pd is 100 µg/day(oral) and maximum permitted concentration is10 µg/g or 10 ppm in drug substances[40]. So, it is necessary to devise new methods and probes for detecting trace amounts of Pd in drug substances, especially those synthesized by Pd-Catalyst mediated synthetic pathways. Many groups have reported many probes capable of detecting Pd^{2+} by comprehensible colorimetric and fluorometric responses[41,42]. There are also some reports of the detection of Pd^{2+} in aspirin, a well-known analgesic drug molecule[43,44]. However, little effort has been made to develop a probe to detect Pd^{2+} in anti-hypertensive drugs where Pd-catalysts are typically used in the synthesis pathway. We have previously reported a probe, 3-(1-isoquinolinyl)imidazo[5, 1-*a*]isoquinoline, for detecting Pd^{2+} ion in MeOH/HEPES buffer medium[45]. The probes reported for the selective detection of Pd^{2+} ion are listed in Table S1 [46–55].

Herein, the synthesis of a probe having benzo[*d*]imidazo[2,1-*b*]thiazole and pyrene rings and its potential as a sensor of Pd^{2+} and Ni^{2+} ions have been reported. In addition, in the presence of ARBs (Angiotensin Receptor Blockers) such as Telmisartan, Valsartan, Irbesartan, Olmesartan Medoxomil, and Losartan Potassium, the probe's potential application in the detection of Pd^{2+} ion has also been reported.

4.2 Experimental Section:

All the information regarding materials and methods for the preparation of samples, UV-Vis titration experiments, spectroscopic data analysis and computational methods are described in detail in supplementary material unless otherwise specified. Compound **1** and **2** were synthesized by a reported procedure[56–58].

4.2.1 Synthesis

benzo[*d*]imidazo[2,1-*b*]thiazole-2-carbohydrazide was synthesized by reported multistep procedures[56–58].

N'-(pyren-1-ylmethylene)benzo[d]imidazo[2,1-b]thiazole-2-carbohydrazide ***(L3H)***

Compound **2** (0.232 g, 1 mmol) and 1-pyrenecarboxaldehyde (0.230 g, 1 mmol) were dissolved in absolute ethanol (20 mL) and heated at reflux for 12 h (Scheme 1). The solution was allowed to cool to room temperature and a pale yellowish-white precipitate of **L3H** deposited

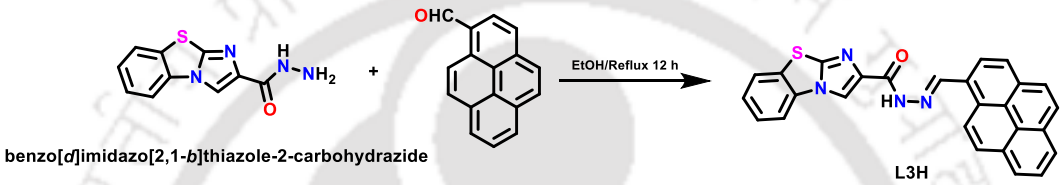

Scheme 1: Synthesis of **L3H**.

was filtered, washed with cold ethanol and dried under vacuum. Yield: 0.270 g (76 %). 600 MHz ^{1}H NMR (DMSO-d_6, δ (J, Hz)): 12.05 (1H, s), 9.75 (1H, s), 9.12 (1H, s), 8.80 (1H, d, *J* = 9.4 Hz), 8.63 (1H, d, *J* = 8.1 Hz), 8.38 (4H, d, *J* = 9.5 Hz), 8.29 - 8.21 (3H, m), 8.15 – 8.09 (2H, m), 7.62 (1H, t, *J* = 8.2 Hz), 7.51 (1H, t, *J* = 8.2 Hz). 150 MHz ^{13}C NMR (DMSO-d_6, δ) 157.8, 146.7, 146.3, 140.6, 131.9, 131.5, 130.9, 130.2, 129.6, 128.8, 128.7, 128.4, 127.5, 127.3, 126.9, 126.6, 126.1, 125.8, 125.3, 125.2, 124.5, 124.2, 123.8, 122.4, 117.0, 114.4. HRMS (ESI +ve) *m/z*: Calcd for $C_{27}H_{17}N_4OS^+$ $[M + H]^+$ 445.1118, Found 445.1119. Calcd. for $C_{27}H_{16}N_4NaOS^+$ $[M + Na]^+$ 467.0938, Found 467.0939. Selected FT IR peaks (ATR mode, cm^{-1}): 3311 (m, ν_{N-H}), 3120 (s, ν_{C-H}), 3042 (w, ν_{C-H}), 1692 (s, $\nu_{C=O}$), 1595 (s, $\nu_{C=N}$).

4.2.2 Preparation of Drug solutions and estimation

The drug compounds telmisartan, valsartan, olmesartan medoxomil, losartan potassium and irbesartan were purchased from commercial sources and used without further purifications. All the drug solutions were prepared by dissolving 10 mg of the drug in 1 mL of HPLC grade DMSO. Calibration plots (absorbance *vs.* conc. of Pd^{2+} ion) were obtained from the UV-Vis titration data obtained in the presence of 0.4 mg of each drug. The recovery test was done by spiking the drug solutions with a predetermined amount of separate solutions of $PdCl_2$, $Pd(OAc)_2$ and $Pd(PPh_3)_2Cl_2$ *i.e.*, 100 µL, 150 µL and 200 µL, followed by the addition of 1mM

L3H solution. From the subsequent absorbance values, the concentration of $PdCl_2$ was determined in the corresponding spiked solutions.

4.3. Results and Discussions

4.3.1 UV-Visible Spectra

The probe **L3H** in CH_3CN/HEPES buffer (2mM, pH = 7.34, 4:1, *v/v*) showed a peak at 372 nm along with three other peaks at 291, 303 and 400 nm. **L3H** has two extended π-conjugated ring systems separated by a hydrazide spacer. On one side, the π-electrons of benzo[*d*]imidazo[2,1-*b*]thiazole ring may be involved in conjugation with the carbonyl group which in turn is in conjugation with the lone pair of electrons on nitrogen of the hydrazide group. Conversely, the –C=N– group is in conjugation with the pyrene ring. The peaks at 372 and 400 nm may be due to the π-π* transitions happening in those two π conjugated ring systems. Upon coordination with the metal ions there was diminishing of peak intensity at 372 nm and probably the N-atom of benzo[*d*]imidazo[2,1-*b*]thiazole ring has involved (*vide supra*) in coordination. But the intensity at 400 nm was not affected by coordination of the metal ions indicating that 400 nm peak may originate from the pyrene ring. UV-Vis spectra of **L3H** were recorded in the presence of 8 equivalents of aqueous solutions of chloride salts of different metal ions, *viz*., Li^+, K^+, Na^+, Mg^{2+}, Ca^{2+}, Al^{3+}, Cr^{3+}, Mn^{2+}, Fe^{3+}, Co^{2+}, Ni^{2+}, Cu^{2+}, Zn^{2+}, Pd^{2+}, Cd^{2+}, Hg^{2+}, Pb^{2+} and Ag^+. Comprehensible changes were observed only in the cases of Ni(II) and Pd(II), wherein the intensity of the 372 nm peak got diminished and shifted to 382 nm along with the peak at 400 nm getting obscured. While titrating with DMSO solution of $PdCl_2$ solution (up to 8 equivalents) in CH_3CN/HEPES buffer (2mM, pH = 7.34, 4:1, *v/v*), **L3H** showed a broadening of absorption spectrum in the region of 424-500 nm and the colour of the solution changed from colourless to greenish yellow. However, 440 nm was used for all estimation purposes. Titration with aqueous $NiCl_2$ solution (up to 2 equivalents) in CH_3CN/HEPES buffer (2mM, pH = 7.34, 4:1, *v/v*) **L3H** showed a broadening of spectrum in the region of 414-480 nm range and 435 nm was considered for all the estimations likewise and a similar change in colour of the solution was observed. Among other metal ions, the spectra (i) remained unchanged for Li^+, K^+, Al^{3+}, Cr^{3+}, Mn^{2+} and Hg^{2+} ion, (ii) there were slight increments (10-38%) in intensity (at 372 nm) for Ag^+, Fe^{3+}, Co^{2+}, Cu^{2+}, Zn^{2+}, Cd^{2+} and Pb^{2+} ions and (iii) slight decrement (5-10%) in intensity (at 372 nm) for Na^+, Mg^{2+} and Ca^{2+} ions (Figure 2). There was no broadening observed in the range of 410-500 nm for all the metal ions mentioned above except for Pd^{2+}

and Ni^{2+}. Competitive analyses were done to understand the interference in sensing by other metal ions for both metal ions (Figure A5).

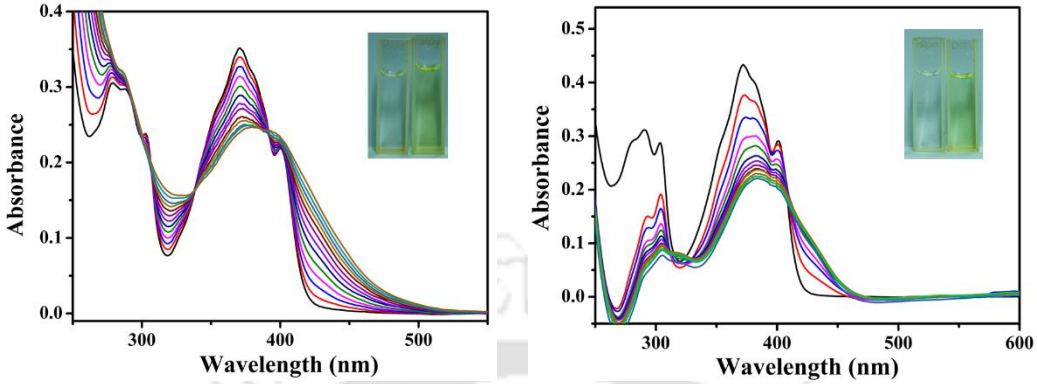

Figure 1: UV-Vis titration of **L3H** with Pd^{2+} (left) and Ni^{2+} (right) ions in CH_3CN/HEPES buffer (2mM, pH = 7.34, 4:1, *v/v*) (Change in colour of the solution is shown in the inset)

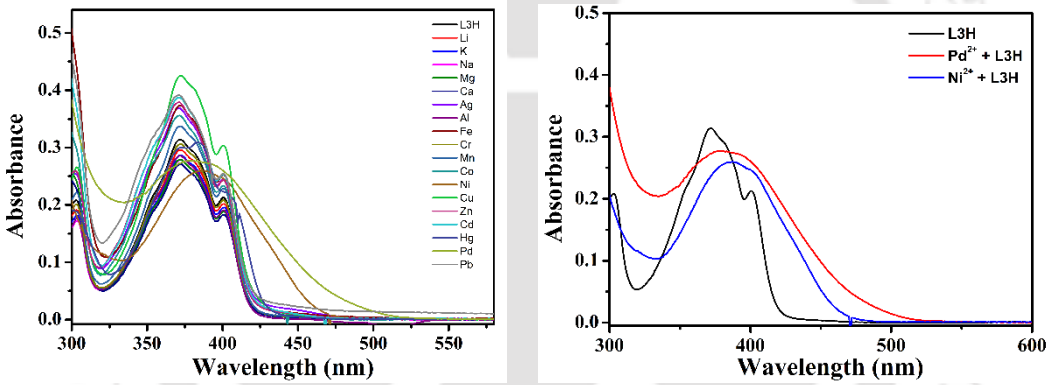

Figure 2: UV-Vis spectra of **L3H** in presence of (**a**) all other metal ions and (**b**) Pd^{2+} and Ni^{2+} ions.

The reason for the **L3H** to selectively binds these two metal ions may be due to soft-soft interaction between **L3H** and Pd^{2+} / Ni^{2+} ions. Interaction of **L3H** with anions were also analysed by employing (8 equivalents) sodium salts of $HCOO^-$, $S_2O_3^{2-}$, OH^-, SO_4^{2-}, NO_3^-, F^-, NO_2^-, CO_3^{2-}, CH_3COO^-, N_3^-, S^{2-}, AsO_3^-, CN^- and $H_2PO_4^-$ ions, wherein no change in absorption spectra was observed (Figure A6). With concentrated solutions of **L3H** and $NiCl_2$, a low intensity peaks at 964 nm was observed which may be of $d \rightarrow d$ transition in origin (Figure A7) and no other $d \rightarrow d$ transitions were observed as they might have been obscured by the allowed intra-ligand transitions. Thus in the presence of these anions, the remarkable selectivity of **L3H** towards Pd^{2+} and Ni^{2+} over other metal ions is established. The **L3H** was

found to be very weakly emissive and none of the metal ions described in this study exhibited any *turn on* response but with $PdCl_2$ and $NiCl_2$ emission intensity got diminished (Figure A8).

4.3.2 Detection of Pd^{2+} ion in presence of drug:

The concentration of Pd^{2+} was varied by gradual addition in the presence of the 0.4 mg of each of the drug compounds (Figure A9) and the **L3H** solution (30 µL) to establish the calibration plots. All the drug samples had their characteristic peaks in the 200-300 nm wavelength range, which did not interfere with the characteristic peaks of the **L3H**. The recovery test was done following the standard procedure of spiking a known amount of $PdCl_2$ solution and taking the absorbance value of the **L3H** mixed with the spiked solution. Then, from the calibration plot (Figures A10-A12), the concentration corresponding to the absorption value was determined. From the recovery percentage data (Table 1), it is understandable that the presence of the drug molecules does not interfere with the sensing of Pd^{2+} by the probe **L3H**.

Table 1: Recovery (%) in the presence of drugs[#].

Test	$[Pd^{2+}]$ added (µM)	$[Pd^{2+}]$ found (µM)	% Recovery	RSD
A+**1**	32.1	27.8	86.85	0.69
	63.1	56.2	89.08	0.37
A+**2**	31.5	23.6	74.70	0.95
	46.6	39.4	84.68	0.38
	61.2	56.2	91.95	0.64
A+**3**	31.5	34.1	108.08	0.45
	46.6	49.6	106.57	0.17
	61.2	61.3	100.16	0.45
A+**4**	31.5	30.2	95.64	2.77
	46.6	48.0	103.14	0.17
	61.2	63.6	104.01	0.33
A+**5**	31.5	27.3	86.51	1.03
	46.6	43.2	92.82	0.79
	61.2	54.3	88.77	0.51
B+**1**	31.5	23.3	73.99	3.68
	46.6	41.5	89.05	3.05
	61.2	47.6	77.82	2.95
B+**2**	31.5	36.9	116.94	3.67
	46.6	45.1	96.75	4.09
	61.2	60.7	99.30	4.26
B+**3**	31.5	29.2	92.48	5.40
	46.6	41.6	89.22	3.40

	61.2	53.9	88.05	3.08
	31.5	15.6	49.31	2.21
B+**4**	46.6	27.0	57.88	2.88
	61.2	54.2	88.61	2.67
	31.5	29.0	91.88	3.68
B+**5**	46.6	36.0	77.36	3.05
	61.2	44.3	72.42	2.95
	6.47	6.18	95.46	2.46
C+**1**	12.9	9.31	72.42	1.70
	25.4	21.5	84.71	1.94
	6.47	5.63	87.02	4.45
C+**2**	12.9	13.7	106.29	2.05
	25.4	27.6	108.56	1.92
	6.47	6.45	99.70	1.20
C+**3**	12.9	10.0	78.11	6.34
	25.4	19.5	76.89	2.00
	6.47	5.34	82.45	3.60
C+**4**	12.9	14.5	113.06	2.50
	25.4	25.4	99.83	1.83
	6.47	5.23	80.73	2.32
C+**5**	12.9	12.8	99.42	2.14
	25.4	25.3	99.70	1.52

[#] **A** = $Pd(OAc)_2$; **B** = $PdCl_2$; **C** = $Pd(PPh_3)_2Cl_2$. **1** = Telmisartan; **2** = Valsartan; **3** = Irbesartan; **4** = Olmesartan Medoxomil; **5** = Losartan Potassium.

4.3.3 Binding stoichiometry and limit of detection

The binding ratio was determined from the Job's plot by using the titration data obtained for λ = 440 nm (for Pd^{2+}) and λ = 435 nm (for Ni^{2+}) with **L3H** in CH_3CN/HEPES buffer (2mM, pH = 7.34, 4:1, *v/v*). In this Job's method of continuous variation, $PdCl_2$ and $NiCl_2$ solutions were gradually added to the solution of **L3H**. The corresponding absorbance values were recorded; in both cases, a 1:1 metal-to-ligand ratio was obtained (Figure A13). The binding constants for **L3H** were calculated from the Benesi-Hildebrand plots (Figure 3) and the values were obtained as 3.72×10^3 L mol^{-1} (for Pd^{2+})and 8.26×10^4 L mol^{-1} (for Ni^{2+}). These binding constants values indicate that ligand **L3H** coordinates more strongly with Ni^{2+} than Pd^{2+} ion. The 1:1 binding stoichiometry was also supported by the observed *m/z* values of 663.45 and 705.08 corresponding the composition [Pd(**L3**)(CH_3CN)Cl] + K^+ (Calcd. 663.95) and [Ni(**L3H**)(CH_3OH)((CH_3)$_2$SO)Cl_2] + Na^+ (Calcd 705.01) respectively, in the mass spectra (Figure A14 and A15).

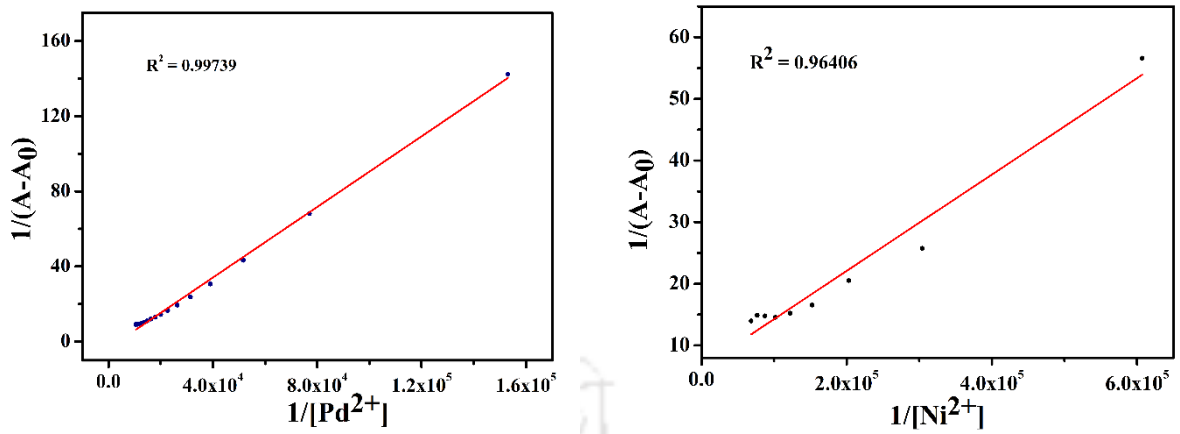

Figure 3: Benesi-Hildebrand plot for Pd^{2+} (left) and Ni^{2+} (right) ions.

Table 2: Binding constants (L mol^{-1}) for Pd^{2+} ion in the presence of drugs.

Drug	Binding Constant
None	3.72×10^3
Telmisartan	6.29×10^3
Valsartan	9.13×10^3
Irbesartan	8.43×10^3
Olmesartan Medoxomil	5.35×10^3
Losartan Potassium	5.03×10^3

Binding constants values for complex formation between **L3H** and Pd^{2+} ion, in the presence of the drug molecules, were obtained from the Benesi-Hildebrand plot (Figure A16). It has been found to show 35-145% increase in the binding constant (Table 2); hence, these drugs do not compete to interact with either **L3H** or Pd^{2+} ion, making the probe **L3H** practically useable to detect Pd^{2+} ion in the drug, as the stability of [Pd(**L3**)(CH_3CN)Cl] has not been hampered by these drug species.

The applicability of any probe for its practical use is significant, and the limit of detection (LOD) is one of the essential parameters. The LOD values were obtained following the standard procedure (LOD = 3σ/K) for each metal ion. LOD values were calculated to be remarkably low, and the values obtained were 12.44 nM (for $Pd(PPh_3)_2Cl_2$), 46.08 nM (for $PdCl_2$) and 9.30 nM (0.546 ppb) (for $NiCl_2$) (Figure 4). These values were lower than most of

the earlier probes reported (Table S1). As the probe **L3H** can detect the Pd^{2+} ions in the presence of the anti-hypertensive drugs, its LOD values are also calculated in their presence (Table 3)

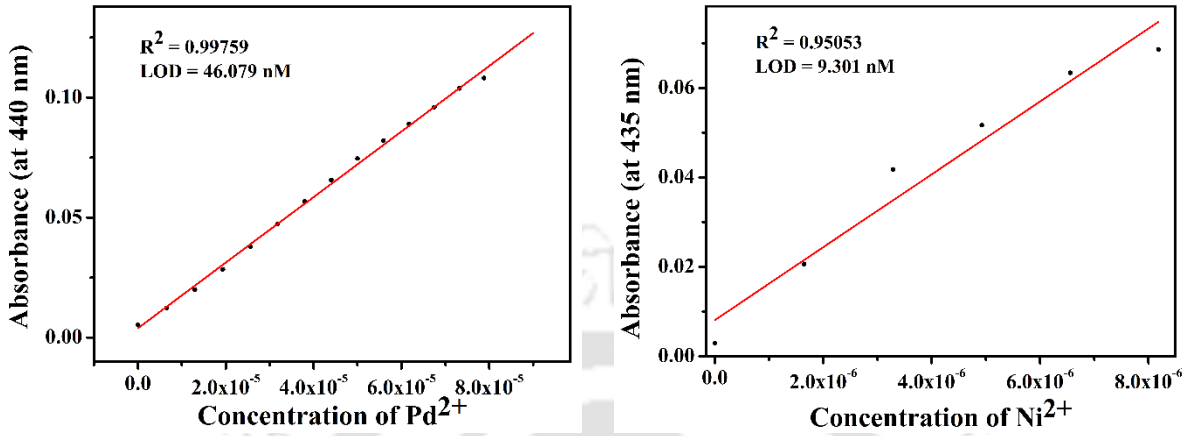

Figure 4: Calibration plot for determination of limit of detection by **L3H** for Pd^{2+} (left) and Ni^{2+} (right) ions.

Table 3: LOD values for **L3H** towards Pd^{2+} ion[#].

Test	nM	ppb	Test	nM	ppb
A	46.079	4.904	C	12.436	1.323
A + 1	81.047	8.625	C + 1	10.577	1.126
A + 2	61.611	6.557	C + 2	19.603	2.086
A + 3	80.429	8.56	C + 3	15.728	1.674
A + 4	57.388	6.107	C + 4	17.750	1.889
A + 5	93.900	9.993	C + 5	14.619	1.556

[#] **A** = $PdCl_2$; **C** = $Pd(PPh_3)_2Cl_2$.**1** = Telmisartan; **2** = Valsartan; **3** = Irbesartan; **4** = Olmesartan Medoxomil; **5** = Losartan Potassium.

The LOD values in the presence of drugs range from 6.107 ppb to 9.993 ppb, which is less than the PDE values prescribed in guidelines by ICH and EMA[40]. The prescribed LOD value for Ni^{2+} is 70µg/L (1.1926 µM) according to WHO guidelines. So, this probe **L3H** can be used to detect the presence of commonly used palladium compounds as impurities in the above-mentioned generic drugs as well as Ni^{2+} in drinking water.

4.3.4 Effect of pH

The tolerance level of the probe in the pH range of 1-11 was determined in similar solvent systems, where $PdCl_2$ solution was added to **L3H**. The probe **L3H** can detect Pd^{2+} ions in the

pH range of 3-11 as there is visible change as well as a comprehensible increase in absorbance value. Similar pattern was observed for the detection of Ni^{2+} ion as well and pH range was found to be 2-11. So, the selectivity of the probe is not deterred by variation in the pH of the solution and probe **L3H** can be used in a wide pH range (Figure 5).

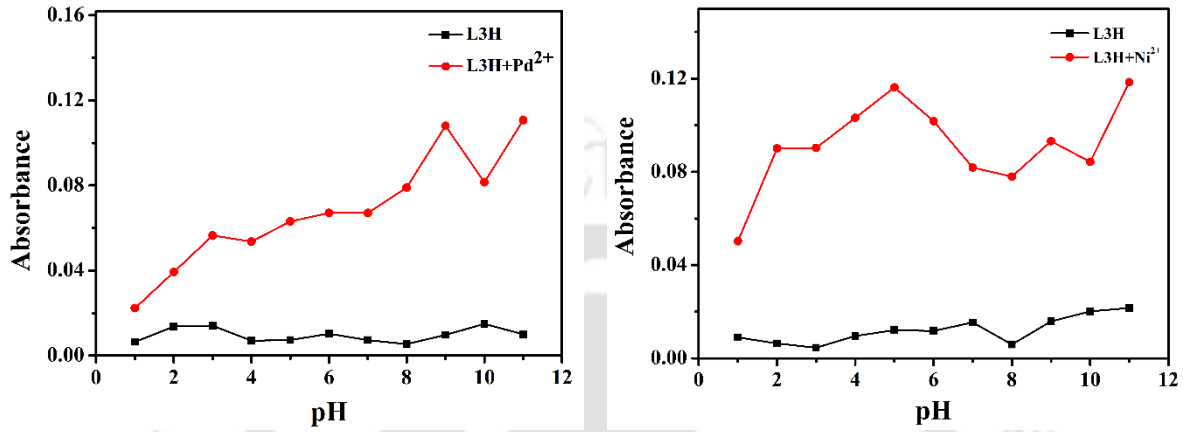

Figure 5: Effect of pH on sensing of Pd^{2+} (left) and Ni^{2+} (right) ions by **L3H**.

4.3.5 Response time

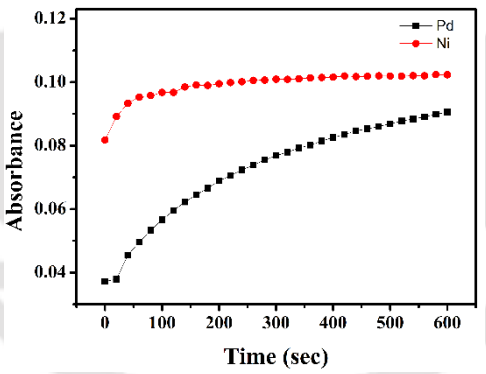

Figure 6 Kinetic profile for calculation of response time.

To measure the response time of **L3H** in detection of Pd^{2+} and Ni^{2+} a kinetics profile of 10 minutes was taken where the buffered solution of **L3H** was mixed with 200 µL of each of the metal chloride solutions. The response time were calculated to be 400 s (for Pd^{2+}) and 40 s (for Ni^{2+}) with longer time for Pd^{2+} ion was understandably due to involvement of 4d-orbitals and operation of associative type mechanism (Figure 6).

4.3.6 Theoretical studies

Optimization of molecular structures and the TD-DFT energy calculation of **L3H**, [Pd(**L3**)(CH_3CN)Cl] and [Ni(**L3H**)(H_2O)(CH_3CN)Cl_2] were done by Gaussian 16 program [59]. Both the calculations were performed at B3LYP level using 6-31+G(d,p) basis set for **L3H** and in LANL2DZ for complexes. All the calculations were done by incorporating acetonitrile as the solvent in the CPCM continuum solvation model. The theoretical electronic spectra were obtained with the help of Gaussview 06 software [60] by using the result of TD-DFT energy calculations. The ground state optimized structure of **L3H** showed that the pyrene ring is twisted with respect to the carbonic hydrazide linkage by an angle of 60°. The HOMO of **L3H** is a π orbital with the electron density concentrated mostly on the pyrene ring and the LUMO is of π^* and anti-bonding in nature with the lobes dominated over pyrene ring. At LUMO+1 level the electron density was observed to be delocalized on the benzo[*d*]imidazo[2,1-*b*]thiazole ring. Electrostatic Potential (ESP) map (Figure 7) showed that the electron density on the benzo[*d*]imidazo[2,1-*b*]thiazole ring was decreased due to the presence of electron-withdrawing carbonyl group, whereas the pyrene ring remain unaffected as there was no electron drift. The probe **L3H** can lose the hydrazide proton and thus can bind as the **L3**$^-$ anion. Since the mass spectrum fitted well with the formulations [Pd(**L3**)(CH_3CN)Cl] and [Ni(**L3H**)(H_2O)(CH_3CN)Cl_2], calculations were performed on these molecules. The **L3**$^-$ has linked through N and O atoms with Pd^{2+} center and **L3H** through N and N atoms with Ni^{2+} ion. Binding by **L3**$^-$ ion and **L3H** respectively with Pd(II) and Ni(II) was supported by the ESP map diagram, wherein accumulation of electron density can be seen on said donor sites. The UV-Vis spectra obtained from the theoretical calculation showed similar shift of absorption maximum as observed in the experimental spectra (Figure 8).

The energy corresponding to the transition $S_0 \rightarrow S_1$ in **L3H**, was calculated to be 3.2061 eV with oscillator frequency 0.7087, which involves promotion of an electron from HOMO to LUMO and to LUMO+1 levels. For [Pd(**L3**)(CH_3CN)Cl], the electronic transition involves HOMO-4, HOMO, LUMO and LUMO+1, with the excitation energy of $S_0 \rightarrow S_4$ transition was calculated to be 2.8127 eV and with an oscillator frequency of 0.4382. The HOMO-4 and LUMO were mainly of *d*-orbitals on Pd. Hence, there might be some *d-d* transition involved these two levels. At the same time, HOMO and LUMO+1 were mainly the π and π^* orbitals, respectively, on the pyrene ring.

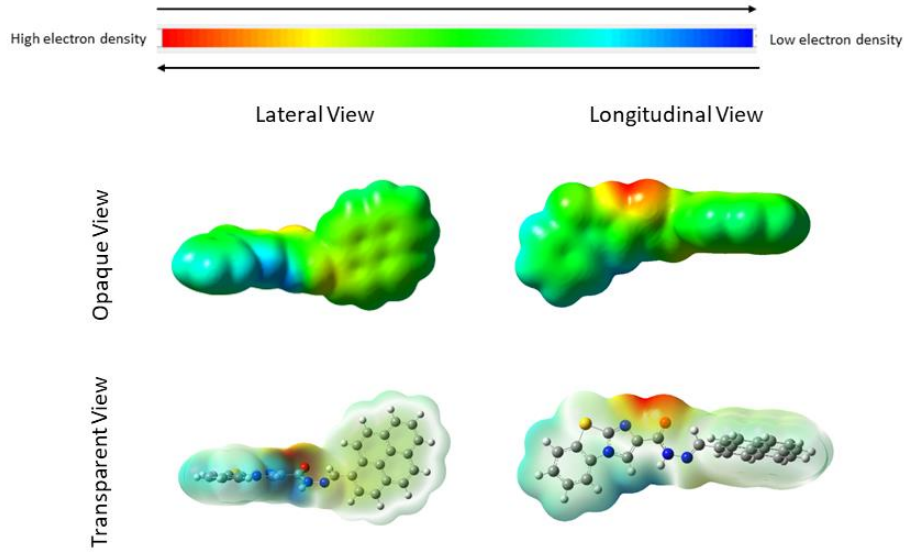

Figure 7: Molecular electrostatic potential map for **L3H**.

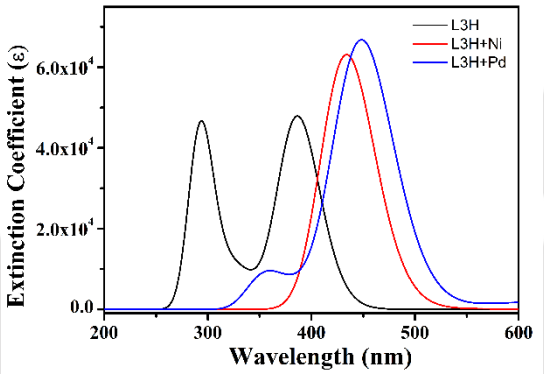

Figure 8: Theoretical UV-Vis spectra.

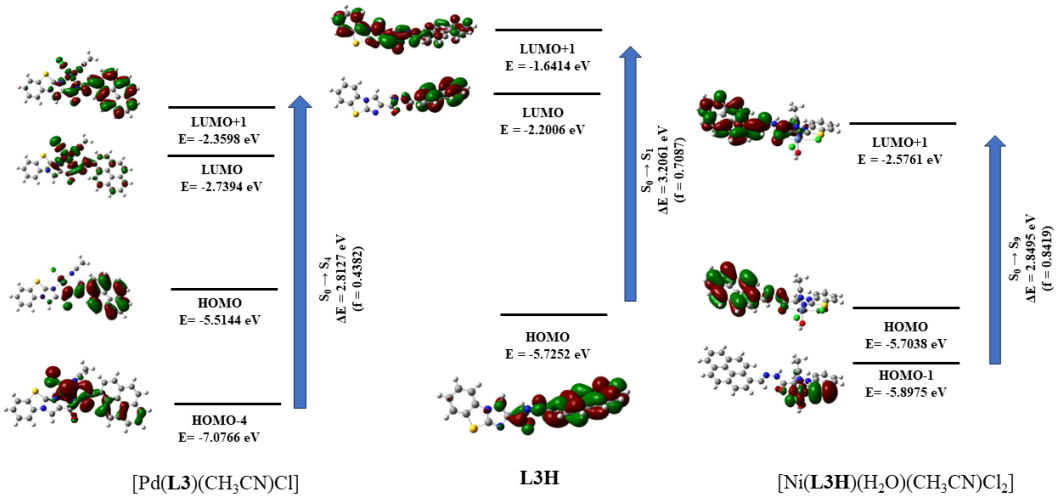

Figure 9: Ligand-based FMO and electronic transitions in acetonitrile.

On the other hand, the in case of [Ni(**L3H**)(H_2O)(CH_3CN)Cl_2] electronic transition $S_0 \rightarrow S_9$ (ΔE = 2.8495 eV, f = 0.8419) had the highest value of oscillator strength, involving HOMO-1, HOMO and LUMO+1 (Figure 9).

4.3.7 Mechanism of Sensing

TDDFT analysis in the solvent phase (acetonitrile) revealed that in both complexes the LUMO and LUMO+1 levels were stabilised to a greater extent and HOMO was stabilised minimally. Net result is the decrease in the excitation energy values due to coordination, implying a red shift in the λ_{max} value and indeed, such red-shift has been observed experimentally.

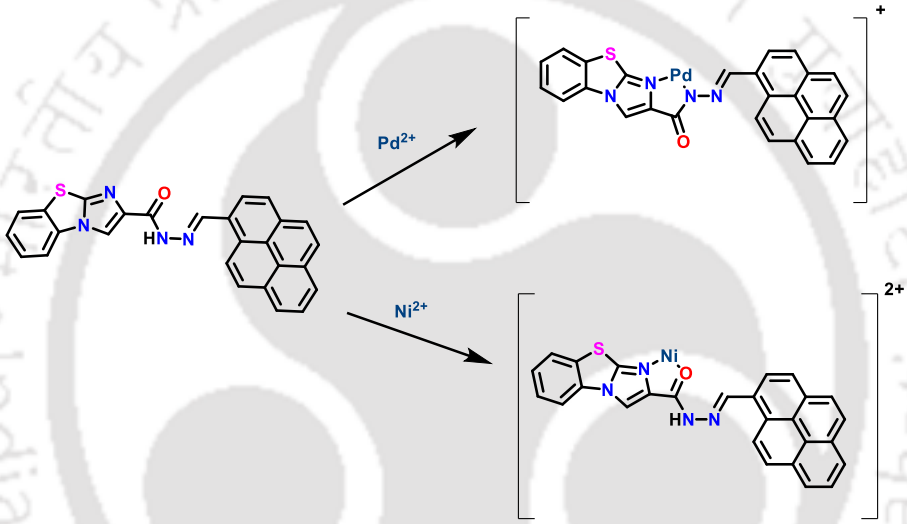

Figure 10: Proposed mechanism of complexation of **L3H** with Pd^{2+} and Ni^{2+} ions.

Theoretically obtained UV-Vis spectra shows the same pattern of shift as observed in experimental spectra (Figure 7). This chelation-induced red-shift may be due to pyrene ring attaining near co-planarity with benzo[*d*]imidazo[2,1-*b*]thiazole ring upon coordination with the metal ions. It is pertinent that the pyrene ring got twisted by 60° with respect to the benzo[*d*]imidazo[2,1-*b*]thiazole ring in **L3H**, and that hinders the delocalization of charge between the two π-conjugated ring systems. So, ICT was turned on upon coordination of the metal ions where the charge transfer would happen from electron rich pyrene ring to the benzo[*d*]imidazo[2,1-*b*]thiazole ring. The proposed complexes are shown in Figure 10 and the visuals of change in colour in Figure 11.

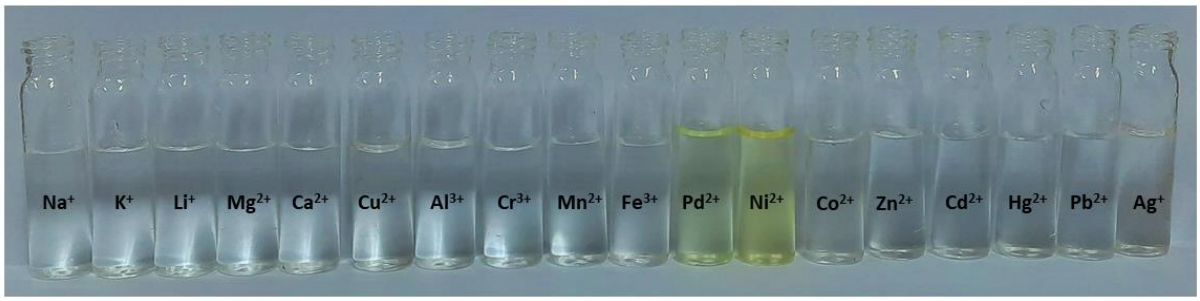

Figure 11: Colour comparison in the presence of different metal ions.

4.4 Conclusion

In conclusion, **L3H** can be established as highly selective sensor for Pd^{2+} and Ni^{2+} ions. In both metal ions, the colour of the solution of **L3H** changed from colourless to greenish yellow, which makes it viable for detection of Pd^{2+} and Ni^{2+} without the help of any costly instrument. The limit of detection of both ions is well below the permitted daily exposure value and **L3H** can be used for detection of trace amounts of Pd^{2+} ions. This probe has no interference from the anti-hypertensive drug in the detection mechanism of Pd^{2+} ions. So, it has greater potential for use in pharmaceutical applications as Pd catalysts are used in industrial synthesis of drug molecules. The high binding constant values are indicative of stable complex formation with Pd^{2+} and Ni^{2+} ions and both bind with **L3H** in 1:1 ratio. Effect of pH is nominal on detection of Pd^{2+} and Ni^{2+} ions, as a wider range of pH was suitable. Theoretical studies prove that coordination of Pd^{2+} and Ni^{2+} ions cause red shift in absorption peak.

References

[1] L. Overman, *Chemical and Engineering News, American Chemical Society* **2003**.

[2] N. Della Ca', *Catalysts* **2021**, *11*, 588.

[3] D. Mc Cartney, P. J. Guiry, *Chem. Soc. Rev.* **2011**, *40*, 5122–5150.

[4] R. F. Heck, J. P. Nolley, *J. Org. Chem.* **1972**, *37*, 2320–2322.

[5] Norio. Miyaura, Akira. Suzuki, *Chem. Rev.* **1995**, *95*, 2457–2483.

[6] K. Tamao, K. Sumitani, M. Kumada, *J. Am. Chem. Soc.* **1972**, *94*, 4374–4376.

[7] S. Baba, E. Negishi, *J. Am. Chem. Soc.* **1976**, *98*, 6729–6731.

[8] E. Negishi, A. O. King, N. Okukado, *J. Org. Chem.* **1977**, *42*, 1821–1823.

[9] D. Milstein, J. K. Stille, *J. Am. Chem. Soc.* **1978**, *100*, 3636–3638.

[10] K. Sonogashira, *J. Organomet. Chem.* **2002**, *653*, 46–49.

[11] R. Chinchilla, C. Nájera, *Chem. Rev.* **2007**, *107*, 874–922.

[12] D. S. Surry, S. L. Buchwald, *Chem. Sci.* **2011**, *2*, 27–50.

[13] S. Czerczak, J. P. Gromiec, A. Pałaszewska-Tkacz, *Patty's Toxicology*, John Wiley & Sons, Inc., Hoboken, NJ, USA, **2001**.

[14] K. S. Egorova, V. P. Ananikov, *Organometallics* **2017**, *36*, 4071–4090.

[15] L. Wang, D. Ye, D. Cao, *Spectrochim. Acta A Mol. Biomol. Spectrosc.* **2012**, *90*, 40–44.

[16] J. L. Boer, S. B. Mulrooney, R. P. Hausinger, *Arch. Biochem. Biophys.* **2014**, *544*, 142–152.

[17] M. Alfano, C. Cavazza, *Protein Sci.* **2020**, *29*, 1071–1089.

[18] S. W. Ragsdale, *Curr. Opin. Chem. Biol.* **1998**, *2*, 208–215.

[19] S. W. Ragsdale, *J. Inorg. Biochem.* **2007**, *101*, 1657–1666.

[20] K. K. Das, R. C. Reddy, I. B. Bagoji, S. Das, S. Bagali, L. Mullur, J. P. Khodnapur, M. S. Biradar, *J. Basic. Clin. Physiol. Pharmacol.* **2019**, *30*, 141–152.

[21] B. Shahzad, M. Tanveer, A. Rehman, S. A. Cheema, S. Fahad, S. Rehman, A. Sharma, *Plant Physiol. and Biochem.* **2018**, *132*, 641–651.

[22] X. Bu, K. Koide, E. J. Carder, C. J. Welch, *Org. Process. Res. Dev.* **2013**, *17*, 108–113.

[23] S. Masi, M. Uliana, M. Gesi, S. Taddei, A. Virdis, *Vascul. Pharmacol.* **2019**, *115*, 84–88.

[24] E. Lurbe, J. Álvarez, J. Redon, *Curr. Hypertens. Rep.* **2010**, *12*, 480–486.

[25] J. Rayadurgam, S. Sana, M. Sasikumar, Q. Gu, *Org. Chem. Front.* **2021**, *8*, 384–414.

[26] C. E. Garrett, K. Prasad, *Adv. Synth. Catal.* **2004**, *346*, 889–900.

[27] M. V. Klyuev, M. G. Abdullaev, Z. Sh. Abdullaeva, *Pharm. Chem. J.* **2010**, *44*, 446–451.

[28] I. Muszalska, A. Sobczak, A. Dołhań, A. Jelińska, *J. Pharm. Sci.* **2014**, *103*, 2–28.

[29] L. J. Goossen, B. Melzer, *J. Org. Chem.* **2007**, *72*, 7473–7476.

[30] S. Ghosh, A. S. Kumar, G. N. Mehta, *J. Chem. Res.* **2010**, *34*, 191–193.

[31] S. Ghosh, A. S. Kumar, G. N. Mehta, *Beilstein J.Org. Chem.* **2010**, *6*, 1-4.

[32] M. Seki, *ACS Catal.* **2011**, *1*, 607–610.

[33] S. Ghosh, A. S. Kumar, R. Soundararajan, G. N. Mehta, *Synth. Commun.* **2009**, *39*, 3880–3887.

[34] O. Singh, H. Kumar Chopra, P. Loktongbam, *Int. J. Sci.Res. Publ.* **2017**, *7*, 444.

[35] J. Lu, X. Li, S. Yuan, Y. Wang, H. Sun, W. Weng, Y. Shi, X. Wang, K. Huang, X. Sun, T. Wu, *Org. Process. Res. Dev.* **2022**, *26*, 1247–1257.

[36] R. D. Larsen, A. O. King, C. Y. Chen, E. G. Corley, B. S. Foster, F. E. Roberts, C. Yang, D. R. Lieberman, R. A. Reamer, D. M. Tschaen, T. R. Verhoeven, P. J. Reider, Y. S. Lo, L. T. Rossano, A. S. Brookes, D. Meloni, J. R. Moore, J. F. Arnett, *J. Org. Chem.* **1994**, *59*, 6391–6394.

[37] Y.-J. Ding, Y. Li, S.-Y. Dai, Q. Lan, X.-S. Wang, *Org. Biomol. Chem.* **2015**, *13*, 3198–3201.

[38] Z. Chen, Y. Guo, H. Niu, J. Wang, J. Li, C. Li, R. Qiao, *Org. Process. Res. Dev.* **2022**, *26*, 2438–2446.

[39] A. D. Martin, A. R. Siamaki, K. Belecki, B. F. Gupton, *J. Org. Chem.* **2015**, *80*, 1915–1919.

[40] ICH The International Council for Harmonisation of Technical Requirements for Pharmaceuticals for Human Use, *Committee for Medicinal Products for Human Use ICH Guideline Q3D (R2) on Elemental Impurities*, Amsterdam, The Netherlands, **2022**.

[41] R. Balamurugan, J.-H. Liu, B.-T. Liu, *Coord. Chem. Rev.* **2018**, *376*, 196–224.

[42] M. G. Choi, J.-Y. Seo, E. J. Cho, S.-K. Chang, *J. Photochem. Photobiol. A Chem.* **2022**, *429*, 113920.

[43] Q. Xia, S. Feng, D. Liu, G. Feng, *Sens. Actuators. B Chem.* **2018**, *258*, 98–104.

[44] N. Kumari, N. Dey, K. Kumar, S. Bhattacharya, *Chem. Asian. J.* **2014**, *9*, 3174–3181.

[45] S. Mahata, A. Bhattacharya, J. P. Kumar, B. B. Mandal, V. Manivannan, *J. Photochem. Photobiol. A Chem.* **2020**, *394*, 112441.

[46] H. Cui, H. Chen, Y. Pan, W. Lin, *Sens. Actuators B Chem.* **2015**, *219*, 232–237.

[47] X. Fang, Y. Zhang, M. Li, Z. Zhang, Y. Qi, X. Zhang, X. Zhang, Y. Liu, J. Li, H. Yu, *Dyes Pigm.* **2023**, *209*, 110929.

[48] W. Feng, L. Bai, S. Jia, G. Feng, *Sens. Actuators B Chem.* **2018**, *260*, 554–562.

[49] W. Luo, M. Lei, Y. Wang, H. Gao, Y. Wang, Q. Zhou, Z. Xu, F. Yang, *Anal. Methods* **2019**, *11*, 1080–1086.

[50] M. G. Choi, J.-Y. Seo, E. J. Cho, S.-K. Chang, *J. Photochem. Photobiol. A Chem.* **2022**, *429*, 113920.

[51] X. Chen, H. Wang, X. Ma, M. Wang, Y. Zhang, G. Gao, J. Liu, S. Hou, *Dyes Pigm.* **2018**, *148*, 286–291.

[52] H. Li, J. Fan, J. Du, K. Guo, S. Sun, X. Liu, X. Peng, *Chem. Commun.* **2010**, *46*, 1079–1081.

[53] W. Zhou, Q. Gao, D. Liu, C. Li, S. Liu, K. Xia, B. Han, C. Zhou, *Spectrochim. Acta A Mol. Biomol. Spectrosc.* **2020**, *237*, 118365.

[54] Y. Tang, Y. Huang, L. Lu, C. Wang, T. Sun, J. Zhu, G. Zhu, J. Pan, Y. Jin, A. Liu, M. Wang, *Tetrahedron Lett.* **2018**, *59*, 3916–3922.

[55] P. P. Dash, P. Mohanty, S. Behera, R. Behura, B. B. Palai, B. Nath, S. K. Sahoo, B. R. Jali, *Methods* **2023**, *219*, 127–138.

[56] H. Wang, S. Zhao, Y. Xu, L. Li, B. Li, M. Pei, G. Zhang, *J. Mol. Struct* **2020**, *1203*, 127384.

[57] M. Aginagalde, Y. Vara, A. Arrieta, R. Zangi, V. L. Cebolla, A. Delgado-Camón, F. P. Cossío, *J. Org. Chem.* **2010**, *75*, 2776–2784.

[58] F. Sultana, S. Reddy Bonam, V. G. Reddy, V. L. Nayak, R. Akunuri, S. Rani Routhu, A. Alarifi, M. S. K. Halmuthur, A. Kamal, *Bioorg. Chem.* **2018**, *76*, 1–12.

[59] Gaussian 16, Revision C.01, M. J. Frisch, G. W. Trucks, H. B. Schlegel, G. E. Scuseria, M. A. Robb, J. R. Cheeseman, G. Scalmani, V. Barone, G. A. Petersson, H. Nakatsuji, X. Li, M. Caricato, A. V. Marenich, J. Bloino, B. G. Janesko, R. Gomperts, B. Mennucci, H. P. Hratchian, J. V. Ortiz, A. F. Izmaylov, J. L. Sonnenberg, D. Williams-Young, F. Ding, F. Lipparini, F. Egidi, J. Goings, B. Peng, A. Petrone, T. Henderson, D. Ranasinghe, V. G. Zakrzewski, J. Gao, N. Rega, G. Zheng, W. Liang, M. Hada, M. Ehara, K. Toyota, R. Fukuda, J. Hasegawa, M. Ishida, T. Nakajima, Y. Honda, O. Kitao, H. Nakai, T. Vreven, K. Throssell, J. A. Montgomery, Jr., J. E. Peralta, F. Ogliaro, M. J. Bearpark, J. J. Heyd, E. N. Brothers, K. N. Kudin, V. N. Staroverov, T. A. Keith, R. Kobayashi, J. Normand, K. Raghavachari, A. P. Rendell, J. C. Burant, S. S. Iyengar, J. Tomasi, M. Cossi, J. M. Millam, M. Klene, C. Adamo, R. Cammi, J. W. Ochterski, R. L. Martin, K. Morokuma, O. Farkas, J. B. Foresman, and D. J. Fox, Gaussian, Inc., Wallingford CT, **2016**.

[60] GaussView, Version 6.1, Roy Dennington, Todd A. Keith, John M. Millam, Semichem Inc., Shawnee Mission, KS, **2016**.

Appendix

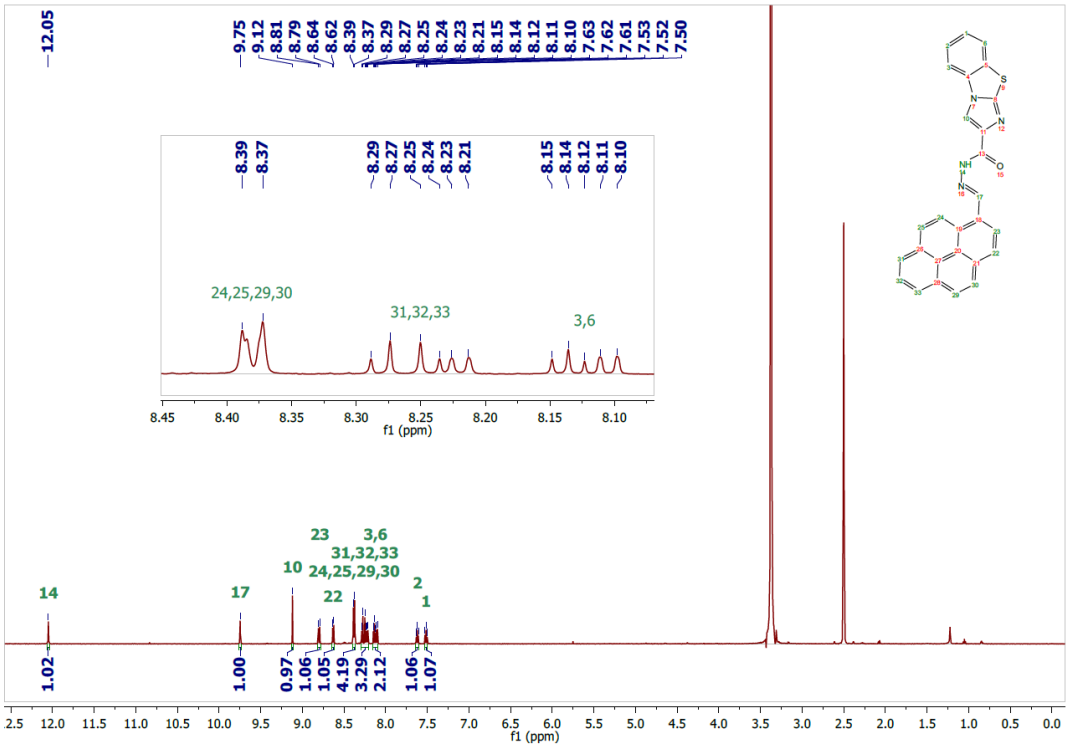

Figure A1. ^{1}H NMR (DMSO-d_6) spectrum of **L3H**.

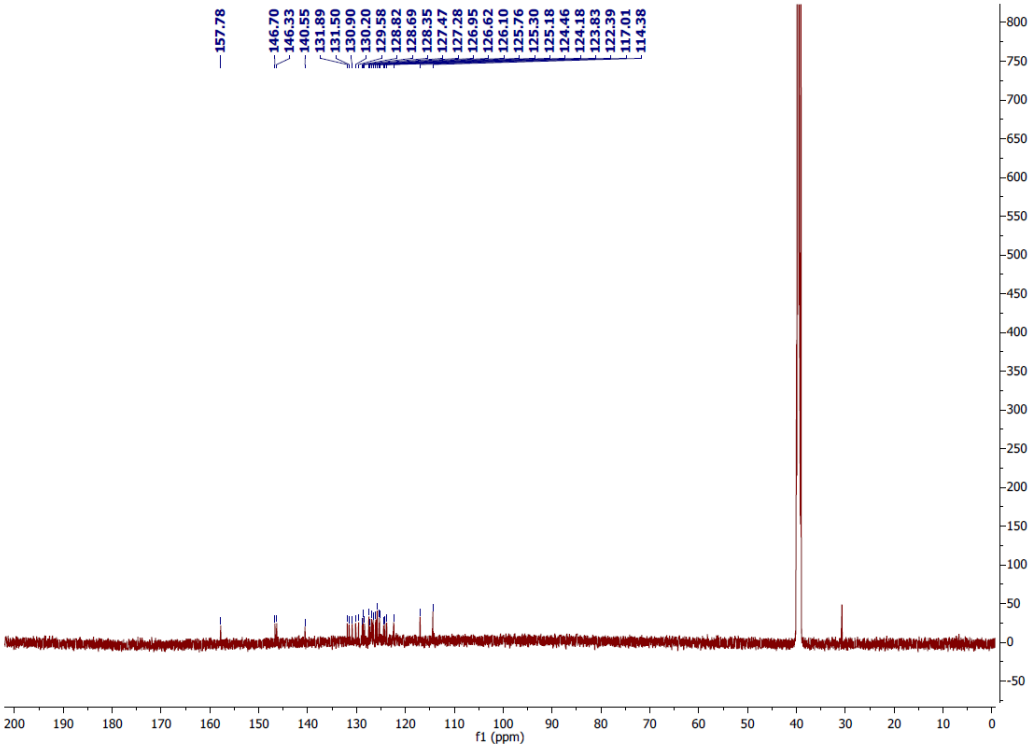

Figure A2. ^{13}C NMR (DMSO-d_6) spectrum of **L3H**.

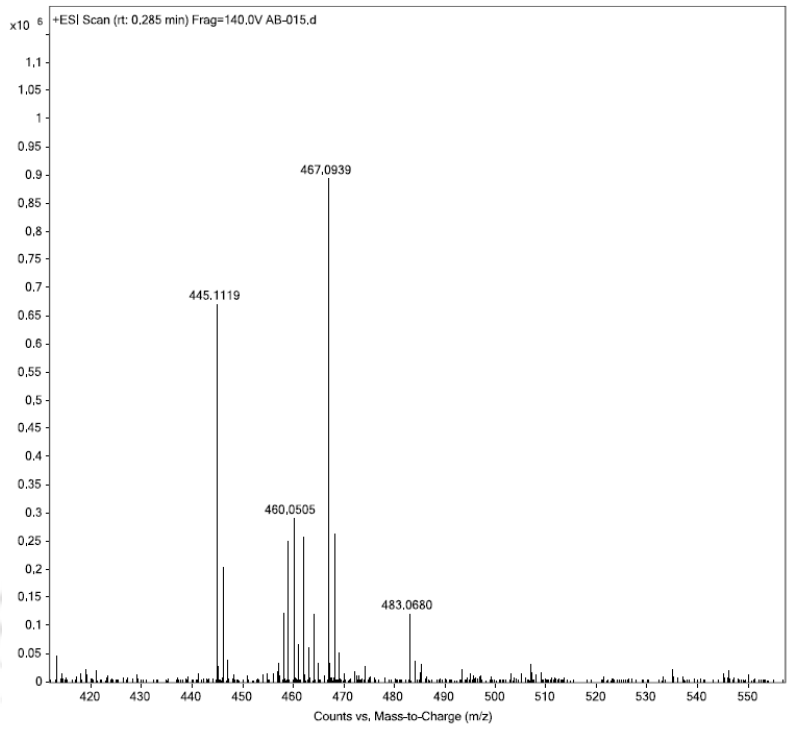

Figure A3. HRMS spectrum of **L3H**.

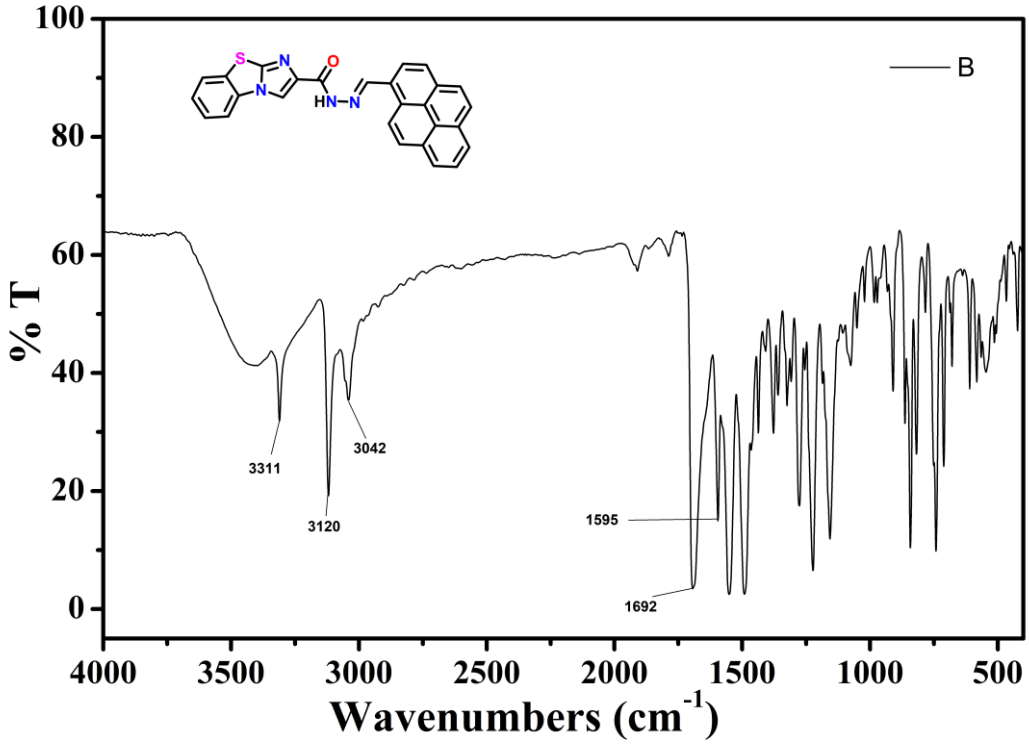

Figure A4. IR spectrum of **L3H**.

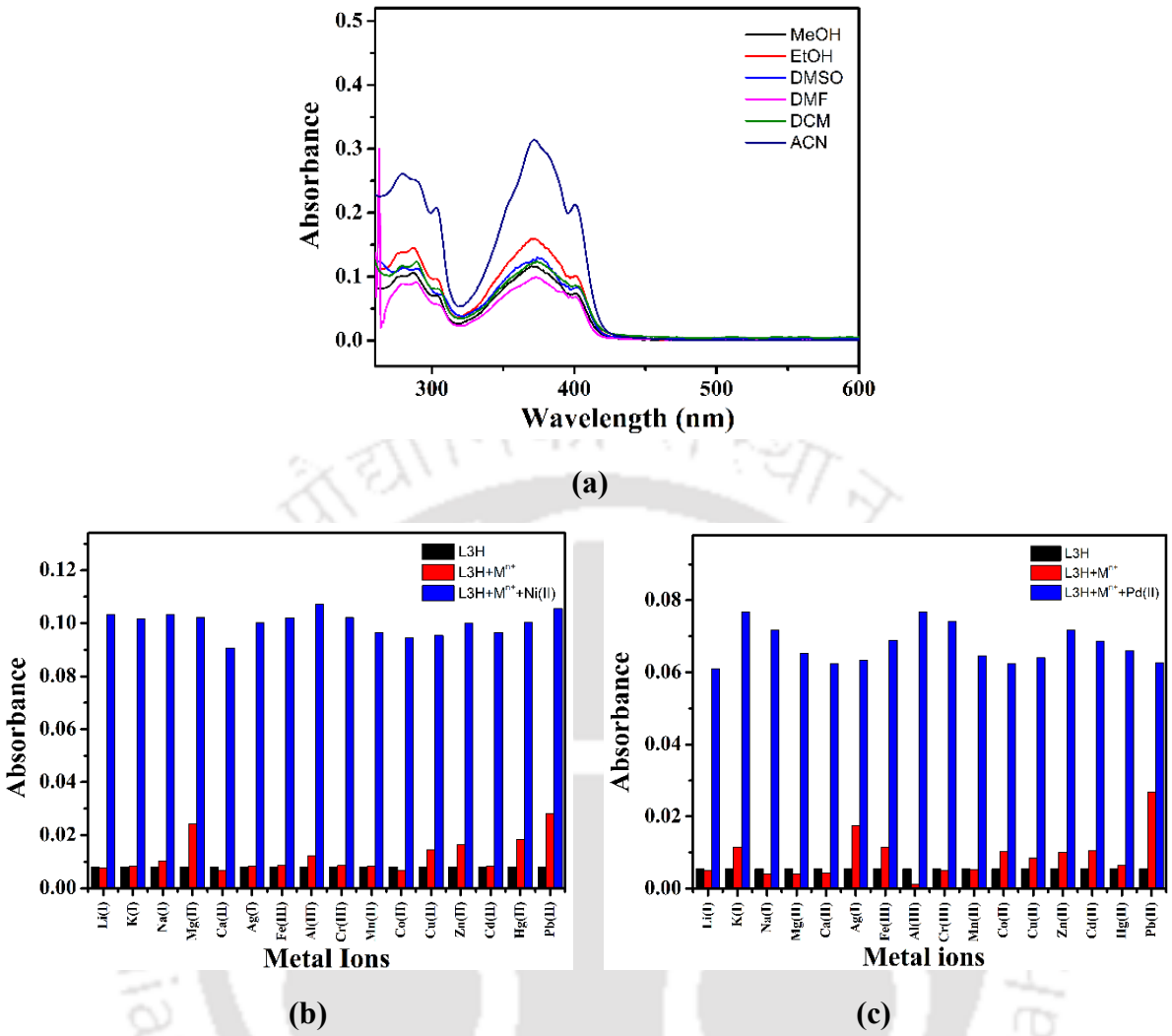

Figure A5. **(a)** UV-Vis spectra of **L3H** in different solvents. Bar diagram for studying interference by other metal ions with **L3H** in presence of **(b)** Ni^{2+} and **(c)** Pd^{2+}.

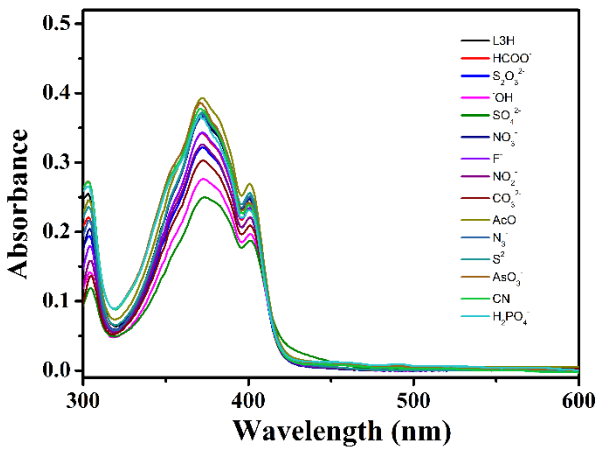

Figure A6. Interaction of anions with **L3H**.

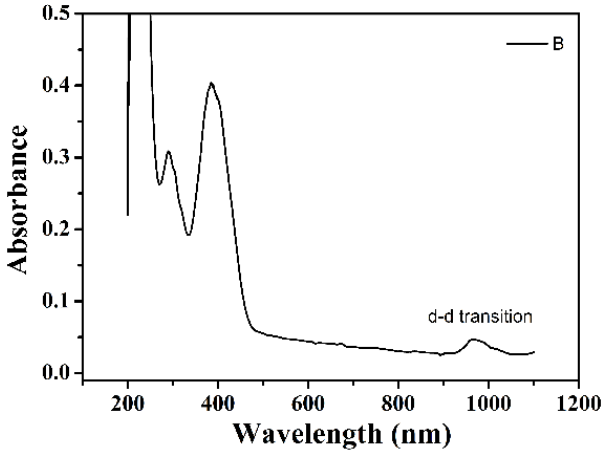

Figure A7. Observation of d-d transition at higher concentration of $NiCl_2$ with **L3H**

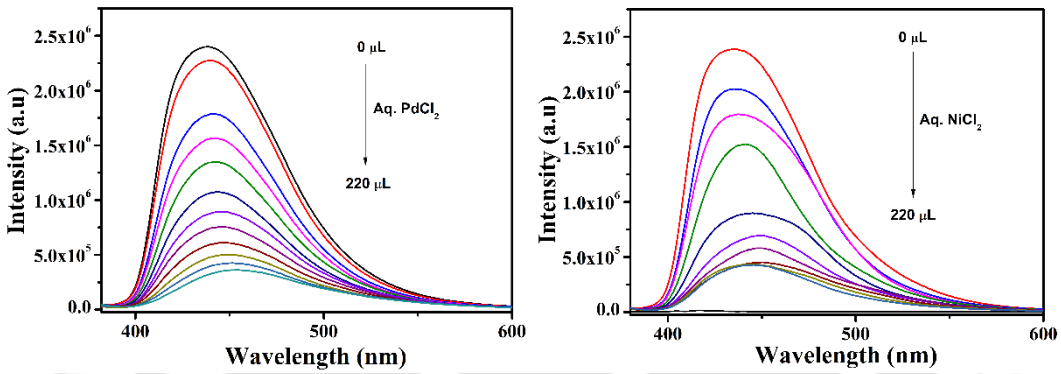

Figure A8. Fluorescence titration of **L3H** with aqueous (a) $PdCl_2$ and (b)$NiCl_2$ solutions.

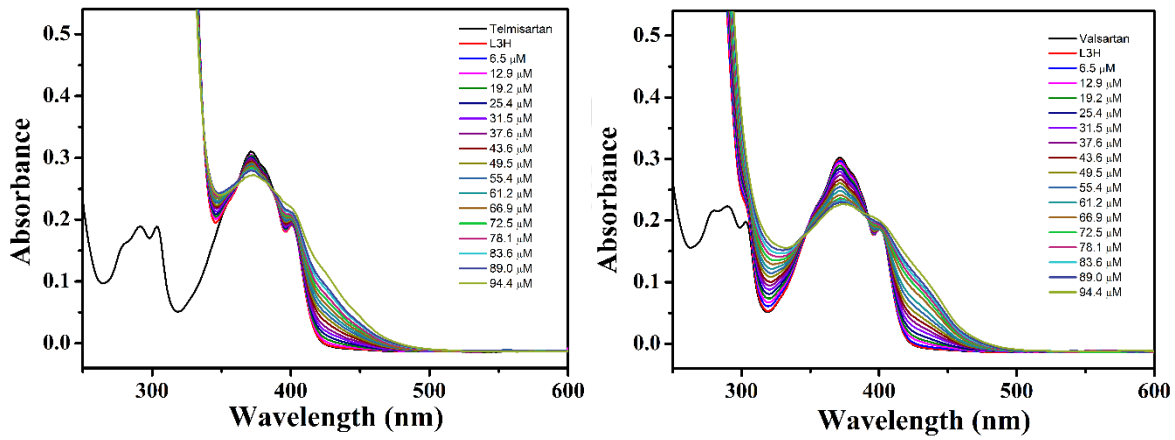

(a) **(b)**

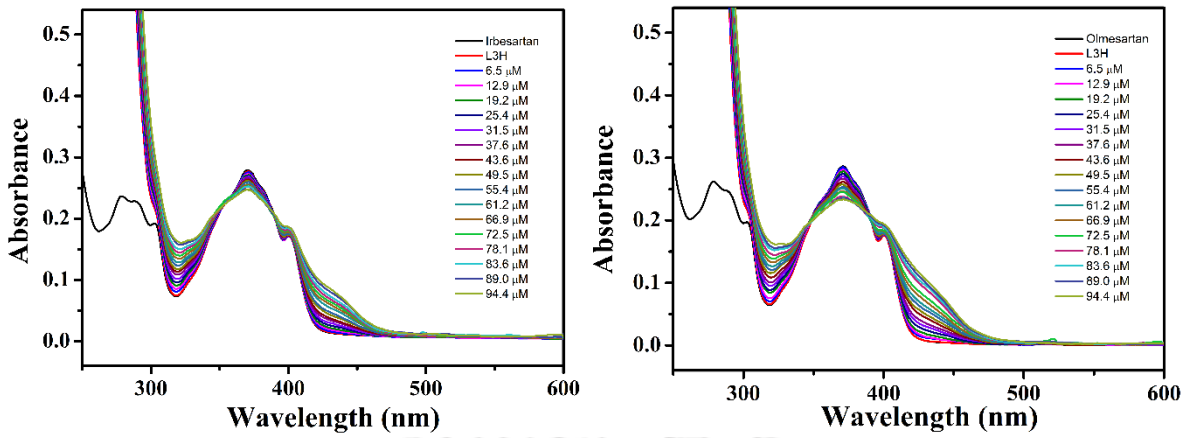

(c) (d)

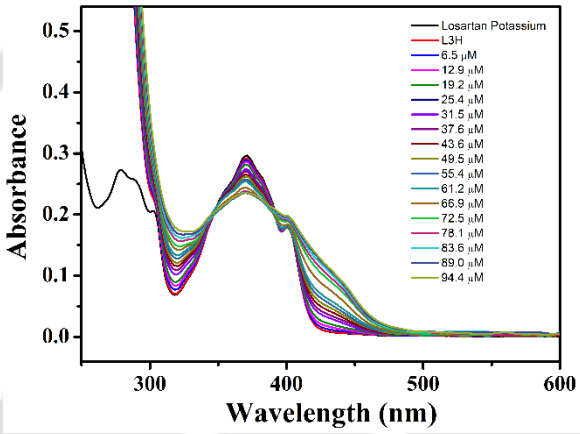

(e)

Figure A9. UV-Vis titration of **L3H** with $PdCl_2$ in presence of **(a)** Telmisartan, **(b)** Valsartan, **(c)** Irbesartan, **(d)** Olmesartan medoxomil and **(e)** Losartan Potassium.

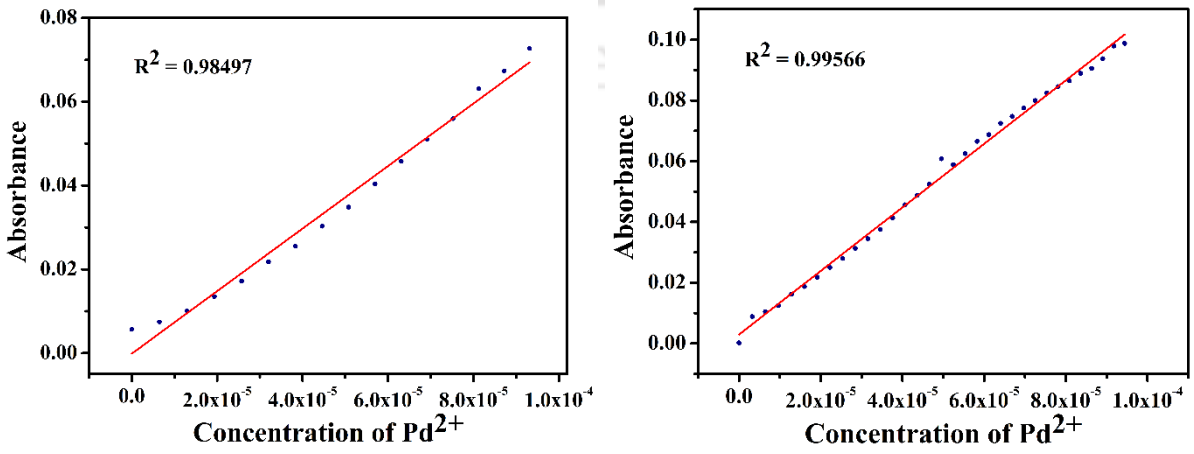

(a) (b)

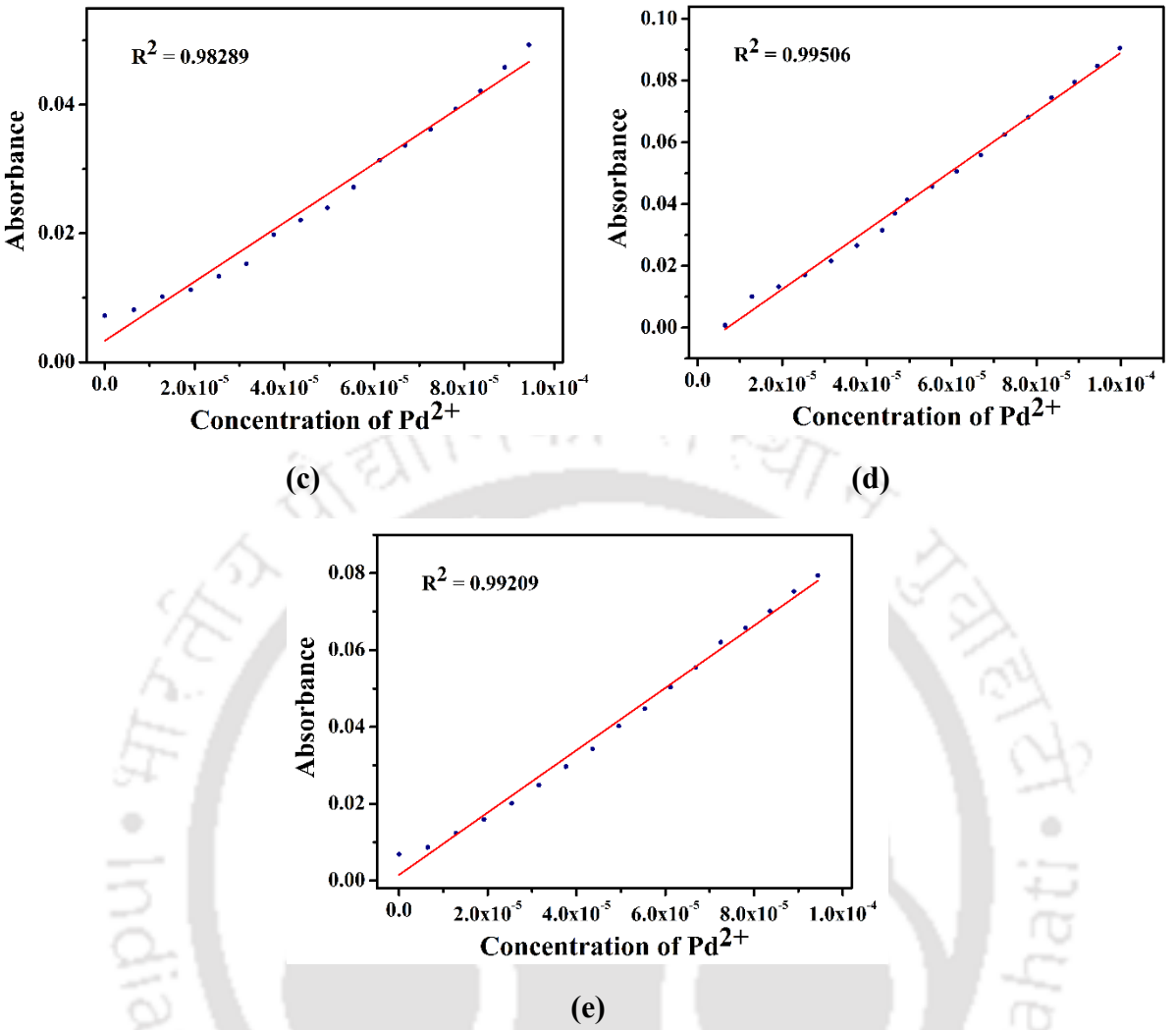

Figure A10. Calibration plot from the UV-Vis titration of **L3H** with $Pd(OAc)_2$ in presence of **(a)** Telmisartan, **(b)** Valsartan, **(c)** Irbesartan, **(d)** Olmesartan medoxomil and **(e)** Losartan Potassium.

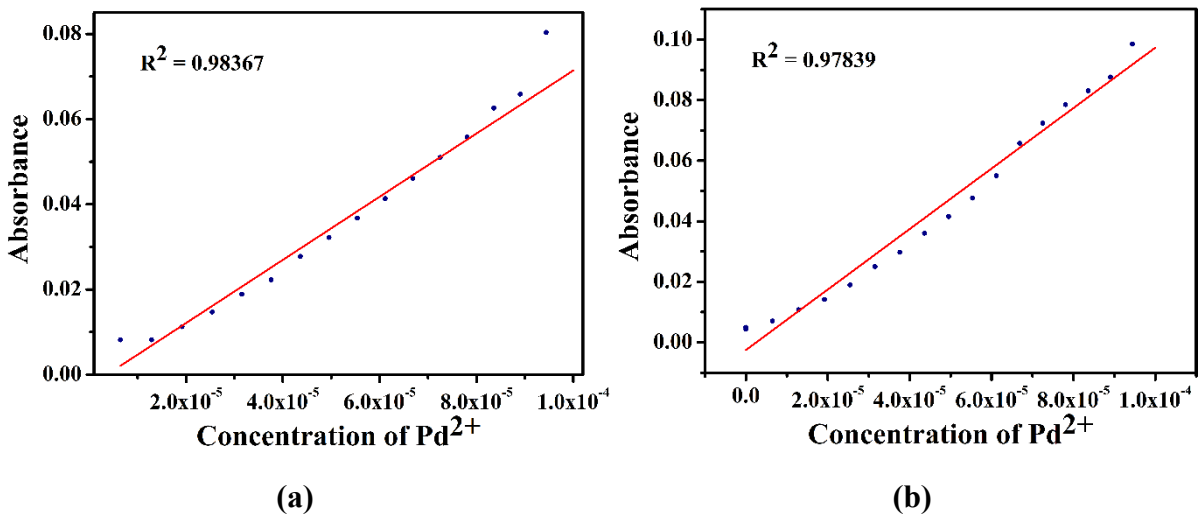

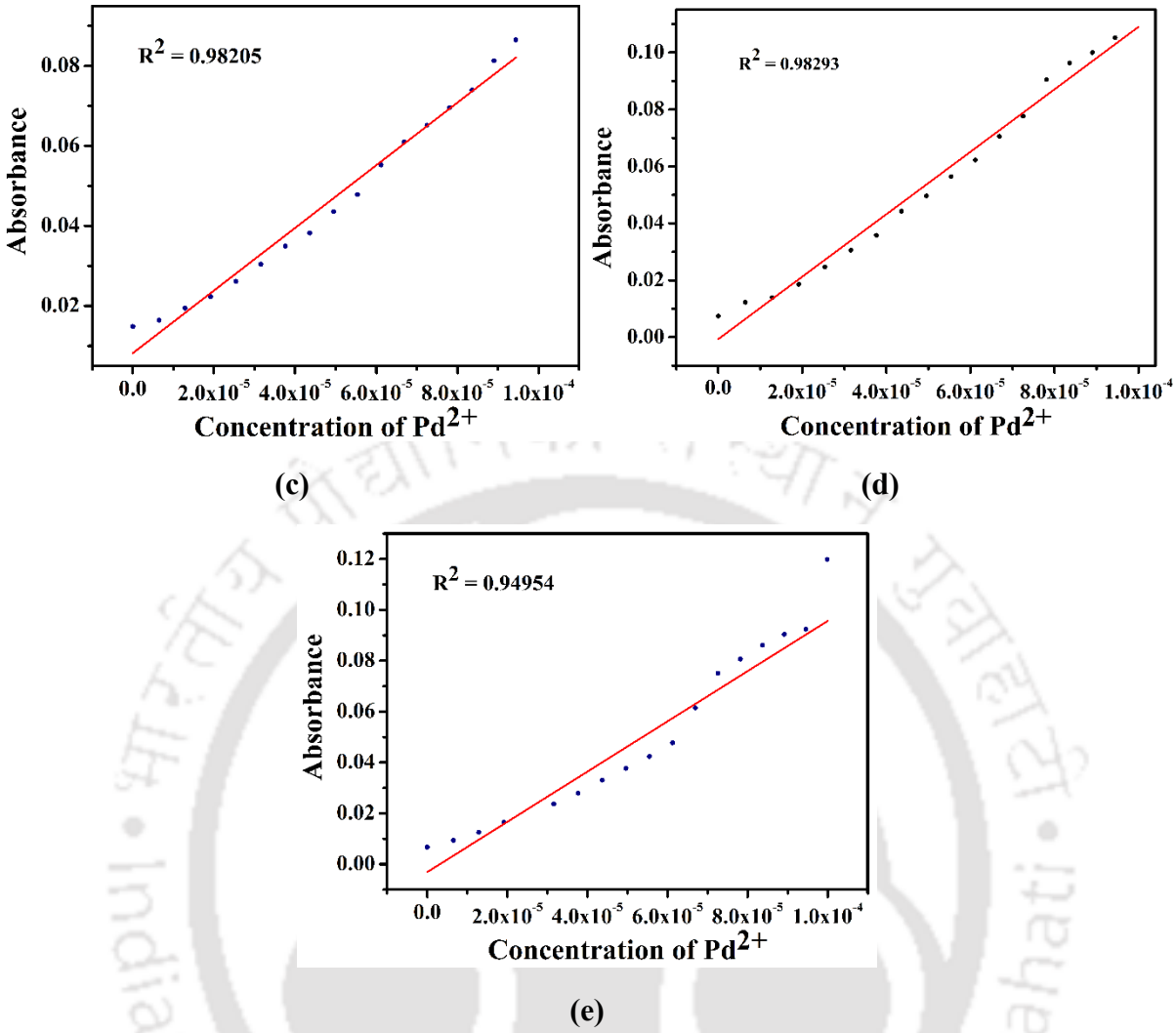

Figure A11. Calibration plot from the UV-Vis titration of **L3H** with $PdCl_2$ in presence of **(a)** Telmisartan, **(b)** Valsartan, **(c)** Irbesartan, **(d)** Olmesartan medoxomil and **(e)** Losartan Potassium.

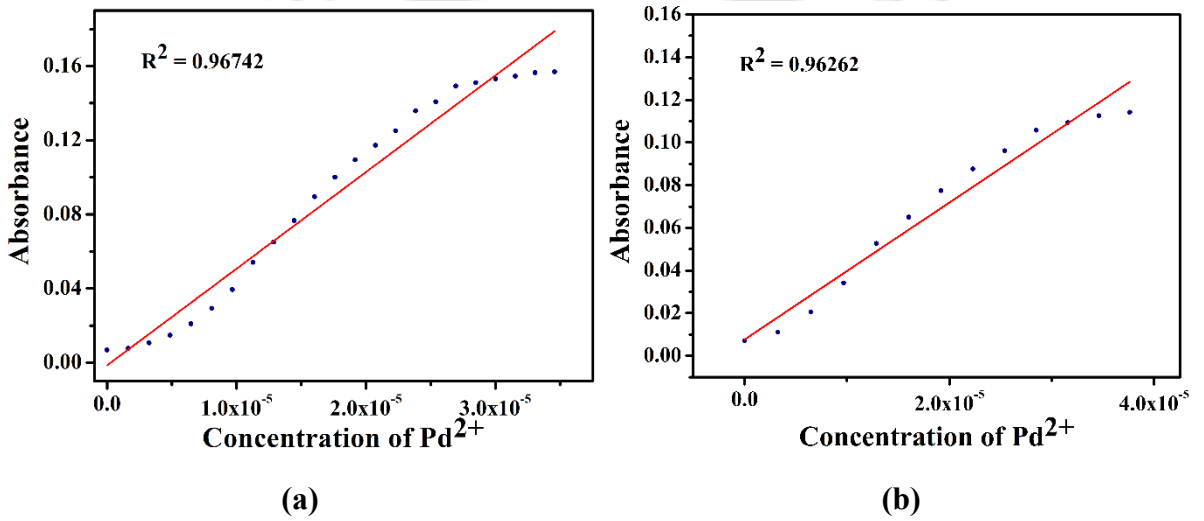

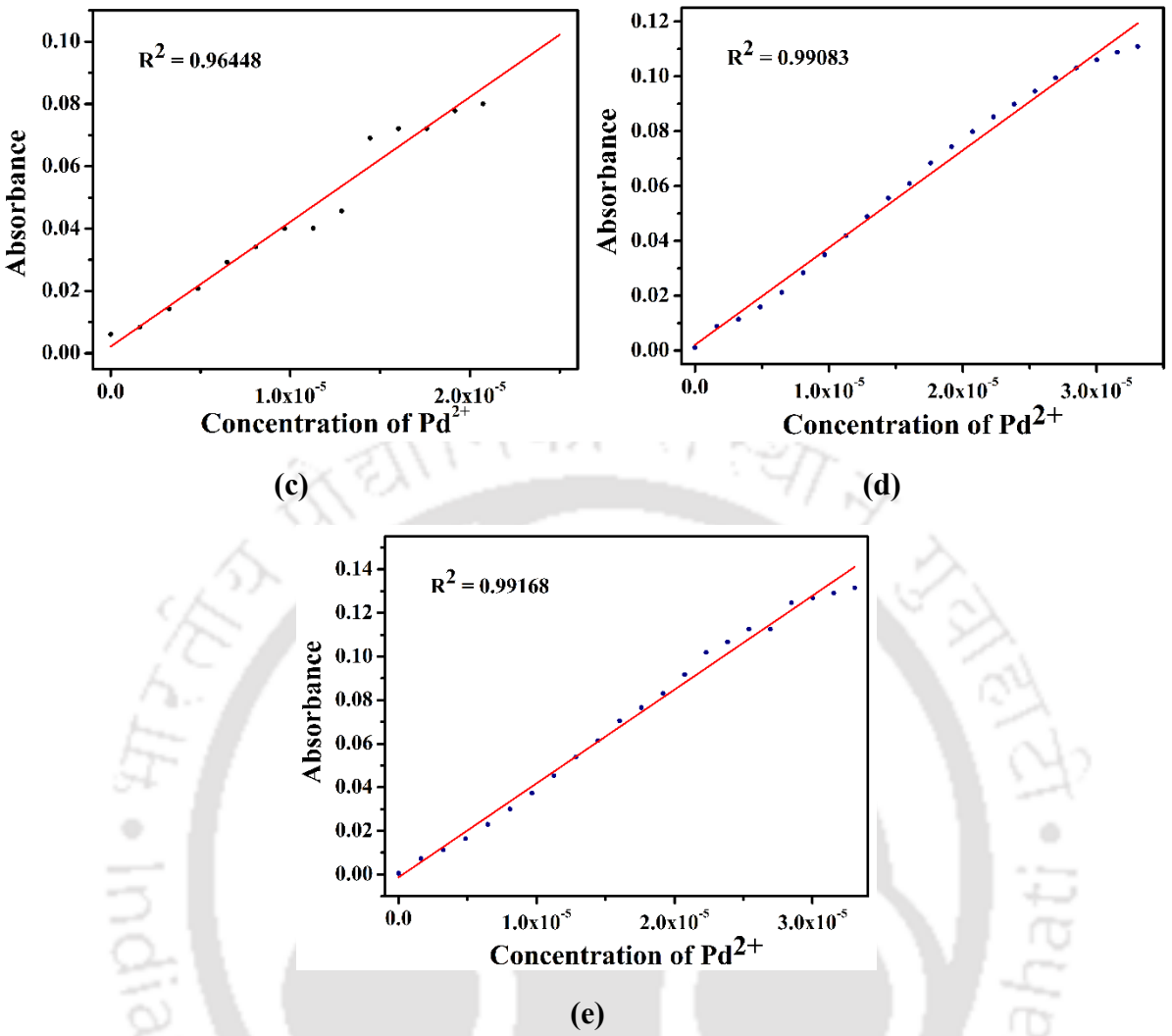

Figure A12. Calibration plot from the UV-Vis titration of **L3H** with $Pd(PPh_3)_2Cl_2$ in presence of **(a)** Telmisartan, **(b)** Valsartan, **(c)** Irbesartan, **(d)** Olmesartan medoxomil and **(e)** Losartan Potassium.

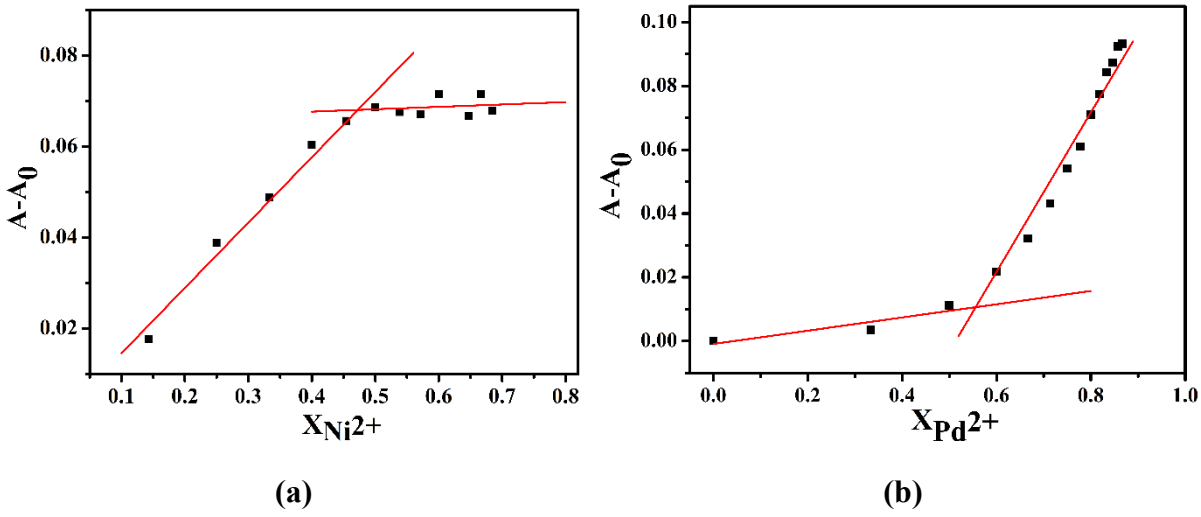

Figure A13. Jobs plot analysis for **(a)** Ni^{2+} and **(b)** Pd^{2+}

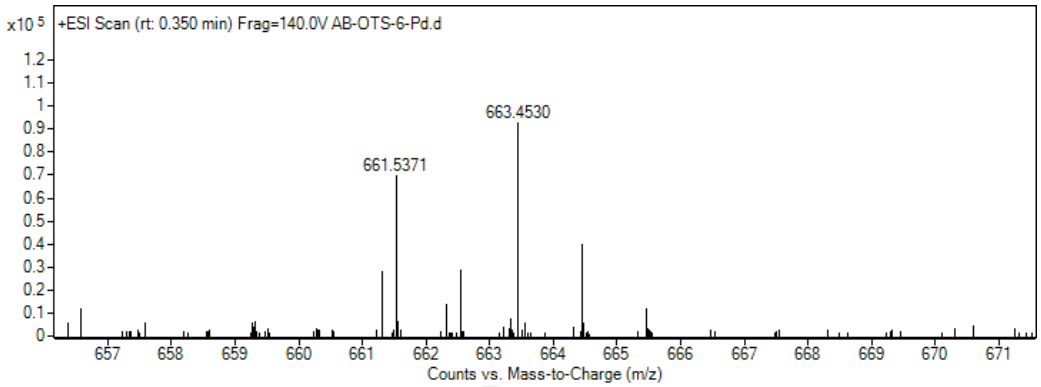

Figure A14. Mass spectrometry (HRMS) of **L3H** with $PdCl_2$ in acetonitrile solution

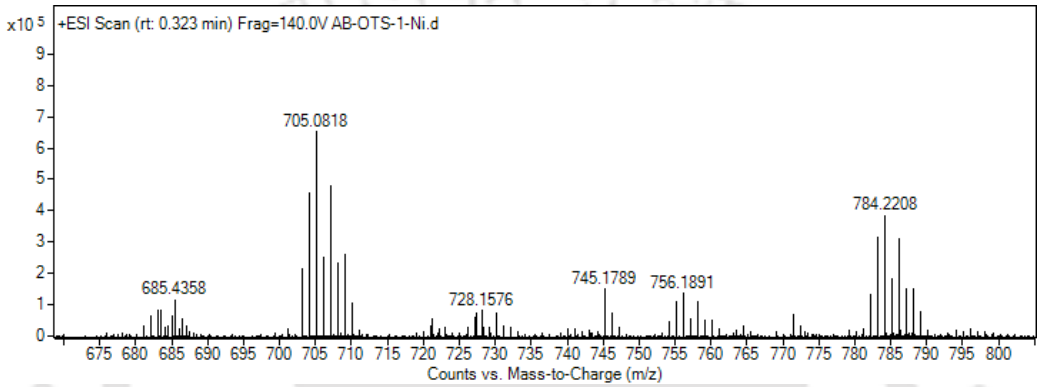

Figure A15. Mass spectrometry (HRMS) of **L3H** with $NiCl_2$ in acetonitrile solution

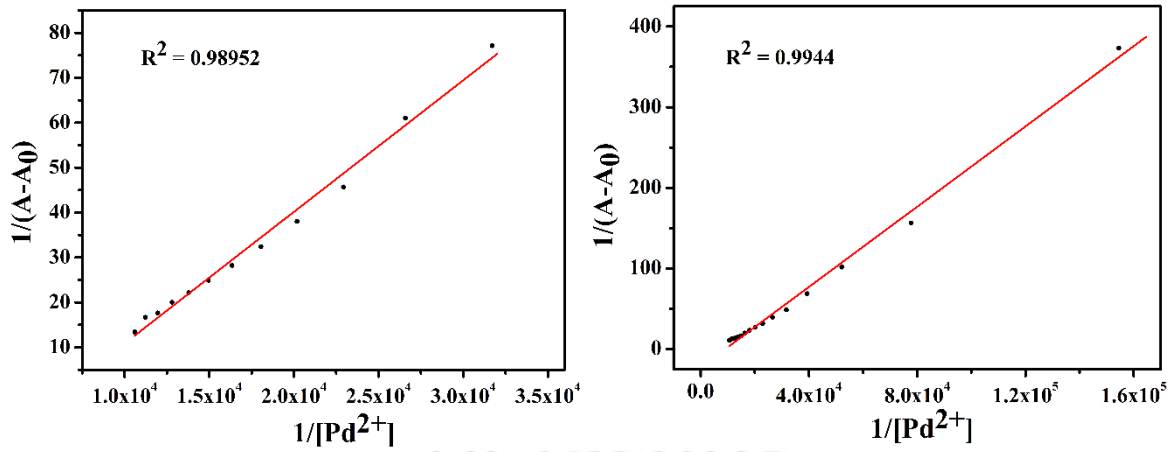

(a) **(b)**

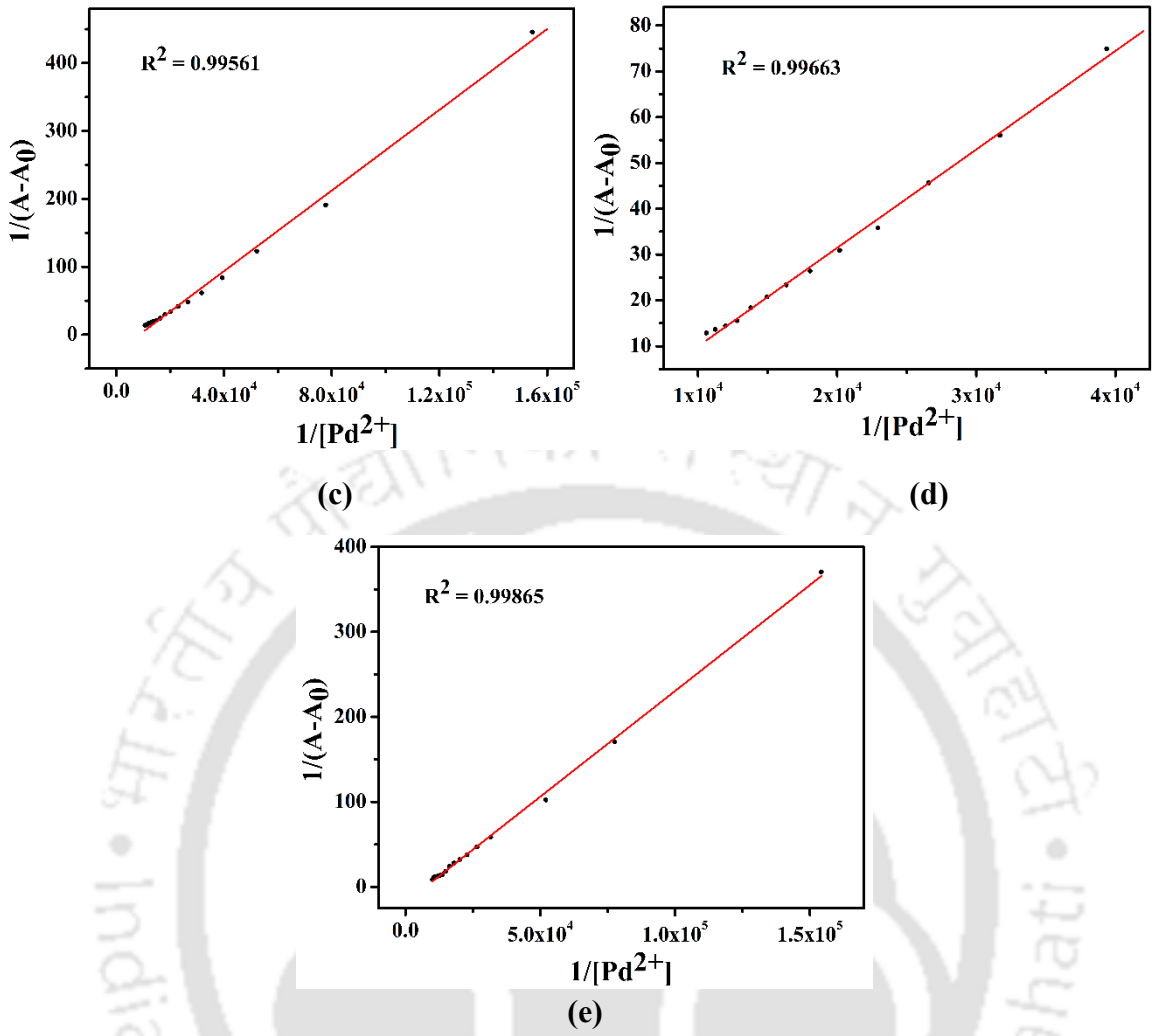

Figure A16. Benesi Hildebrand plot from the UV-Vis titration of **L3H** with $PdCl_2$ in presence of **(a)** Telmisartan, **(b)** Valsartan, **(c)** Irbesartan, **(d)** Olmesartan medoxomil and **(e)** Losartan Potassium.

3.4 Limit of detection

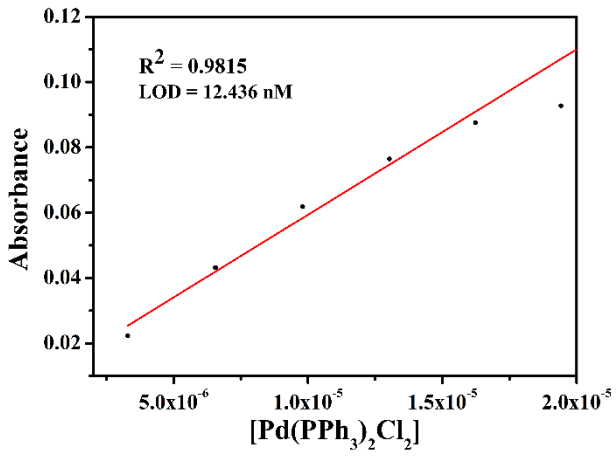

Figure. A17 Calibration plot for determination of limit of detection by **L3H** for $Pd(PPh_3)_2Cl_2$

Table A1

Probe	Solvent medium	LOD	Metal	K_b	Ref
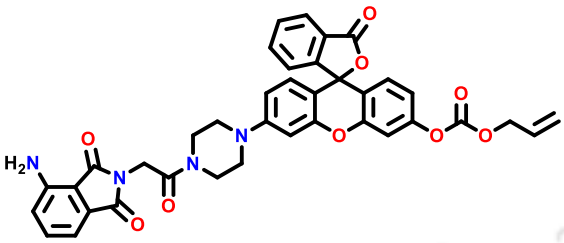	CH_3CN HEPES buffer solution (2:8, v/v, 10 mM HEPES, pH 7.4)	31 nM	Pd^{2+}	Not reported	[48]
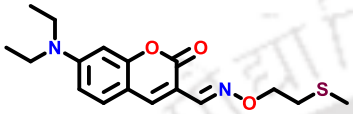	($EtOH/H_2O$ = 40:60, v/v, 25°C)	41.5 nM	Pd^{2+}	Not Reported	[51]
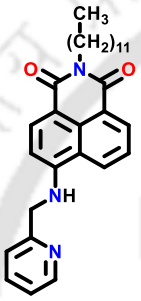	DMSO	22.5 nM	Pd^{2+}	1.37×10^4 lit mol^{-1}	[47]
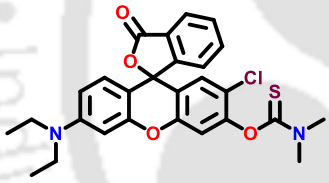	Phosphate-buffered (pH 7.0) 50% aqueous DMSO solution	4.5 µM	Pd^{2+}	Not Reported	[50]
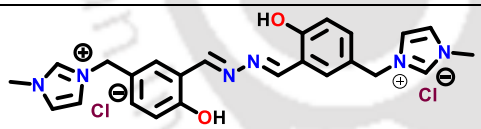	Tris-HCl buffer (pH = 7.0)	80 nM	Pd^{2+}	Not reported	[53]
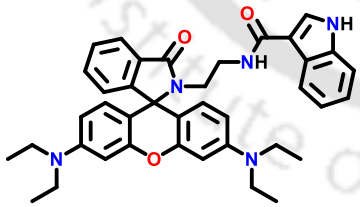	CH_3OH/PBS (5 mM, pH = 7.40, 50% CH_3OH)	170 nM	Pd^{2+}	2.20×10^4 lit mol^{-1}	[49]
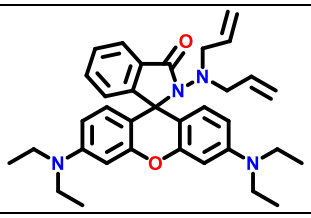	Ethanol–H_2O (1 : 1, v/v, 25° C)	185 nM	Pd^{2+}		[52]
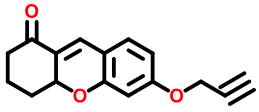	PBS buffer-ethanol (9:1, v/v, pH = 7.4)	22 nM	Pd^{2+}	Not Reported	[46]

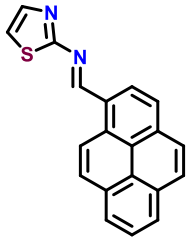	DMSO	0.5 wt%	Water	Not applicable	[55]
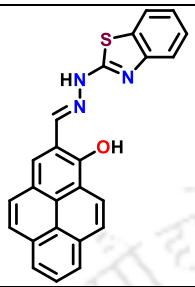	EtOH-HEPES (65:35, v/v, pH = 7.20)	2.58×10^{-7} M	Zn^{2+}	$4.04 \times 10^{4}\ M^{-1}$	[54]
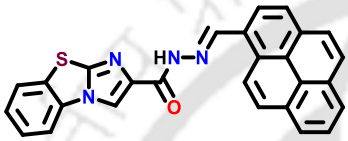	CH_3CN HEPES buffer (2mM, pH = 7.34, 4:1, *v/v*)	12.4 nM(Pd^{2+}) 70 nM (Ni^{2+})	Pd^{2+} and Ni^{2+}		This work

Chapter 5

Selective colorimetric detection of Co^{2+} and Cu^{2+} ions by a 2,7-dichlorofluorescein based ligand: use of its *in situ* Cu-complex for estimation of BSA and HSA proteins.

Abstract:

A probe (**L4H**) based on 2,7-dichlorofluorescein has been synthesized and evaluated as a colorimetric sensor for selective detection of metal ions. This probe has been found to exhibit a colour change from colourless to green Co^{2+} ions and violet in the presence of Cu^{2+} in CH_3CN/HEPES buffer (4:1, *v/v*, 2 mM, pH = 7.34). The LOD values are 2.85 µM (for Co^{2+} ion) and 70.33 nM (for Cu^{2+} ion) which are lower than the WHO guideline values. Binding stoichiometry (probe : metal ion) of 1:2 (for Co^{2+}) and 1:1 (for Cu^{2+}) has been established from Jobs plot and mass spectrum. The binding constant values calculated from the plot are 2.013×10^4 L mol^{-1} (for Co^{2+}-**L4H**) and 5.986×10^4 L mol^{-1} (Cu^{2+}-**L4H**) complex as obtained from the Benesi-Hildebrand plot, indicate high binding affinity. This *in situ* Cu^{2+}-**L4H** complex formed can be utilised for the quantification of protein like BSA and HSA. The pH tolerance of the probe was found to be in the range of 2-8 (for Co^{2+}) and 1-10 (for Cu^{2+}). Differences in colour upon addition of the metal ions lead to its another application as molecular logic gate. Structure optimisation and theoretical studies performed on **L4H**, $[Co(\mathbf{L4})_2]^+$ and $[Cu(\mathbf{L4})(H_2O)]^+$ in gas phase, showed good correlation between calculated UV-Vis and experimental spectra. Thus, this sensor molecule can be utilized for detection of Co^{2+} and Cu^{2+} ions and its potential application as quantification of proteins and logic gate is also established.

5.1 Introduction:

Copper is present in many biological systems like the enzymes, cytochrome *c* oxidase, superoxide dismutase and tyrosinase [1]. Menkes syndrome and Wilson disease are genetic diseases that happens due to copper deficiency and overload, respectively [2]. There are many health hazards due to copper overload in the human body, *viz*., Indian childhood cirrhosis, endemic Tyrolean infantile cirrhosis and idiopathic copper toxicosis in infants and children under 6 years of age [3–6]. Wilson disease which is an autosomal disorder that leads to inefficient copper excretion resulting in copper deposition in liver and kidney [5]. There are evidences that many eukaryotes utilize copper as potent anti-microbial weapon [7].

Cobalt is one of the most versatile metals that is being used in electric devices[8], batteries, catalysts in petrochemical industries[9,10], manufacturing alloys[11], radiological instruments to treat cancer[12] and in artificial hip and knee joints[13]. Co is also present in vitamin B12, which is a cofactor for the enzymes, methionine synthase and methylmalonylCoA mutase[14].

Fluorescein is a well-known fluorophore and its photophysical properties were exploited to make selective sensors. A ferrocene-appended fluorescein was found to be a ratiometric chemosensor for the detection of Fe^{3+} and Hg^{2+} ions in the aqueous medium.[15] A Schiff base having fluorescein moiety[16] was found detect Zn^{2+} ions by "*turn on*" fluorescence response. A nano-sized fluorescein-based fluorescence sensor was reported to detect Cu^{2+} ions in aqueous solution.[17] Fluorescein/thiourea-derived chemosensor was synthesized which acted as a colorimetric sensor for Hg^{2+} in an aqueous medium[18]. A fluorescein-2-(pyridin-2-ylmethoxy) benzaldehyde conjugate gave a fluorogenic *turn-on* response for Hg^{2+} ions in water and in living cells[19]. A fluorescence sensing protocol was developed for the detection of Hg^{2+} ion as well as in bio-imaging applications[20]. Fluorescein linked to two rhodamine B moieties was used for the detection of Hg^{2+} ion[21]. Another fluorescence sensor, incorporating 5-aminoisophthalic acid methyl ester with fluorescein was reported for the detection of Cu^{2+} ions[22]

5.2. Experimental Section:

5.2.1 Synthesis

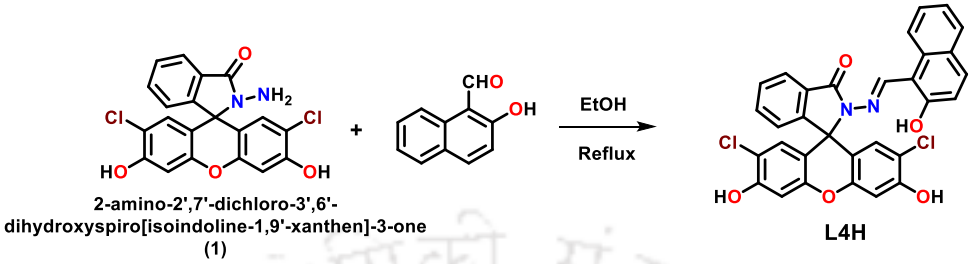

Scheme 1 Synthesis of **L4H**.

*2-Amino-2',7'-dichloro-3',6'-dihydroxyspiro[isoindoline-1,9'-xanthen]-3-one (**1**).*

Compound **1** was prepared according to the reported procedures [23,24].

*2',7'-dichloro-3',6'-dihydroxy-2-(((2-hydroxynaphthalen-1-yl)methylene)amino)spiro[isoindoline-1,9'-xanthen]-3-one (**L4H**)*:

To **1**, (0.200 g, 0.48 mmol) dissolved in hot ethanol (20 mL) 2-hydroxynaphthaldehyde (91.3 g, 0.53 mmol) was added and heated at reflux for 12 h. The volume of solvent was reduced to half, the yellow precipitate obtained was filtered and washed with ice-cold ethanol and dried under a vacuum. Yield: 0.133 g (49 %). 600 MHz ^{1}H NMR (DMSO-d_6, δ (ppm), J (Hz)): 11.23 (1H, s), 11.09 (2H, s), 10.08 (1H, s), 8.10 (1H, d, J = 8.6 Hz), 7.99 (1H, d, J = 7.0 Hz) 7.86 (1H, d, J = 9.0 Hz), 7.80 (1H, d, J = 7.9 Hz), 7.74 – 7.68 (2H, m), 7.41 (1H, t, J = 7.7 Hz), 7.34 (1H, t, J = 7.4 Hz), 7.27 (1H, d, J = 7.3 Hz), 7.09 (1H, d, J = 8.9 Hz), 6.91 (s, 2H), 6.66 (s, 2H) (Figure A1). 150 MHz ^{13}C NMR (DMSO-d_6, δ(ppm)) 163.7, 158.3, 154.9, 151.7, 151.2, 149.2, 134.9, 134.0, 131.7, 130.4, 129.9, 129.3, 128.4, 128.2, 128.2, 124.4, 124.1, 124.1, 122.4, 118.8, 116.6, 111.1, 109.8, 104.3, 65.4, (Figure A2). MS (ESI +ve) *m/z*: Calcd. for $C_{31}H_{19}Cl_2N_2O_5^+$ $[M + H]^+$ 569.0666, Found 569.0675 (Figure A3). Selected FT-IR (ATR mode, cm^{-1}): 3260 (w, ν_{C-H}), 1680 (s, $\nu_{C=O}$), 1623 (s, $\nu_{C=N}$) (Figure A4). Block-shaped crystals suitable for SC-XRD were obtained by slow evaporation of ethanol solution of **L4H**. The molecular structure of **L4H** has been determined, which is shown in Figure 1 along with the atom labelling scheme. One EtOH and one H_2O molecules were in the unit cell but they were disordered and hence it became very difficult to model so a SQUEEZE command was implemented in OLEX2 software. For that reason, signals due to EtOH and H_2O appeared in ^{1}H and ^{13}C NMR spectra of **L4H**. The crystallographic parameters are listed in Table 1.

5.2.2 X-ray crystallographic data

X-ray crystallographic data were acquired on a Bruker D8 Venture single-crystal X-ray diffractometer using graphite-monochromated Mo Kα radiation. The data refinement and cell reductions were carried out with the Bruker SAINT program[25]. Structures were further solved and refined by the full-matrix least-squares method using SHELXS-14[26]. Electron density from the region [with ca 36 e- (From calculation it may be one EtOH and one water molecule) and volume 186 $Å^3$ each, are reported by the program] were removed using the SQUEEZE procedure implemented in OLEX2 environment.

5.2.3 Preparation of stock solution of BSA and HSA

Solutions of Bovine Serum Albumin (BSA) and Human Serum Albumin (HSA) were prepared by dissolving 6 mg of them in 3 mL of deionised water making the concentration of 2 mgL^{-1}.

5.3. Results and discussion

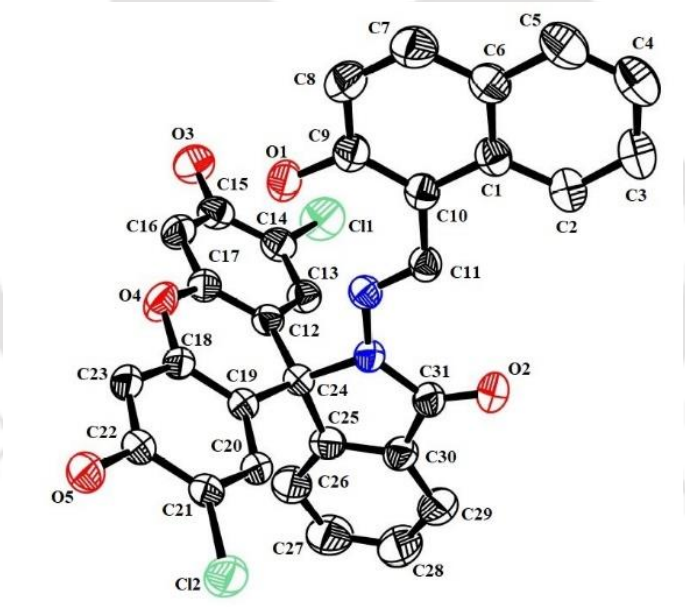

Figure 1 ORTEP diagram (30% probability) of **L4H**.

Table 1: Crystallographic data and refinement parameter

	1
Formula	$C_{31}H_{18}Cl_2N_2O_5$
Mol. wt.	569.37
Cryst. color, habit	Yellow, block
T, K	300

Cryst. syst.	monoclinic
Space group	*C2/c*
a, Å	22.031(12)
b, Å	16.503(9)
c, Å	17.972(10)
α ,deg	90
β, deg	106.407(15)
γ ,deg	90
V, $Å^3$	6268(6)
Z	8
*D*calcd, g cm^{-3}	1.207
μ, mm^{-1}	0.246
GOF[a] on F^2	1.055
F(000)	2336.0
Reflection collected	68179
Unique reflections	5528
R_1[b], wR_2[c] $(I \geq 2\sigma(I))$	0.0630, 0.1659
R_1[b], wR_2[c] (all data)	0.0945, 0.2035

[a]GOF (Goodness-of-fit) = $[\sum[w(F_0^2 - F_c^2)^2] / M - N]^{1/2}$ (M = number of reflections, N = number of parameters refined). [b]$R_1 = \sum \| F_0 | - | Fc \| / \sum | F_0 |$. [c]$wR_2 = [\sum[w(F_0^2 - F_c^2)^2] / \sum[w(F_0^2)^2]]$.

5.3.1 UV-Visible spectra

UV-Vis spectroscopic study of **L4H** in CH_3CN/HEPES buffer (4:1, *v/v*, 2 mM, pH = 7.34) revealed a peak around 370 nm (λ_{max}) with a shoulder at 386 nm. This is typically due to the π-π* transition of the two π-conjugated ring systems of the ligand frameworks, the fluorescein moiety and the 2-hydoxynaphthalene moiety. The spectra were recorded in the presence of various metal ions like Li^+, K^+, Na^+, Mg^{2+}, Ca^{2+}, Al^{3+}, Cr^{3+}, Mn^{2+}, Fe^{3+}, Co^{2+}, Ni^{2+}, Cu^{2+}, Zn^{2+}, Pd^{2+}, Cd^{2+}, Hg^{2+}, Pb^{2+}, Pt^{2+} and Ag^+. The spectral pattern was observed to change upon the addition of Co^{2+} and Cu^{2+} ions. For Cu^{2+} the spectral change was so intense that the concentration of the stock solution was reduced to 0.1 mM for further experiments.

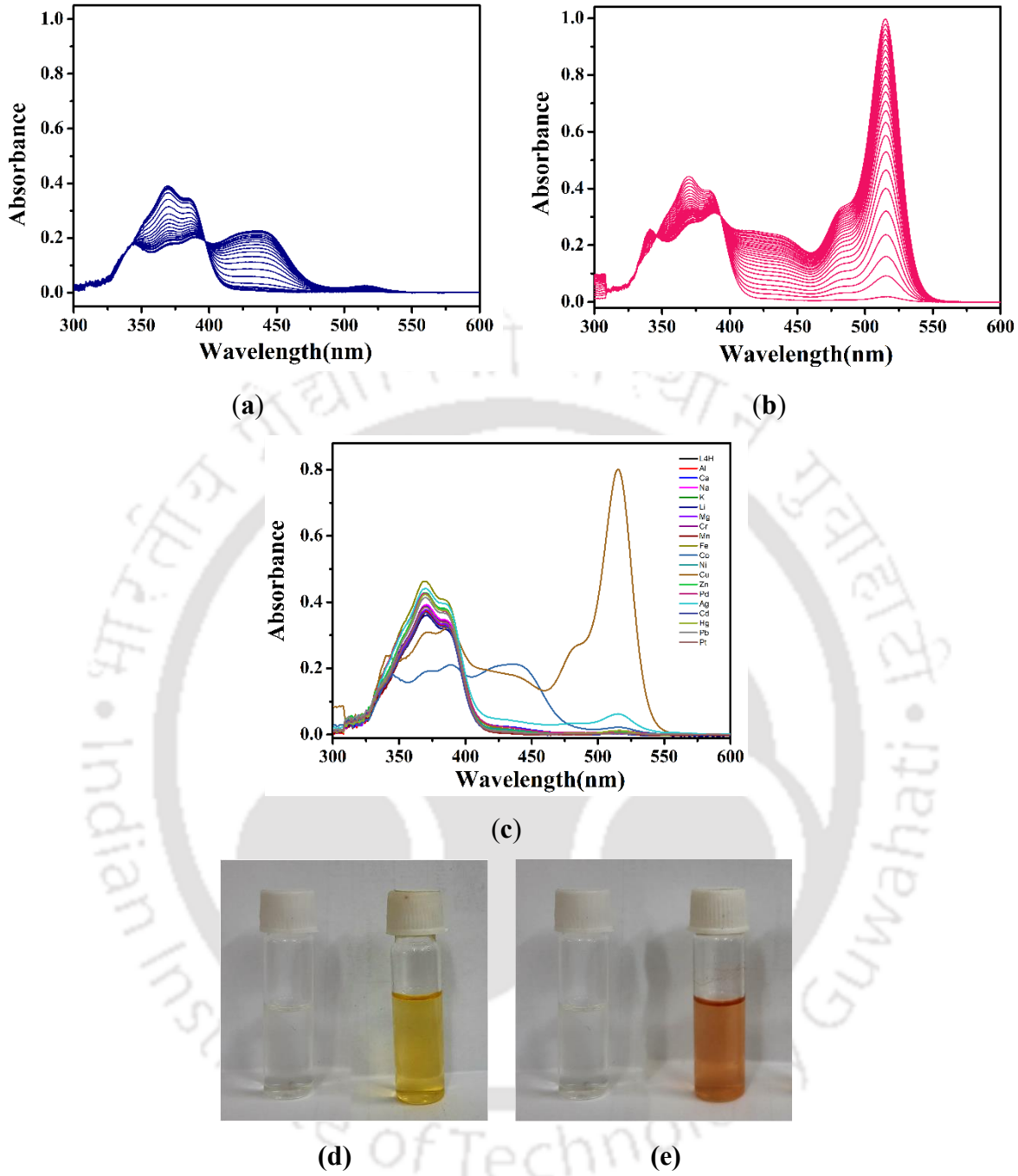

Figure 2: UV-Vis titration of **L4H** in CH_3CN/HEPES buffer (4:1, *v/v*, 2 mM, pH = 7.34) with (a) Co^{2+} (1 mM) and (b) Cu^{2+} (0.1 mM). (c) Comparison of UV-Vis spectra of **L4H** in the presence of various metal ions. Colour of the solution of **L4H** in presence of (d) Co^{2+} and (e) Cu^{2+} ions.

Gradual addition of Co^{2+} resulted in reducing the intensity of the λ_{max} and a new peak at 438 nm appeared with a clear isosbestic point at 397 nm. On the other hand, the addition of Cu^{2+} ion to the solution of **L4H** resulted in forming a new peak at 515 nm with one shoulder at 483

nm and a broad band around 435 nm. There were two isosbestic points at 346 nm and 393 nm respectively (Figure 2). The presence of an isosbestic point indicates stable complex formation between the Ligand and the **L4H**. The difference in the spectral observation in the cases of Co^{2+} and Cu^{2+} may be due to coordination through different binding sites.

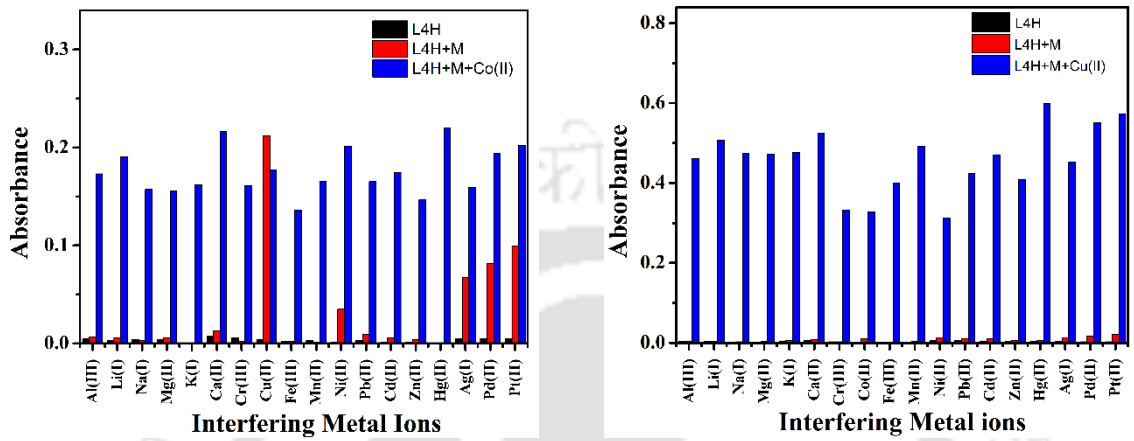

(a) **(b)**

Figure 3: Study of interference by different metal ions on (a) Co^{2+} and (b) Cu^{2+} ions.

Other metal ions can also bind to the binding sites of the **L4H** and thus can interfere in the sensing of Co^{2+} and Cu^{2+} ions, so a competitive study was done to ensure selective detection of Co^{2+} and Cu^{2+} ions. From that study (Figure 3) it can be said that the probe **L4H** can selectively detect Co^{2+} and Cu^{2+} in the presence of other metal ions. However, Ni^{2+}, Ag^{+}, Pd^{2+} and Pt^{2+} ions had shown little increase in intensity at 438 nm, which might be caused due to weak coordination between the metal ions and the **L4H**. But for sensing of Co^{2+}, only Cu^{2+} can interfere as there is an increase of absorbance intensity in the 438 nm region. So, apart from Cu^{2+} there is not much interference by other metal cations in the aforesaid solvent system.

5.3.2 Effect and estimation of BSA and HSA protein by the Cu-L4H complex

As the Cu^{2+} ion has the tendency to bind with amino acid side chain residues present in protein molecules, we have tried to explore the possible *in situ* interaction between the BSA (Bovine Serum Albumin) and HSA (Human Serum Albumin) proteins with the Cu^{2+}-**L4H** complex and use of it as an estimation technique of the protein. The gradual addition of the proteins to the stable *in situ* complex of Cu^{2+}-**L4H** resulted in a steady decrease of intensity at 515 nm (Figure 4) and it followed a linear pattern when plotted against the concentration of BSA and HSA proteins (Figure 5). The mechanism for this UV-spectral change may be due to the de-sequestration of Cu^{2+} from the Cu^{2+}- **L4H** complexes as it is abstracted by the proteins.

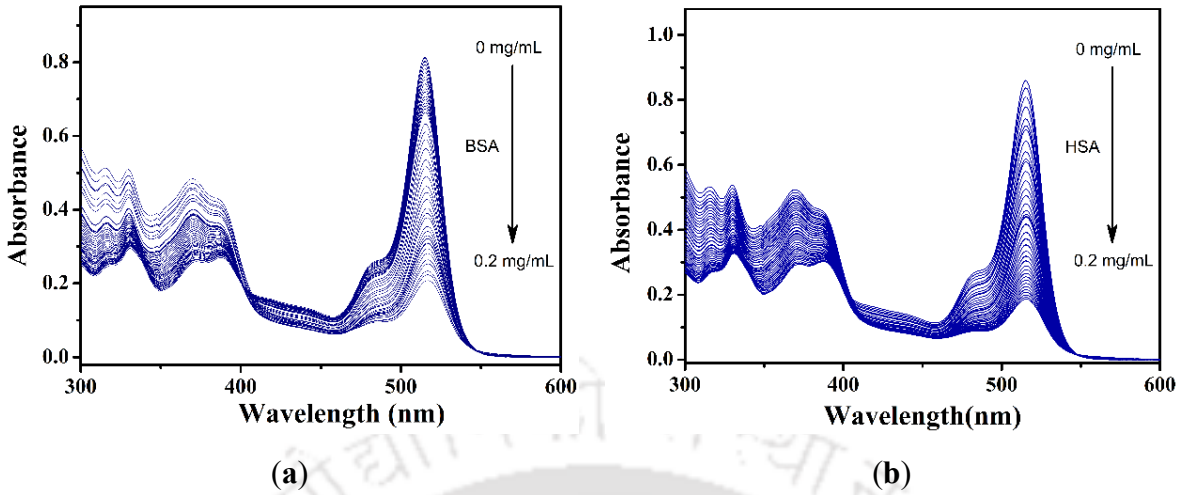

Figure 4: Titration of Cu^{2+}-**L4H** complex with (a) BSA and (b) HSA proteins in CH_3CN/HEPES buffer (4:1, *v/v*, 2 mM, pH = 7.34).

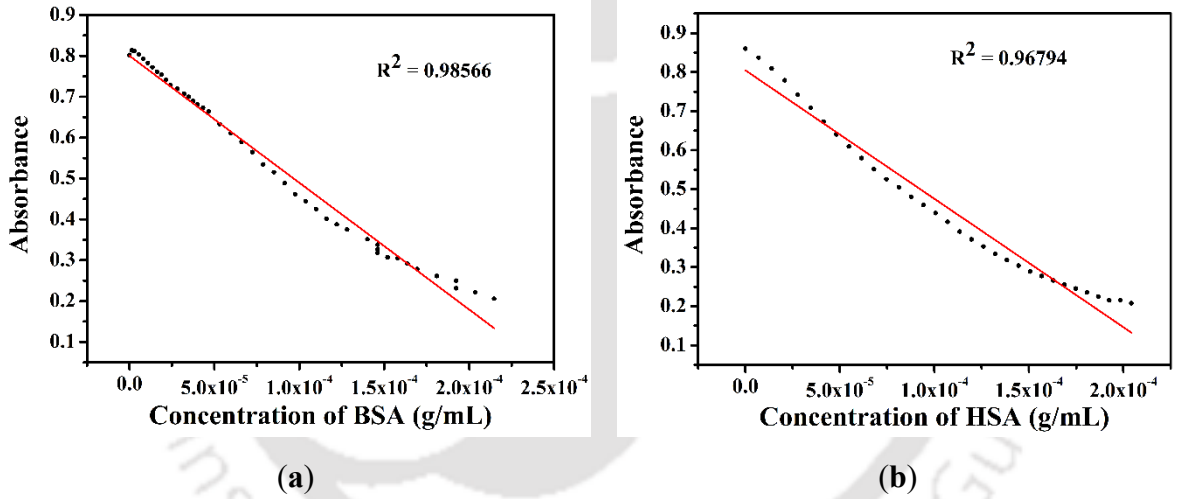

Figure 5: Calibration plot from the titration data for (a) BSA and (b) HSA.

5.3.3 Binding stoichiometry

Binding constant values were calculated from the Benesi-Hildebrand plot for both Co^{2+}-**L4H** and Cu^{2+}-**L4H** complexes. The binding constant values calculated from the plot are 2.013 × 10^4 L mol^{-1} for Co^{2+}-**L4H** and 5.986 × 10^4 L mol^{-1} Cu^{2+}-**L4H** complex. These high values of binding constants indicate stable complex formation in the solution (Figure 6). Stoichiometric ratio of the complexes were obtained from Job's plot where the ratio of Co^{2+} and **L4H** in Co^{2+}-**L4H** complex was calculated to be 1:2 but the ratio of Cu^{2+} and **L4H** in Cu^{2+}-**L4H** complex is found to be 1:1 (Figure 7). This can be further confirmed from the mass spectra where HRMS (ESI +ve) value of $[Co(C_{31}H_{17}Cl_2N_2O_5)_2]^+$ (Figure A5) obtained as 1195.0358 (Calcd.

1195.0332) and $[Cu(C_{31}H_{17}Cl_2N_2O_5)(MeO)] + Na^+$ (Figure A6) obtained as 683.43 (Calcd. 683.99).

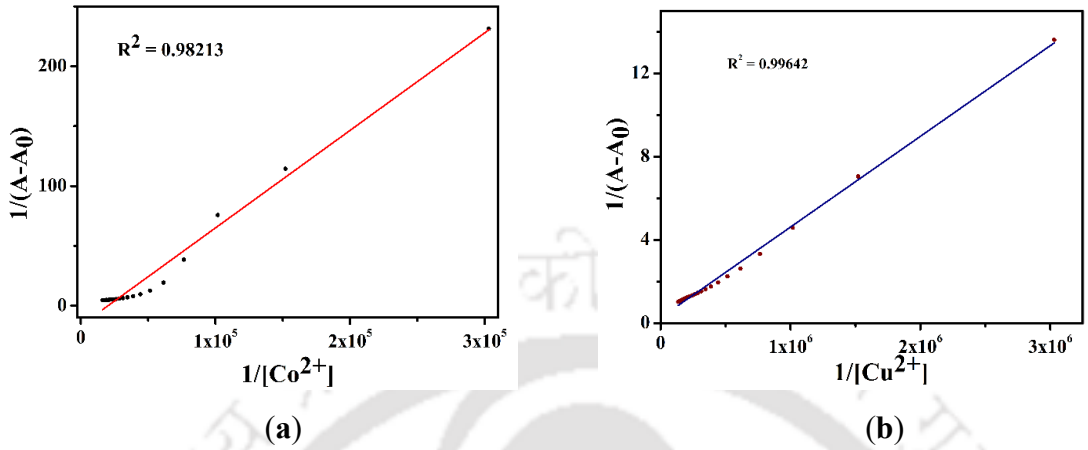

(a) **(b)**

Figure 6: Benesi-Hildebrand plot for **(a)** Co^{2+}-**L4H** and **(b)** Cu^{2+}-**L4H** complexes.

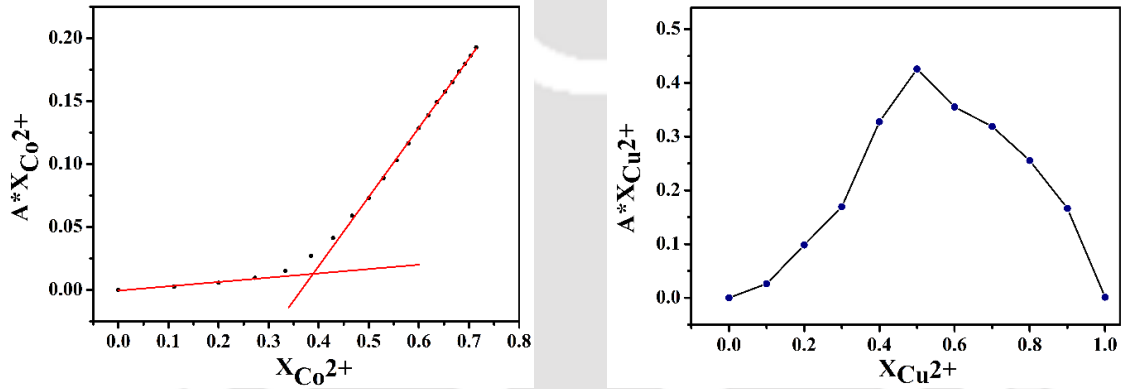

(a) **(b)**

Figure 7: Jobs plot analysis for the complexes **(a)** Co^{2+}-**L4H** and **(b)** Cu^{2+}-**L4H**

5.3.4 Limit of detection and quantification:

In order to establish the probe's practical applicability determination of the limit of detection is very necessary. Limit of detection was calculated from the calibration plot obtained from the UV-Vis titration of **L4H** with Co^{2+} and Cu^{2+} in CH_3CN/HEPES buffer (4:1, *v/v*, 2 mM, pH = 7.34) solvent system. The LOD values are 2.85 µM and 70.33 nM for Co^{2+} and Cu^{2+} respectively. As Cu^{2+} can be found in natural source of water and it is one of the primary contaminants of ground water ability of the **L4H** to detect Cu^{2+} in water was tested (Figure A7 and A8) and from the calibration plot LOD values were obtained. The LOD value of Cu^{2+} and Co^{2+} in drinking water and tap water are 221.31 nM and 200.73 nM (Table 2) respectively.

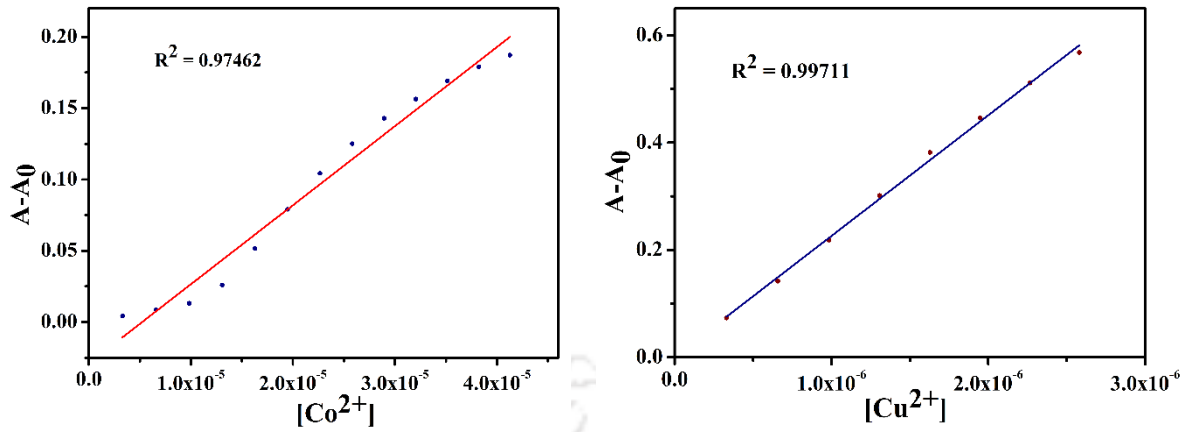

(a) (b)

Figure 8: Calibration plot for **(a)** Co^{2+} and **(b)** Cu^{2+} ion.

Table 2 LOD and LOQ values of metals in different medium.

Medium	Metal ion	LOD	LOQ
ACN/Buffer	Cu^{2+}	70.33 nM	234.44 nM
	Co^{2+}	2.85 µM	9.51 µM
Drinking Water	Cu^{2+}	221.31 nM	737.71 nM
Tap Water	Cu^{2+}	200.73 nM	669.12 nM

Table 3 LOQ values of BSA and HSA by Co-complex.

Protein	LOQ
BSA	44.29 µg L^{-1}
HSA	41.76 µg L^{-1}

As maximum quantifiable amount of any analyte dictates the limitation of any probe to be used for detection purpose the limit of quantification value is necessary to calculate. The *in situ* Cu^{2+}-**L4H** complex can be used for the quantification of the BSA and HSA proteins the practical applicability of the probe depends on the limit of Quantification ($10\sigma/k$)[27] value obtained from the same calibration plots (Figure 5, 8 and A8). LOQ values of Co^{2+} and Cu^{2+} in ACN/Buffer medium were found to be 9.51 µM and 230.44 nM respectively. In Drinking water and the Tap water medium the LOQ values for Cu^{2+} were 737.71 nM and 669.12 nM respectively. LOQ values for BSA and HSA proteins (Table 3) are as low as 44.29 μgL^{-1} and 41.76 μgL^{-1}.

5.3.5 pH effect

It is very important to understand the pH effect on the sensing of metal ions by **L4H** as there are one N-site and one O-site which can be protonated in lower pH making the lone pair of electrons on the N-sites unavailable for the coordination and deprotonated at higher pH to facilitate coordination. From the Figure 9 it can be observed that at pH ≥ 2 there was no effect on binding of Co^{2+} with **L4H** but at pH ≥ 8 the intensity of absorbance decreases so **L4H** cannot detect Co^{2+} beyond pH = 8. Thus, the effective pH range of detection for Co^{2+} is 2-8. For Cu^{2+} this effect was not observed as the absorbance value increased upon addition of Cu^{2+} in the range of pH = 1-10. So Cu^{2+} was detectable in a wider pH range than Co^{2+} (Figure 9).

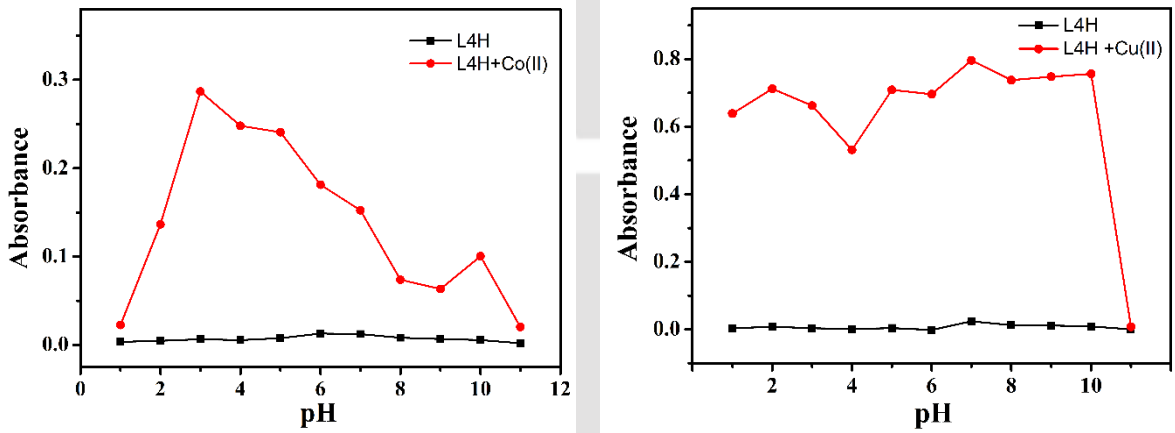

(a) **(b)**

Figure 9: Effect of variable pH for **(a)** Co^{2+} and **(b)** Cu^{2+} ion.

5.3.6: Application of L4H as a molecular logic gate

The probe **L4H** showed a significant photophysical property by exhibiting distinct absorption peaks at different wavelengths for Co^{2+} and Cu^{2+} ions. In the absence of any metal ion **L4H** showed a distinct absorption at 370 nm. And after the addition of the Co^{2+} and Cu^{2+} ions absorption maximum got shifted to 438 and 515 nm, respectively. So for application as logic gate the three wavelengths 370 nm, 438 nm and 515 nm were taken as output Y_1, Y_2 and Y_3 respectively. For output Y_1 absorbance value 0.2 is set as the optimum value above which the binary output was considered as 1 and below 0.2 the binary output was taken as 0. For outputs Y_2 and Y_3 the optimum level of absorbance value is taken as 0.1 (Figure 10). The input **A** is denoted by Cu^{2+} and input **B** by Co^{2+}. The presence of Cu^{2+} is considered as "*on state*" with binary number 1 and the absence of Cu^{2+} in the solution as "*off state*" with binary number 0.

Similarly, the presence of Co^{2+} is considered as "*on state*" with binary number 1 and the absence of Co^{2+} in the solution as "*off state*" with binary number 0. Accordingly, the truth table along with the logic gate circuit was constructed based on the output signals (Figure 11).

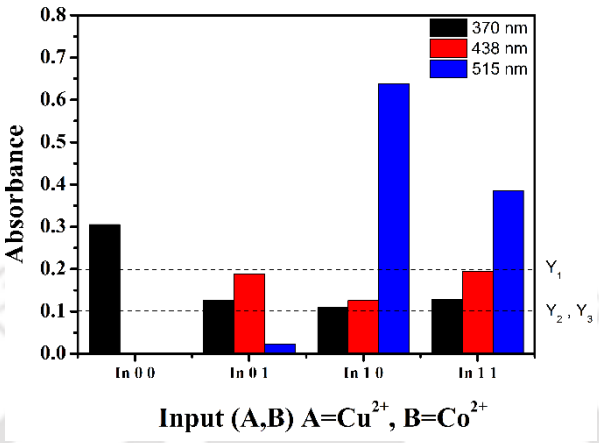

Figure 10: Absorbance levels for the logic gate analysis.

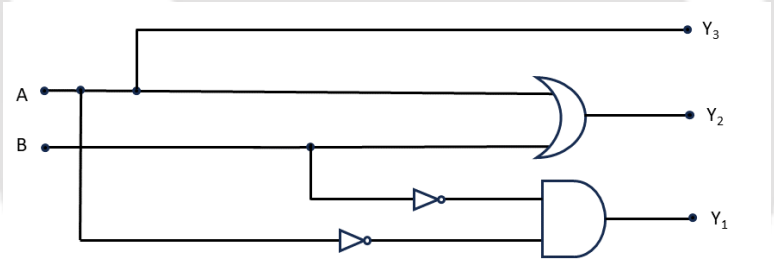

Truth table

A(Cu^{2+})	B(Co^{2+})	Y_1 (370 nm)	Y_2 (438 nm)	Y_3 (515 nm)
0	0	1	0	0
0	1	0	1	0
1	0	0	1	1
1	1	0	1	1

Logic equations

$$Y_1 = \bar{A}.\bar{B}$$
$$Y_2 = A + B$$
$$Y_3 = A$$

Figure 11: Logic gate operation along with the truth table and Logic equations.

When input **A** and input **B** were both in "*off state*," output Y_1 remained in "*on state*". Now if one of the inputs (or both) were in "*on state*", Y_1 went into "*off state*". So, output Y_1 was defined as AND logic operation after NOT operation on both the inputs. On the other hand, output Y_2 can be defined by the OR logic operation. Here, output Y_2 was in "*off state*" when input A and input B were in "off-state" and when one of the inputs (or both) was in "*on state*" the output Y_2 went into "*on state*", thus making it a classic example of OR logic operation.

Output Y_3 is independent of input B as it was in "on-state" only when the input A was in "*on state*".

5.3.7 Theoretical calculations

Optimization of molecular structures and the TD-DFT energy calculation of **L4H**, $[Cu(\mathbf{L4})(H_2O)]^+$ and $[Co(\mathbf{L4})_2]^+$ were done by Gaussian 16 program [28]. The calculations were performed at B3LYP level using 6-31G(d,p) basis set for **L4H** and in LANL2DZ for $[Cu(\mathbf{L4})(H_2O)]^+$ complex. But for $[Co(\mathbf{L4})_2]^+$ complex LanL2DZ basis set was assigned to metal centre and for other atoms 6-31G(d,p) was assigned. The theoretical electronic spectra were obtained with the help of Gaussview 06 software [29] by using the result of TD-DFT energy calculations. The ground state optimized structure of **L4H** showed that the xanthene ring is nearly perpendicular to the naphthalene ring. The HOMO of **L4H** is a π orbital with the electron density concentrated mostly on the naphthalene ring and the LUMO is of π^* and anti-bonding in nature with the lobes dominated over benzofuran and naphthalene ring. The probe **L4H** can lose the hydroxy proton and can also bind the metal ion as the anion $\mathbf{L4}^-$. Since the mass spectrum shows 1:1 binding ratio between **L4H** and Cu^{2+} and 1:2 ratio with Co^{2+} those ratios were maintained during calculations performed on these molecules The UV-Vis spectra obtained from the theoretical calculation showed similar shift of absorption maximum as observed in the experimental spectra (Figure 12). The energy corresponding to the transition $S_0 \rightarrow S_1$ in **L4H**, was calculated to be 3.3032 eV with oscillator frequency 0.4100, which involves promotion of an electron from HOMO to LUMO level. For $[Cu(\mathbf{L4})(H_2O)]^+$, the electronic transition involves alpha and beta set of MOs involving HOMO-LUMO(for alpha) and HOMO-1 - LUMO with the excitation energy of $S_0 \rightarrow S_{10}$ transition was calculated to be 2.2011 eV and with an oscillator frequency of 0.0066. At HOMO and HOMO-1 the electron density was observed to be concentrated on the xanthenone ring whereas, LUMO orbitals are mainly concentrated on the naphthalene ring. On the other hand, the in case of $[Co(\mathbf{L4})_2]^+$ electronic transition $S_0 \rightarrow S_{17}$ ($\Delta E = 2.7043$ eV, $f = 0.0753$) had the highest value of oscillator strength, involving HOMO-2, HOMO, LUMO+2 and LUMO+4 (Figure 13). The rest of the orbitals e.g., HOMO-1, LUMO, LUMO+1 and LUMO+3 are d orbitals on the Co^{2+} centre.

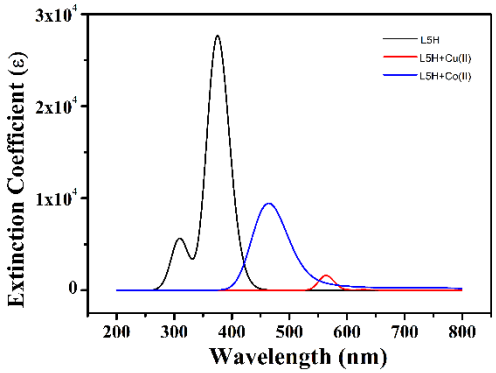

Figure 12 Theoretical UV-Vis spectra.

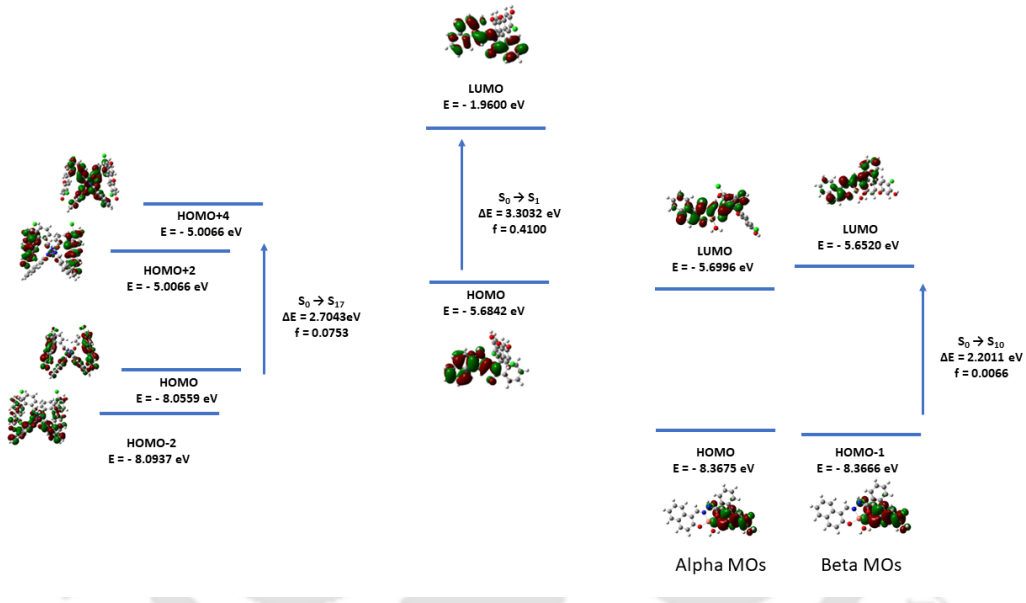

Figure 13 Ligand-based FMO and electronic transitions in gas.

5.3.8 Mechanism of Sensing

As shown in Scheme 2 in the presence of the metal ions the cyclic structure is going into the acyclic form via the formation of xanthenone. As a result, the sp^3 C becomes sp^2, which causes extended conjugation between naphthalene and xanthenone ring through benzohydrazide spacer. It is further confirmed from the theoretical TD-DFT analysis where the electron density is confined to the naphthalene ring in both the HOMO and LUMO of the free **L4H**. But in both the complexes the electron density was seen to be delocalised to the xanthenone ring and it gives stability to the system. For that reason, stabilisation of FMOs were observed for both the complexes and the energy differences were also lowered which causes absorption in longer wavelength.

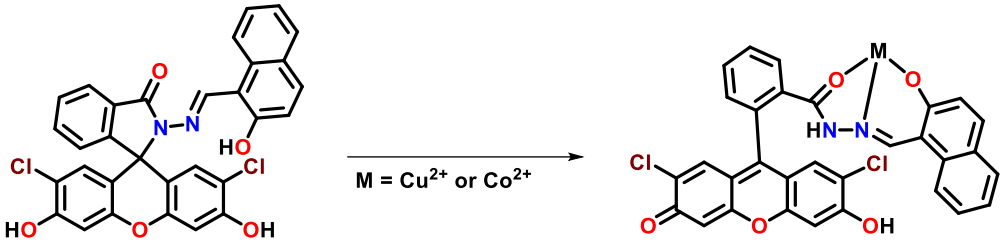

Scheme 2. Mechanism of sensing due to formation of $[Cu(\mathbf{L4})(H_2O)]^+$ and $[Co(\mathbf{L4})_2]^+$ ions (Only binding of one $\mathbf{L4}^-$ is shown and other ligands are omitted for clarity).

5.4 Conclusion

In conclusion it can be said that **L4H** can be good sensor for Cu^{2+} and Co^{2+} ions. Nanomolar detection limit of Cu^{2+} ion makes it a practically usable sensor probe. The probe binds with Cu^{2+} and Co^{2+} ions in 1:1 and 1:2 ratio, respectively. The probe has good pH tolerance along with differential colorimetric selectivity which can detect these two metal ions distinctively. The high binding constant values indicate towards stable complex formation. The *in situ* generated $[Cu(\mathbf{L4})(H_2O)]^+$ complex ion can utilised for quantification of the BSA and HSA proteins. Its differential selectivity leads to its application as molecular logic gate. Theoretical calculations support red shift of the 370 nm peak of **L4H** to 438 (Cu^{2+}) and 515 nm (Co^{2+}) upon coordination.

References

[1] P. Verwilst, K. Sunwoo, J. S. Kim, *Chem. Comm.* **2015**, *51*, 5556–5571.

[2] M. C. Linder, M. Hazegh-Azam, *Am. J. Clin. Nutr.* **1996**, *63*, 797S-811S.

[3] M. S. Tanner, *Am. J. Clin. Nutr.* **1998**, *67*, 1074–1081.

[4] T. Müller, H. Feichtinger, H. Berger, W. Müller, *Lancet* **1996**, *347*, 877–880.

[5] I. H. Scheinberg, I. Sternlieb, *Am. J. Clin. Nutr.* **1996**, *63*, 842S-845S.

[6] R. Mehta, D. M. Templeton, P. J. O'Brien, *Chem. Biol. Interact.* **2006**, *163*, 77–85.

[7] R. A. Festa, D. J. Thiele, *Curr. Biol.* **2011**, *21*, R877–R883.

[8] S. J. Uke, V. P. Akhare, D. R. Bambole, A. B. Bodade, G. N. Chaudhari, *Front Mater* **2017**, *4*, 1-6.

[9] M. Patel, U. Ajay, K. Padala, T. Naveen, *Asian J. Org. Chem.* **2022**, *11*, e202200201.

[10] M. Usman, M. Humayun, M. D. Garba, L. Ullah, Z. Zeb, A. Helal, M. H. Suliman, B. Y. Alfaifi, N. Iqbal, M. Abdinejad, A. A. Tahir, H. Ullah, *Nanomaterials* **2021**, *11*, 2029.

[11] D. Klarstrom, P. Crook, A. Sharif, in *Reference Module in Materials Science and Materials Engineering*, Elsevier, **2017**.

[12] L. J. Schreiner, C. P. Joshi, J. Darko, A. Kerr, G. Salomons, S. Dhanesar, *The Role of Cobalt-60 in Modern Radiation Therapy: Dose Delivery and Image Guidance*, **2008**.

[13] C. Yao, J. Lu, T. J. Webster, in *Biomaterials for Artificial Organs* (Eds.: M. Lysaght, T.J. Webster), Elsevier, **2011**, pp. 34–55.

[14] A. D. Smith, M. J. Warren, H. Refsum, in *Adv Food Nutr Res* (Ed.: N.A.M. Eskin), Academic Press, **2018**, pp. 215–279.

[15] S. R. Bhatta, A. Pal, U. K. Sarangi, A. Thakur, *Inorganica Chim. Acta* **2019**, *498*, 119097.

[16] B. Das, A. Jana, A. Das Mahapatra, D. Chattopadhyay, A. Dhara, S. Mabhai, S. Dey, *Spectrochim. Acta A Mol. Biomol. Spectrosc.* **2019**, *212*, 222–231.

[17] P. G. Mahajan, N. C. Dige, B. D. Vanjare, S.-H. Eo, S. J. Kim, K. H. Lee, *Spectrochim. Acta A Mol. Biomol. Spectrosc.* **2019**, *216*, 105–116.

[18] E. M. Bakir, A. R. Sayed, H. M. A. El-Lateef, *J. Photochem. Photobiol. A Chem.* **2022**, *422*, 113569.

[19] H. Mohammad, A. Saleh Musha Islam, M. Sasmal, C. Prodhan, M. Ali, *Inorganica Chim. Acta* **2022**, *543*, 121165.

[20] L. Huang, Y. Sun, G. Zhao, L. Wang, X. Meng, J. Zhou, H. Duan, *J. Mol. Struct.* **2022**, *1255*, 132427.

[21] N. Wanichacheva, O. Hanmeng, S. Kraithong, K. Sukrat, *J. Photochem. Photobiol. A Chem.* **2014**, *278*, 75–81.

[22] Y. Jiao, X. Liu, L. Zhou, H. He, P. Zhou, C. Duan, X. Peng, *J. Photochem. Photobiol. A Chem.* **2018**, *355*, 67–71.

[23] S. Kempahanumakkagari, P. Malingappa, G. Ambikapathi, D. Kuramkote Shivanna, *J. Spectroscop.* **2013**, *2013*, 1–8.

[24] S. Y. Lee, H. J. Kim, J.-S. Wu, K. No, J. S. Kim, *Tetrahedron Lett.* **2008**, *49*, 6141–6144.

[25] *APEX2, SAINT and SADABS*; Bruker AXS Inc.: Madison, WI, USA, **2013**.

[26] Sheldrick, G. M. Crystal structure refinement with SHELXL. *Acta Crystallogr., Sect. C: Struct. Chem.* **2015**, *71*, 3– 8,

[27] D. A. Armbruster, T. Pry, *Clin. Biochem. Rev.* **2008**, *29 Suppl 1*, S49-52.

[28] Gaussian 16, Revision C.01, M. J. Frisch, G. W. Trucks, H. B. Schlegel, G. E. Scuseria, M. A. Robb, J. R. Cheeseman, G. Scalmani, V. Barone, G. A. Petersson, H. Nakatsuji, X. Li, M. Caricato, A. V. Marenich, J. Bloino, B. G. Janesko, R. Gomperts, B. Mennucci, H. P. Hratchian, J. V. Ortiz, A. F. Izmaylov, J. L. Sonnenberg, D. Williams-Young, F. Ding, F. Lipparini, F. Egidi, J. Goings, B. Peng, A. Petrone, T. Henderson, D. Ranasinghe, V. G. Zakrzewski, J. Gao, N. Rega, G. Zheng, W. Liang, M. Hada, M. Ehara, K. Toyota, R. Fukuda, J. Hasegawa, M. Ishida, T. Nakajima, Y. Honda, O. Kitao, H. Nakai, T. Vreven, K. Throssell, J. A. Montgomery, Jr., J. E. Peralta, F. Ogliaro, M. J. Bearpark, J. J. Heyd, E. N. Brothers, K. N. Kudin, V. N. Staroverov, T. A. Keith, R. Kobayashi, J. Normand, K. Raghavachari, A. P. Rendell, J. C. Burant, S. S. Iyengar, J. Tomasi, M. Cossi, J. M. Millam, M. Klene, C. Adamo, R. Cammi, J. W. Ochterski, R. L. Martin, K. Morokuma, O. Farkas, J. B. Foresman, and D. J. Fox, Gaussian, Inc., Wallingford CT, **2016**.

[29] GaussView, Version 6.1, Roy Dennington, Todd A. Keith, John M. Millam, Semichem Inc., Shawnee Mission, KS, **2016**.

Appendix

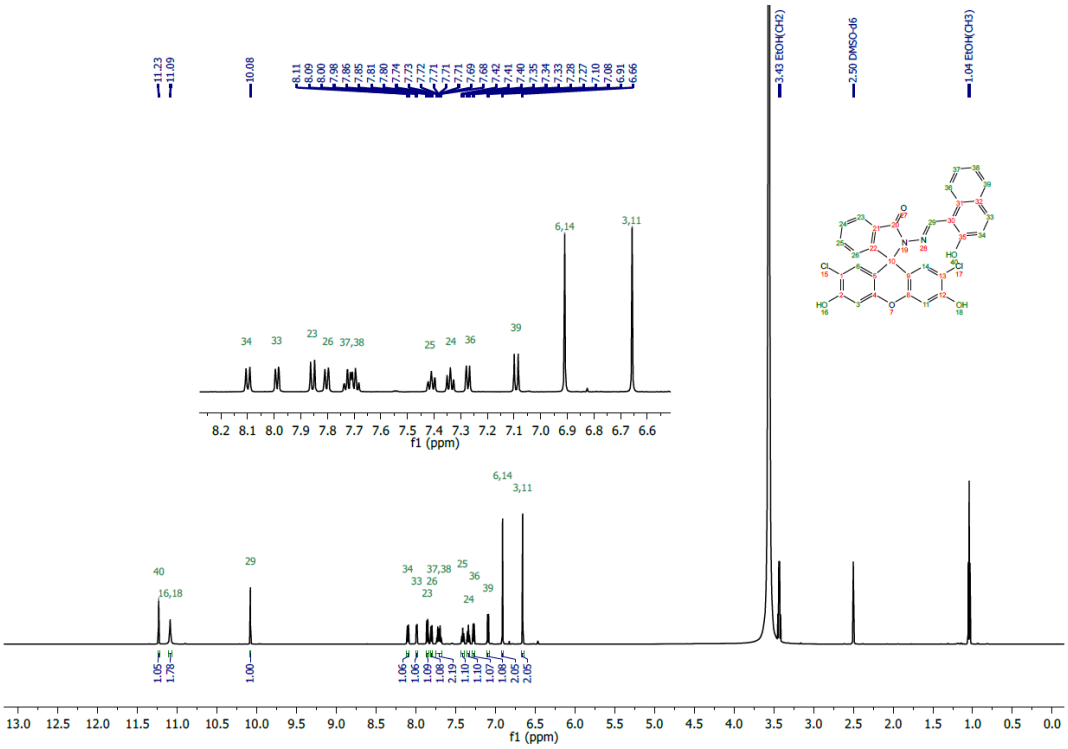

Figure A1 ^{1}H NMR of **L4H**.

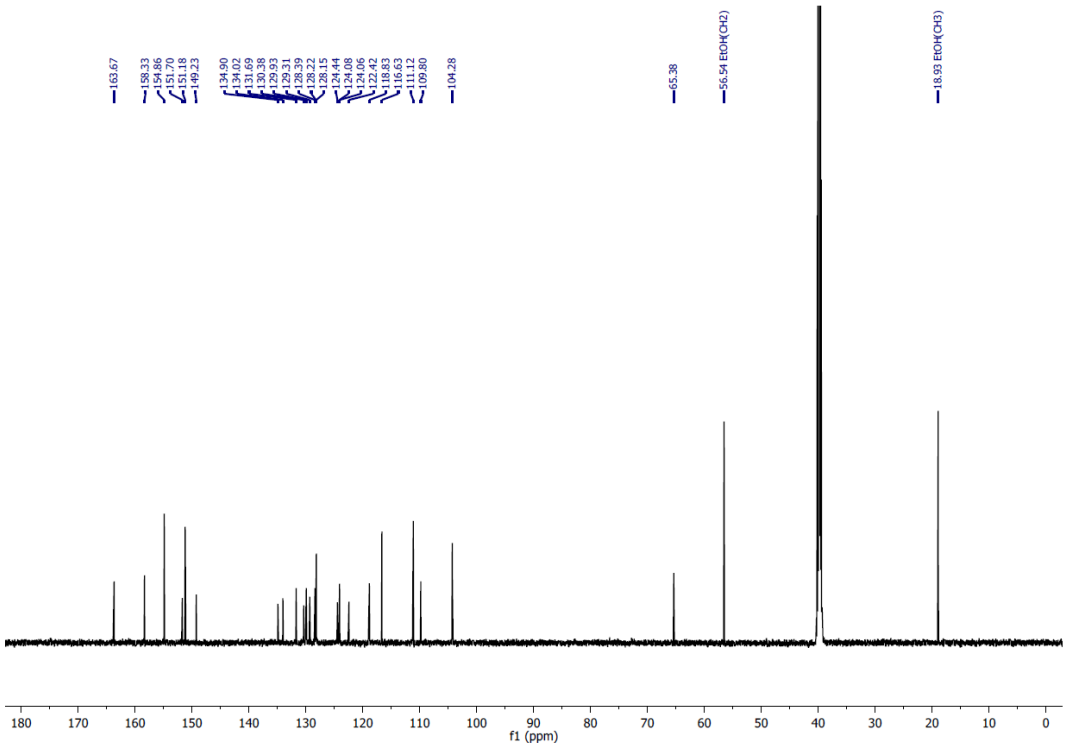

Figure A2 ^{13}C NMR of **L4H**.

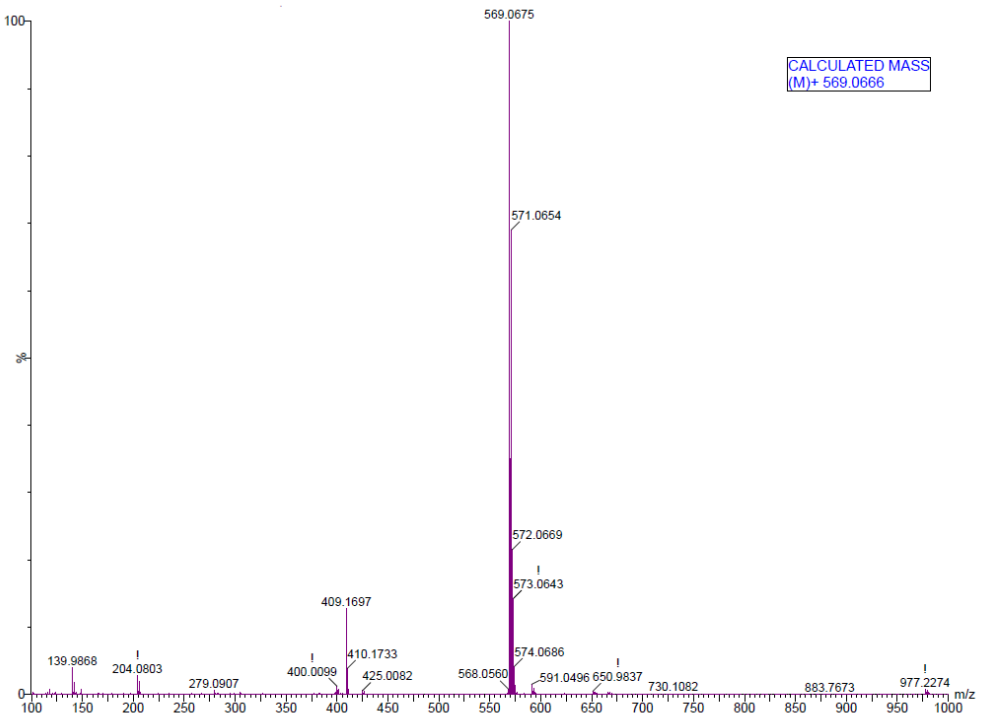

Figure A3 HRMS spectrum of **L4H**.

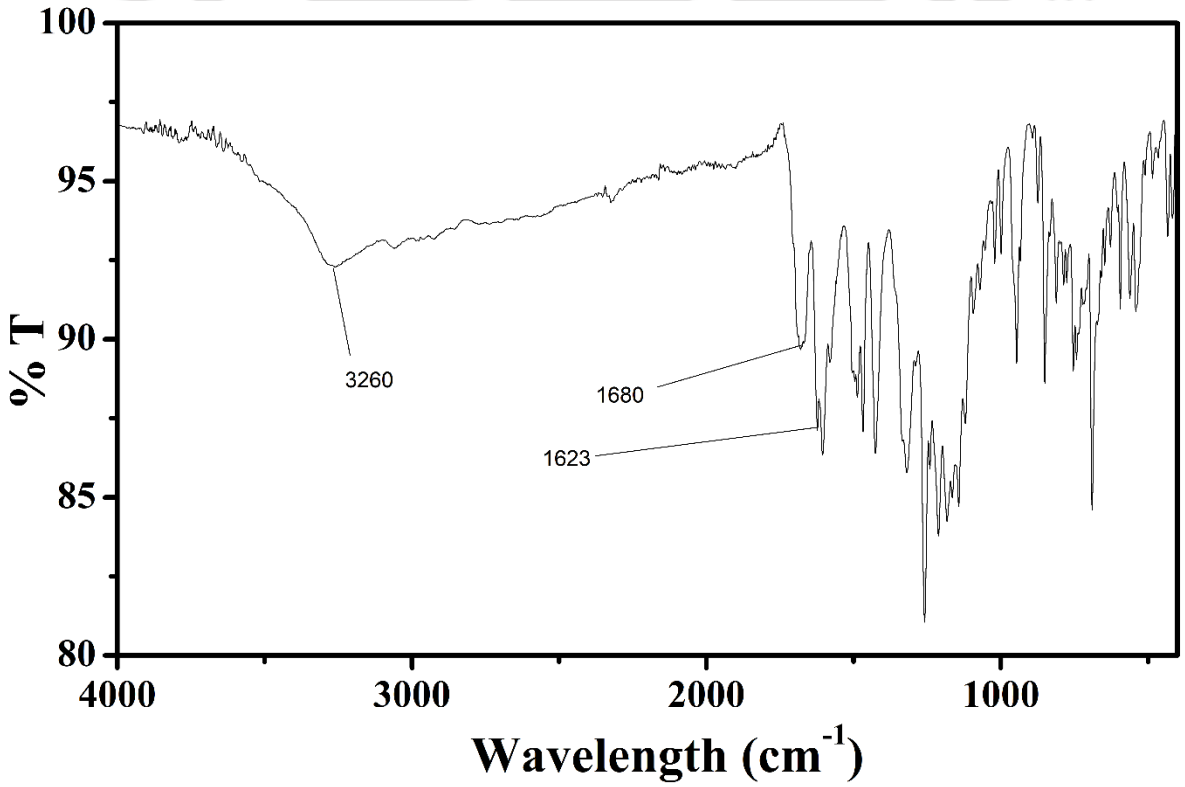

Figure A4 IR spectrum of **L4H**.

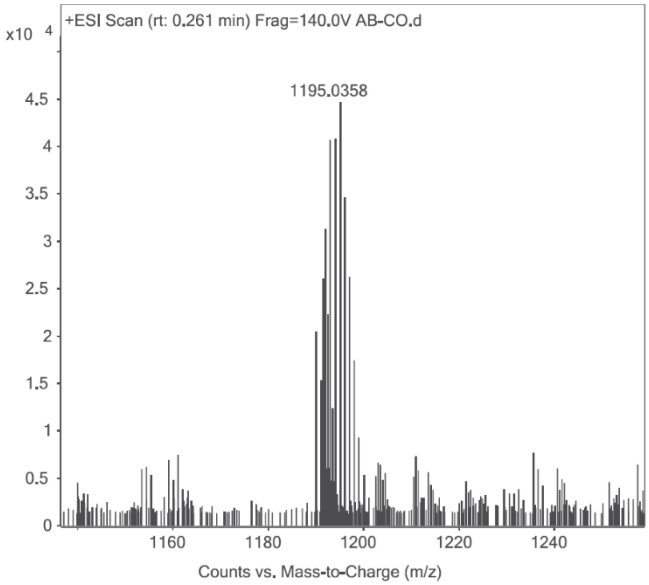

Figure A5 HRMS (ESI +ve) spectrum of Co^{2+}-**L4H** mixture.

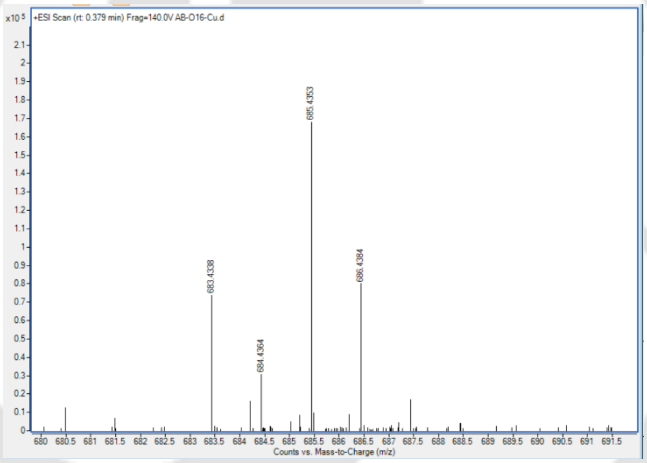

Figure A6 HRMS (ESI +ve) spectrum spectrum of Cu^{2+}-**L4H** mixture.

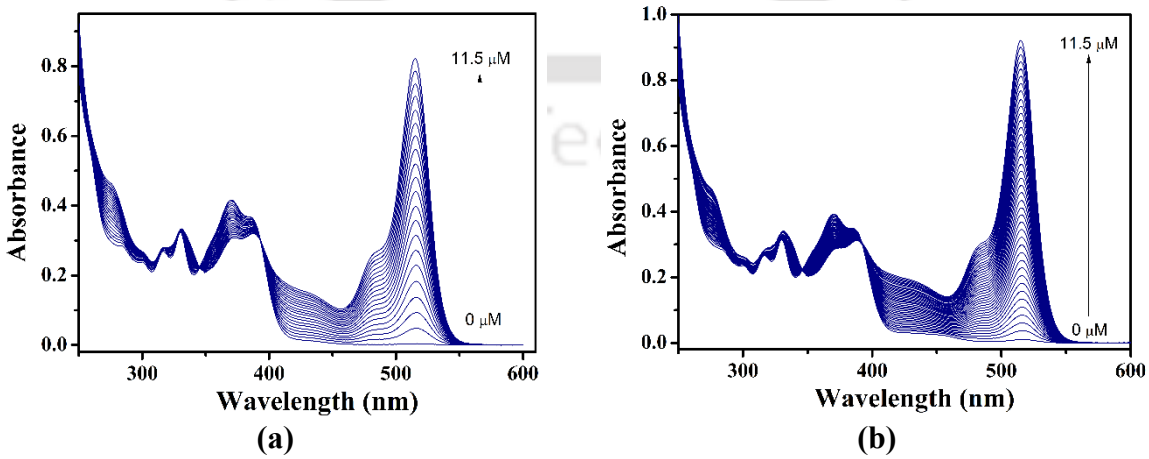

Figure A7 UV-Vis titration of **L4H** by $CuCl_2$ solution in **(a)** Drinking water and **(b)** Tap Water medium.

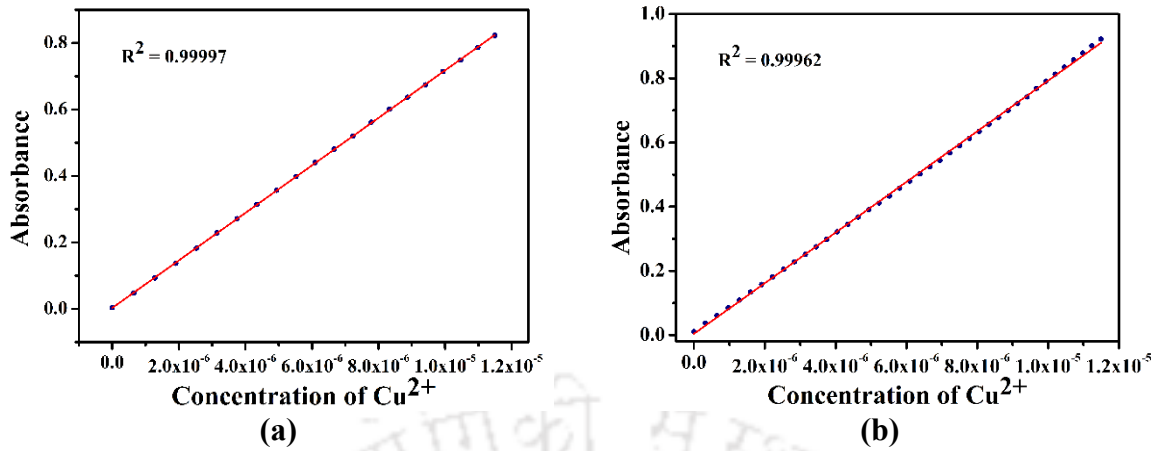

Figure A8 Calibration plot obtained from the titration data in **(a)** Drinking water and **(b)** Tap water medium.

Thesis Summary

In this thesis, Chapter 1 contains discussion of topics focussed on use and presence of metals in everyday life and biological systems. Different adverse effects of over exposure or accumulation of metals/metal ions on human health was further elaborated. Then different techniques for detection of metal ions in different systems was briefly discussed. Colorimetric and fluorometric detection techniques, being the cheaper alternatives for costly instrumental methods, was depicted and some recent examples of metal ions sensors incorporating different fluorophores was cited. At the end of the chapter different materials and methods used for experimentation was given in details. In Chapter 2, application of 2,4,5-tris(2-pyridyl)imidazole (**L1H**) as "turn-off" sensor for selective detection of Cu^{2+} and Hg^{2+} ions in EtOH/HEPES buffer medium (5 mM, pH = 7.34, 1:1, *v/v*) is explored. Electronic transitions are ascertained from the TDDFT analysis of **L1H**, and its complexes. A live cell imaging study was done to find out its practical usability in detecting Cu^{2+} and Hg^{2+} in live cells. In the Chapter 3 the probe 2,6-di(2-pyridyl)-1,5-dihydroimidazo[4,5-*f*]benzimidazole (**L2H$_2$**) is found to be a selective, reversible and ratiometric fluorescent sensor of Zn^{2+} and Cd^{2+} ions in different aqueous mediums. DFT/TDDFT analysis was done in depth to correlate the experimental absorbance with theoretical UV-Vis spectra. After that in chapter 4 a probe (**L3H**) having benzo[*d*]imidazo[2,1-*b*]thiazole and pyrene rings has been synthesised and characterised. It is found to be a brilliant colorimetric probe for the detection of Pd^{2+} and Ni^{2+} in CH_3CN/HEPES buffer (2mM, pH = 7.34, 4:1, *v/v*). This probe is further utilised to detect the trace amount of Pd^{2+} present in the API/Drug sample. The limit of detection ranges from 46.1 to 93.9 nM (4.9 to 6.0 ppb) for $PdCl_2$ and 10.6 to 19.6 nM (1.1 to 2.1 ppb) for $Pd(PPh_3)_2Cl_2$ and these are lower than the permitted daily exposure limit suggested by the European Medicines Agency (EMA). In the final Chapter 5, a novel ligand 2',7'-dichloro-3',6'-dihydroxy-2-(((2-hydroxynaphthalen-1-yl)methylene)amino)spiro[isoindoline-1,9'-xanthen]-3-one (**L4H**) has been synthesised and it is found to be a colorimetric sensor of Co^{2+} and Cu^{2+} ions in CH_3CN/HEPES buffer (2mM, pH = 7.34, 4:1, *v/v*) solvent medium. The probe exhibits a differential colorimetric signal in the presence of Co^{2+} and Cu^{2+} ions. With the help of this property, the in-situ Cu-complex formed can be utilised for the quantification of BSA and HSA proteins. This can be utilised to construct a molecular logic gate system.

Future Perspectives

In future, metal complexes of the said in-situ complexes formed during the sensing phenomenon can be synthesized and characterised by single crystal XRD. Some new fluorophores can be introduced with benzo[*d*]imidazo[2,1-*b*]thiazole and the 2,7-dichlorofluorescein to make new novel sensors for detection of various metal ions or anions. Biological application of the probes can be further studied.

List of Publications

From Thesis

[1] A. Bhattacharya, S. Mahata, A. Bandyopadhyay, B. B. Mandal, V. Manivannan, *Luminescence* 2022, **37**, 883–891.

[2] A. Bhattacharya, V. Manivannan, *J Photochem Photobiol A Chem* 2023, **444**, 114913.

[3] *Colorimetric detection of* Pd^{2+} *and* Ni^{2+} *ions using a probe having benzo[d]imidazo[2,1-b]thiazole and pyrene rings: application in detection of* Pd^{2+} *ion in anti-hypertensive drugs* (Manuscript under revision)

From others

[1] S. Mahata, A. Bhattacharya, J. P. Kumar, B. B. Mandal, V. Manivannan, *J Photochem Photobiol A Chem* 2020, **394**, 112441.